AD-A179 884 BASIC PROCESSES OF PLASMA PROPULSION(U) STUTTGART UNIV 1/2
(GERMANY F R) INSTR FUER RAUMFAHRTSYSTEME
H O SCHRADE ET AL 30 JAN 87 AFOSR-VR-87-0557
UNCLASSIFIED AFOSR-82-0298 F/G 21/3 NL

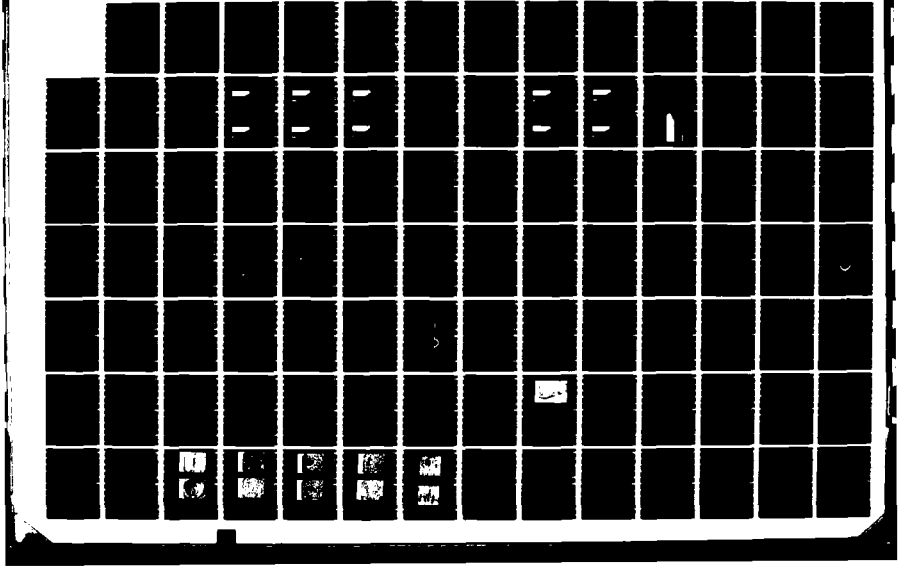

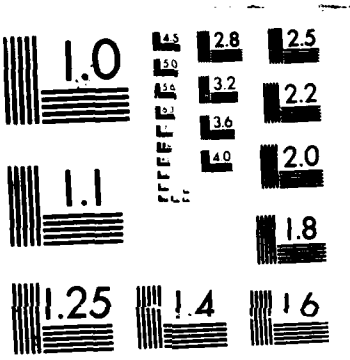

AFOSR-TR- 87-0557

AFOSR Grant 82-0298

BASIC PROCESSES OF PLASMA PROPULSION

Herbert O. Schrade
Monika Auweter-Kurtz
Helmut L. Kurtz

January 1987

Final Scientific Report, 1 August 1982 - 31 July 1986

Approved for public release; distribution unlimited

prepared for

Air Force Office of Scientific Research
Bolling AFB, DC
and
European Office of Aerospace Research and Development
London, England

I. The current density distribution, flow, pressure, and density fields are calculated for a (quasi-) steady nozzle-type MPD thruster, based on a partially two-dimensional approach, assuming a fully singly ionized plasma with an isothermal electron and an adiabatic ion behavior. In addition, for a given current rise, the current contour lines and the flow, pressure, and density fields within the cylindrical flow discharge region are calculated as a function of time. As initial conditions, one assumes a homogeneous radial current within a confined axial electrode region and a supersonic homogeneous axial flow.

II. In order to investigate the arc stability, a unique theoretical approach is presented which allows determination of the stability behavior of an arbitrarily shaped current-carrying plasma channel under various conditions. Based on this novel theory, the onset phenomenon observed in any nozzle-type MPD arc jets can be predicted; calculated and measured results agree favorably. Moreover, this stability theory can also explain the very strange behavior of arc spots and the, until now, seemingly obscure retrograde and Robson drift motion of arcs in a transverse magnetic field.

III. The cathode attachment of electric arcs are theoretically and experimentally investigated. The erosion effects and the surface damage due to spots are discussed; they stem from evaporation, droplet ejection, and/or splashing. The most severe damage to the cathode surface occurs when many samll spots cluster together and build one or even several larger spots which now cause melting and splashing. Erosion rate measurement on different surfaces and cathode materials are presented.

P r e f a c e

The work described in this final report has been sponsored by the Air Force Office of Scientific Research through the European Office of Aerospace Research and Development in London under Grant AFOSR 82-0298. The research work period covered herein is from August 1, 1982 to July 31, 1986.

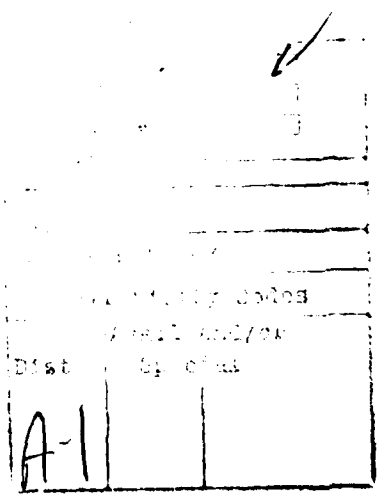

TABLE OF CONTENTS

1. Introduction and Objectives

The on-board power requirement for future space missions will soon grow into a range high enough such that magnetoplasmadynamic propulsion systems become attractive for many near-earth applications, for which modest specific impulse values of 10 to 30 km/s are optimal. However, the development stages of the different possible MPD thrusters and systems are insufficient to reliably predict performance, life, weight and cost potentials. Moreover, the fundamental understanding of MPD discharges is still incomplete. Therefore, a detailed investigation of the arc discharge and acceleration processes within a) the electrode gap and b) the arc electrode interphase region of those devices is mandatory.

The research work covered in this report deals with both problem areas and intends at first to give proper explanations of the still not fully understood limiting processes occuring in MPD arc propulsion devices and eventually to develop design criteria for annular self-field MPD arc thrusters.

Objectives

It is necessary to gain an understanding of the fundamental processes occuring in coaxial arc jet and MPD arc thrusters, in order to obtain reliable design criteria and to predict thruster performances.

To achieve these goals, one must

- investigate the arc cathode and anode attachments under different operating modes (experimental and analytical),
- develop computational methods to determine the flow arc discharge region and the acceleration mechanisms, and
- analyze the arc stability under various operating conditions and geometries (onset)

Based on these objectives, the report is divided into three sections:

- flow discharge calculations,
- stability theory and
- electrode investigations.

2. Flow Discharge Calculations

2.1 Nozzle-Type MPD Thruster Investigations (Steady-State)

In order to predict the overall performance of a nozzle-type self-field MPD thruster (Figs. 1 and 2) a semi-two-dimensional model calculation and computer program has been developed. In this approach, the current contour lines are calculated in r- und z- dependence while the flow field is taken as a one-dimensional, frictionless expansion flow assuming isothermal behavior for the electron component and isentropic expansion for the heavy particles like ions and neutrals. This assumption is justified, since primarily the electron component is heated by Ohmic energy input, and since within the nozzle expansion flow the energy exchange between the lightweight electrons and the heavy particles like ions and neutrals is fairly weak. Likewise, reaction collisions (ionization and recombination processes, etc.) are neglected. Hence, the model approach distinguishes between electron and heavy particle temperatures and assumes a frozen flow from the nozzle throat on downstream.

Within the nozzle throat, one assumes a "fully developed" arc flow regime, i.e. the gas and plasma velocity has only an axial component and the arc column is defined by only radial heat transfer (and possibly by radial radiation) losses. Moreover, from the nozzle throat on upstream, one no longer distinguishes between electron and heavy particle temperatures, since within this higher pressure regime a tight coupling between all components is more likely to be established than in the low pressure downstream nozzle regime. In spite of the neglect of the radial dependency of the flow and species temperatures, however, this model approach turns out to be an effective tool for predicting the current contour lines within and the thrust and specific impulse of a nozzle-type self-field MPD thruster.

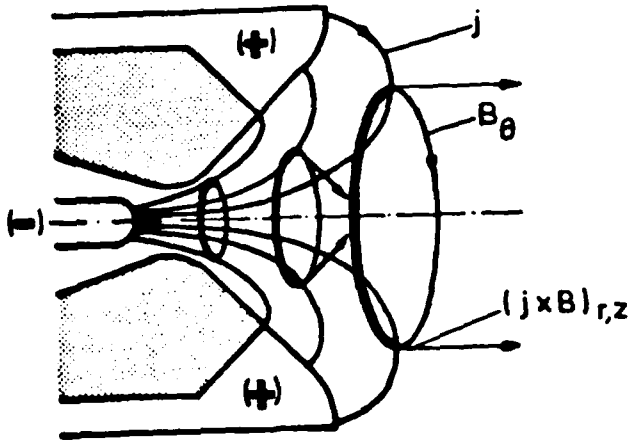

Fig. 1 Principle of Nozzle-Type MPD Thruster

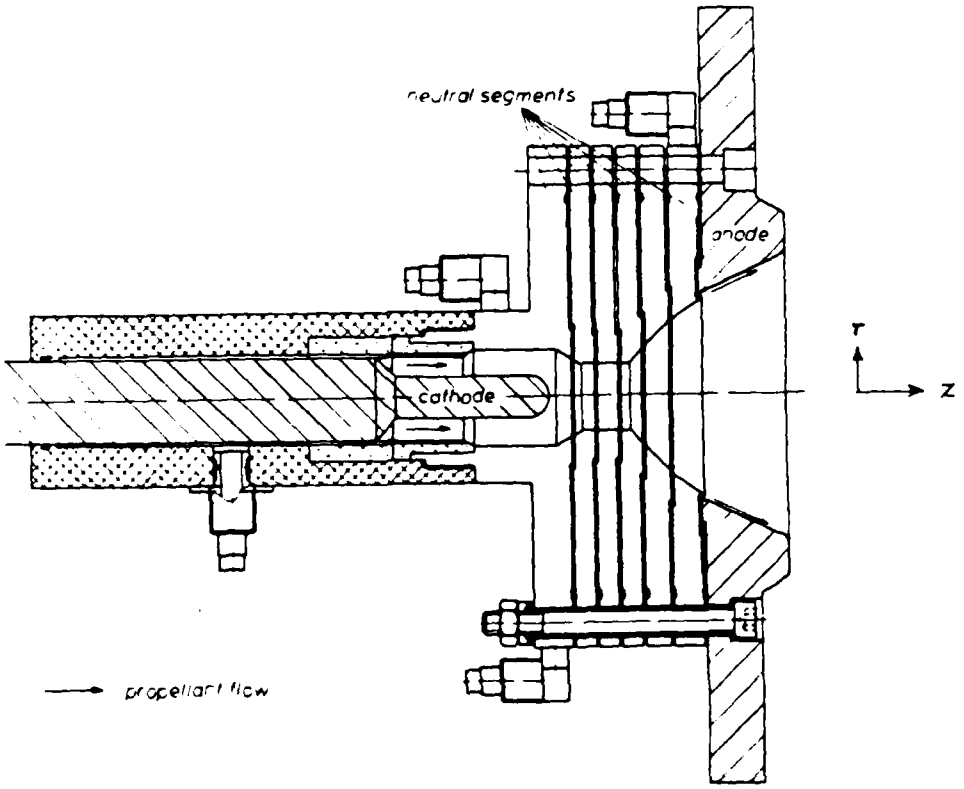

Fig. 2 Stuttgart University Continuous Water-Cooled Research Self-Field MPD Thruster (Capacity about 5 kA or 15 N Thrust with Argon).

The thrust of a self-field MPD accelerator is composed of two effects; first the sum of all gas-dynamic surface forces on the inner plenum chamber and on the inner nozzle wall, and second the sum of all volume effects given by the magnetic field forces which act between the current-carrying plasma and the entire power circuit, including the coaxial electrodes. Hence it is

$$\vec{T}h = \int_{A_S} \{\rho \overleftrightarrow{vv} + \overleftrightarrow{P}\} \cdot d\vec{A} \quad - \int_{V=V_1+V_2} \vec{j} \times \vec{B} \, dV \tag{1}$$

$$= c_{Th} p_0 A_t - \int_{V=V_1+V_2} \vec{j} \times \vec{B} \, dV \tag{1a}$$

where $\{\rho \overleftrightarrow{vv} + \overleftrightarrow{P}\}$ is the gas dynamic force per unit area and A_S represents the surface of all internal walls like plenum chamber with the gas inlet cross sections, the cathode surface and the inner solid wall of the nozzle. The second term is the sum over all $\vec{j} \times \vec{B}$ forces which act between the current-carrying solid leads of the electric power circuit and the current-carrying plasma; in the second equation (1a) p_0 is the chamber pressure, A_t the nozzle throat area and c_{Th} the thrust coefficient which matches the gas dynamic effects. It is by definition

$$c_{Th} = \frac{1}{p_0 A_t} \int_{A_S} \{\rho \overleftrightarrow{vv} + \overleftrightarrow{P}\} \cdot d\vec{A} \tag{2}$$

The above thrust formula eq. (1) can be rearranged by means of the equation of motion

$$\nabla \{\rho \overleftrightarrow{vv} + \overleftrightarrow{P}\} = \vec{j} \times \vec{B} \tag{3}$$

which is integrated over the volume V_1 of the plenum and nozzle (see Fig. 3). With the theorem of Gauss follows

$$\int_{V_1} \nabla \{\rho \overleftrightarrow{vv} + \overleftrightarrow{P}\} \cdot dV = \int_{A_S} \{\rho \overleftrightarrow{vv} + \overleftrightarrow{P}\} \cdot d\vec{A} + \int_{A_e} \{\rho \overleftrightarrow{vv} + \overleftrightarrow{P}\} \cdot d\vec{A}$$

$$= \int_{V_1} \vec{j} \times \vec{B} \, dV \tag{4}$$

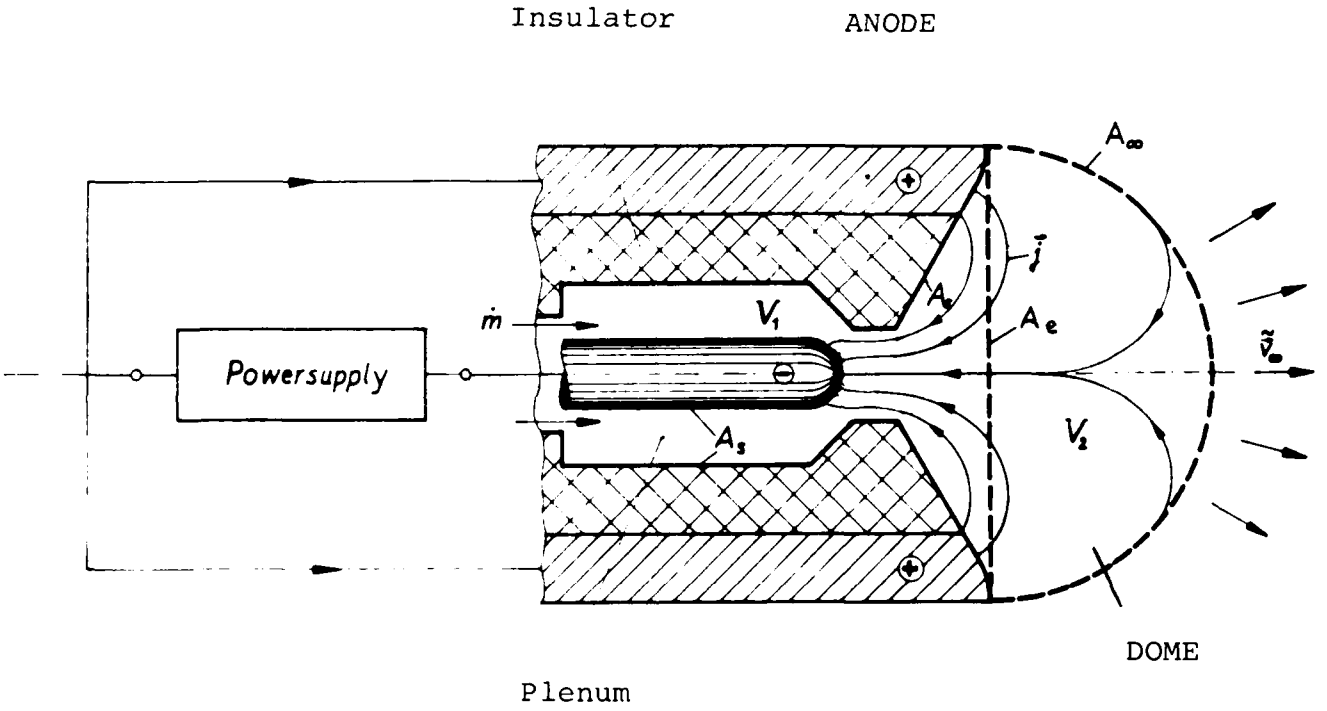

Fig. 3 Scheme of the Different Regions of a Nozzle - Type MPD Thruster

Replacing $\int_{A_s} \{\rho \overleftrightarrow{vv} + \overleftrightarrow{P}\} \cdot d\vec{A} - \int_{V_1} \vec{j} \times \vec{B}\, dV$ in the formula for the thrust (1) according to this relation (4) one obtains

$$\vec{Th} = - \int_{A_e} \{\rho \overleftrightarrow{vv} + \overleftrightarrow{P}\} \cdot d\vec{A} - \int_{V_2} \vec{j} \times \vec{B}\, dV \qquad (5)$$

or in our one-dimensional flow approach, by neglecting viscous effects and by taking the ambient pressure to be zero, the absolute thrust is

$$Th = \dot{m}\, v_{ex} + A_{ex} p_{ex} + \left| \int_{V_2} \vec{j} \times \vec{B}\, dV \right| \qquad (6)$$

where now $\dot{m}$ is the mass flow rate, v_{ex} the exit velocity and p_{ex} the average pressure at the nozzle exit, and V_2 is the volume of the current-carrying "dome" region outside the nozzle. Hence, instead of knowing the flow and pressure on the inner solid walls of the thruster, one needs only to determine the flow and pressure on the exit area A_E of the nozzle and the $\vec{j} \times \vec{B}$ force distribution within the dome region. Nevertheless, the $\vec{j} \times \vec{B}$ distribution should be known in the entire current-carrying plasma region of volume V_1 and V_2, since the expansion processes within the nozzle (V_1) depend on the axial effects of the $\vec{j} \times \vec{B}$ forces. This is shown in Appendix I. One obtains for the thrust

$$Th = \dot{m}\, v_t \left\{ \frac{v_{ex}}{v_t} + \frac{1}{1+\alpha} \frac{v_t}{v_{ex}} \left[\alpha + \left(\frac{v_t A_t}{v_{ex} A_{ex}} \right)^{\kappa-1} \right] \right\}$$

$$+ \left| \int_{V_2} \vec{j} \times \vec{B}\, dV \right| \qquad (7)$$

and hence the specific impulse by

$$I_{sp} = \frac{Th}{\dot{m}} \qquad (8)$$

where v_t is the average velocity within the nozzle throat, A_t is the throat area, α is the degree of ionization and $\kappa = c_p/c_v$ the quotient of the specific heats.

The calculation of the thrust and/or the specific impulse and the current contour lines follows now according to a stepwise approximation based on the following equations and assumptions.

Assumptions:

- steady state conditions
- rotational symmetry
- singly ionized, quasi-neutral plasma
- thermal equilibrium from cathode to nozzle throat--frozen flow from there on downstream
- ambipolar expansion flow without friction (electrons: isothermal; ions: adiabatic)
- within nozzle throat fully developed flow conditions with equal electron- and ion temperatures
- electric current density normal to electrode surface

Basic Equations:

Maxwell's eqs.:

$$\nabla \times \vec{B} = \mu_0 \vec{j} \qquad \text{a)}$$

$$\nabla \times \vec{E} = -\frac{\partial \vec{B}}{\partial t} = 0 \qquad \text{b)}$$

$$\nabla \cdot \vec{B} = 0 \qquad \text{c)} \qquad (9)$$

$$\nabla \vec{E} = 0 \qquad \text{d)}$$

Ohm's Law:

$$\vec{j} = \sigma \{\vec{E} + \vec{v} \times \vec{B}\} - \frac{\omega\tau}{B} [\vec{j} \times \vec{B}] \qquad (10)$$

$$\sigma = \frac{e^2 n_e}{m_e} \tau \quad *) \qquad (11)$$

$$\tau = \frac{3\sqrt{\pi}}{8\sqrt{2}} \frac{m_e}{\sum_{\nu \neq e} n_\nu Q_{e\nu} \sqrt{m_e kT_e}} \quad *) \qquad (12)$$

$$\omega = \frac{eB}{m_e} \qquad (13)$$

where $Q_{e\nu}$ = Collision cross section between electrons and particles of type ν.

Degree of Ionization (Defeinition): $$\alpha = \frac{n_e}{n_i + n_0} \tag{14}$$

Quasi Neutrality: $$n_e = n_i = \alpha \frac{\rho}{m_0} \tag{15}$$

Equation of State*: $$p = \rho \frac{k}{m_0} T_t \left\{\alpha + \left(\frac{\rho}{\rho_t}\right)^{\kappa-1}\right\} \tag{16}$$

Continuity Equation: $$\rho v A = \rho_t A_t v_t = \dot{m} \tag{17}$$

Expansion Relation*: $$\left(\frac{v}{v_t}\right)^2 = 1 + \frac{2\alpha}{1+\alpha} \ln \left|\frac{A}{A_t}\frac{v}{v_t}\right| + \frac{2}{1+\alpha}\frac{\kappa}{\kappa-1}\left[1 - \left(\frac{A_t}{A}\frac{v_t}{v}\right)^{\kappa-1}\right] + \frac{2}{\dot{m} v_t}\int_{z_t}^{z}\left(\frac{v}{v_t}\right)(\vec{j} \times \vec{B})_z A\, dz \tag{18}$$

Nozzle Throat Conditions**: $$v_t^2 = \left(\frac{\partial p}{\partial \rho}\right)_{t,\text{isoth}} = 2\frac{k}{m_0} T_t \tag{19}$$

$$T_t = T_e = f\left(\frac{I}{r_t}\right) \sim \left(\frac{I}{r_t}\right)^{2/5} \tag{20}$$

---

* see Appendix I

** see Appendix II

Input data:

- Geometry of Thruster $A(z)$
- Mass Flow Rate $\dot{m}$
- Electric Current I

Result:

- Current Contour Lines
- Thrust, Th
- Specific Impulse, I_{sp}

The stepwise solution proceeds now in the following manner.

First, one rewrites Ohm's Law (10) by means of Maxwell's equations (9a-d) and obtains a vector equation for the magnetic induction vector $\vec{B}$ in the form

$$-\frac{\partial \vec{B}}{\partial t} = \frac{1}{\mu_0} \operatorname{curl} \left(\frac{1}{\sigma} \operatorname{curl} \vec{B}\right) - \operatorname{curl} \left[\vec{v} \times \vec{B}\right] + \frac{1}{\mu_0} \operatorname{curl} \left[\beta \, (\operatorname{curl} \vec{B}) \times \vec{B}\right] = 0 \qquad (21)$$

Based on the rotational symmetry, the zero azimuthal current density and the one-dimensional flow in z-direction along the nozzle axis, one obtains

$$\vec{B} = \begin{bmatrix} B_r = 0 \\ B_\theta = B \\ B_z = 0 \end{bmatrix} \qquad (22a); \qquad \vec{v} = \begin{bmatrix} v_r \\ v_\theta = 0 \\ v_z = v \end{bmatrix} \qquad (22b)$$

and for the quantity

$$\Psi = rB_\theta$$

follows from eq. (19) the elliptic, partial differential equation of 2nd order in the form

$$\frac{d^2\Psi}{dr^2} + \frac{d^2\Psi}{dz^2} - \frac{d\Psi}{dr}\left(\frac{1}{r} + \frac{1}{\sigma}\frac{d\sigma}{dr} - \frac{\sigma\Psi}{r}\frac{d\beta}{dz} + \sigma\mu_0 v_r\right)$$

$$- \frac{d\Psi}{dz}\left(\frac{1}{\sigma}\frac{d\sigma}{dz} - \frac{\sigma\Psi}{r}\frac{d\beta}{dr} - \frac{2\sigma\beta\Psi}{r^2} + \sigma\mu_0 v_z\right)$$

$$- \sigma\mu_0\Psi\left(\frac{dv_r}{dr} + \frac{dv_z}{dz} - \frac{v_r}{r}\right) = 0 \qquad (24)$$

with $\beta = \frac{\omega\tau}{B\sigma} = \frac{1}{en_e}$ (25)

The function $\Psi(r,z)$ = const. represents now a current contour line, since $B = B_\theta \sim I(r)/r$ and $I(r)$ is the electric current carried through a cross sectional area of πr^2. The proper boundary conditions for Ψ follow from the geometry of the thruster walls and electrodes.

Step 1: By setting the integral

$$\int_{z_t}^{z} \left(\frac{v}{v_t}\right)\left(\vec{j} \times \vec{B}\right)_z A \, dz$$

in the expansion relation eq. (18) to zero, one obtains together with eqs. (19) and (20) a first approximation of $v = v(z)$, $p = p(z)$, $\rho = \rho(z)$ and $n_i = n_e = n_e(z)$ within the nozzle. Outside the nozzle one assumes two possible flow conditions:

Case a: an extended conical plume ($v_r = 0$) and
Case b: a hyperbolic expansion flow ($v_r \neq 0$)

as shown in Fig. 4 and Fig. 5, respectively. In both cases the expansion process is taken adiabatically for electrons and ions outside the nozzle.

With the knowledge of the flow and plasma properties (in first approximation), σ, β and v (or v_z, v_r for case b outside the nozzle) are also known, as well as their derivations. With these quantities one now solves the differential equation (24) by means of a finite differential method (Gauss-Seidel) for the current contour lines in first approximation. In Fig. 6abcd and Fig. 7abcd, the current contour lines are shown for Case a and Case b, respectively, assuming a fully ionized argon plasma. According to eq. (9a), one also obtains from Ψ the current density and the $\vec{j} \times \vec{B}$ force configuration within the discharge.

Step 2: One solves the expansion relation eq. (18) numerically by taking $(\vec{j} \times \vec{B})_z$ within the integral from Step 1. With that the velocity v(z) and the quantities p(z), ρ(z), n_e(z) are calculated in second order approximation and from that the new quantities for σ, β and v with their derivations.
With these new quantities, one now solves the differential equation (24) for the current contour lines by means of the same numerical method as in Step 1. In Fig. 8abcd, the current contour lines are shown for four current settings by taking a conical plume (Case a) outside the nozzle.

Step 3: By taking the new $(\vec{j} \times \vec{B})_z$ configuration from Step 2, one proceeds now in the same manner as shown in the step before.
In Fig. 9, the current contour lines are again shown for a current of 4000 A and compared with the results of Steps 1 and 2. Based on these results,

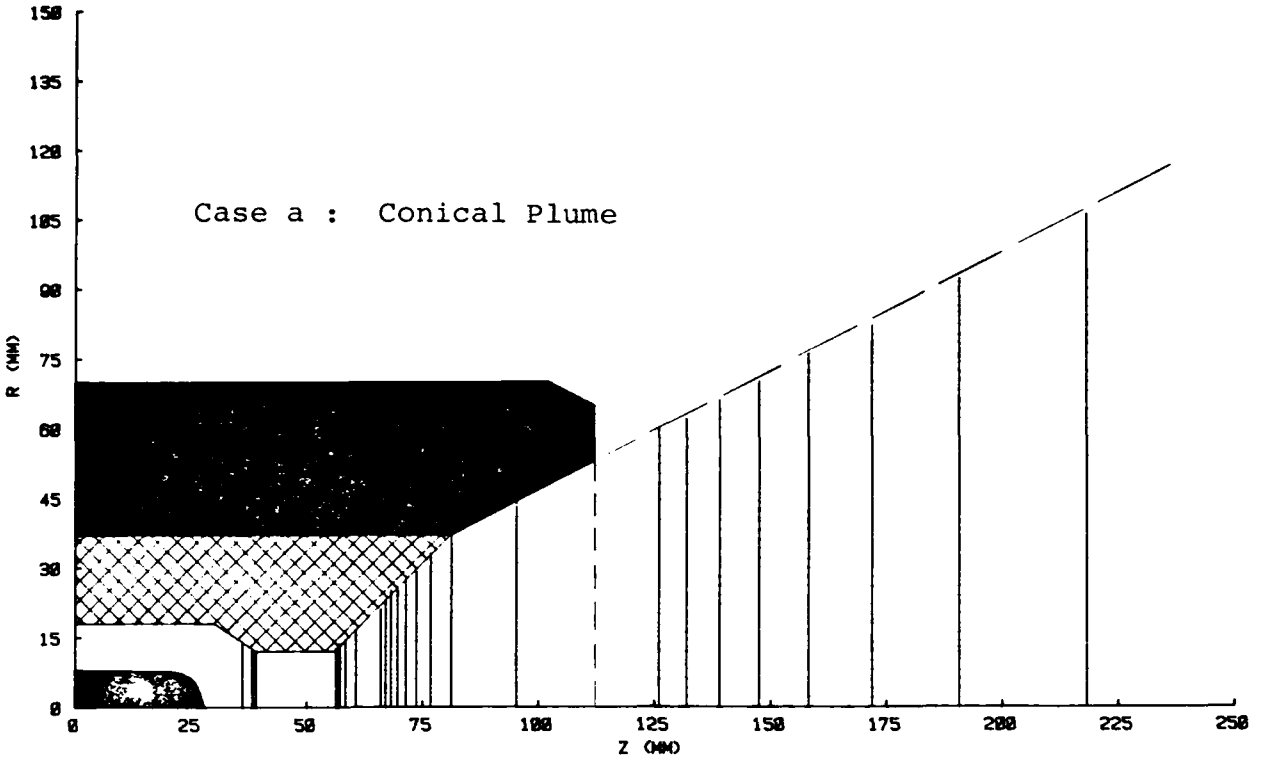

Fig 4 Jet plume conditions: conical expansion flow with constant density lines.

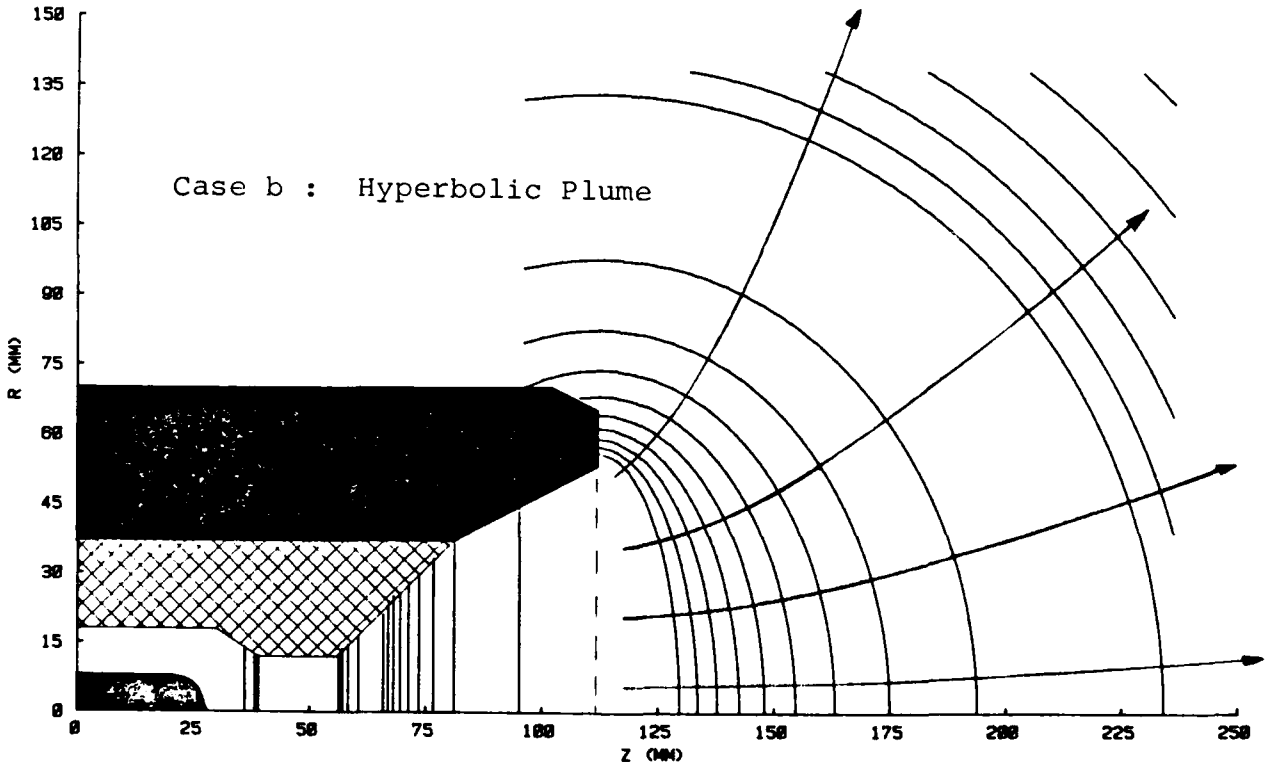

Fig 5 Jet plume conditions: hyperbolic expansion with constant density lines.

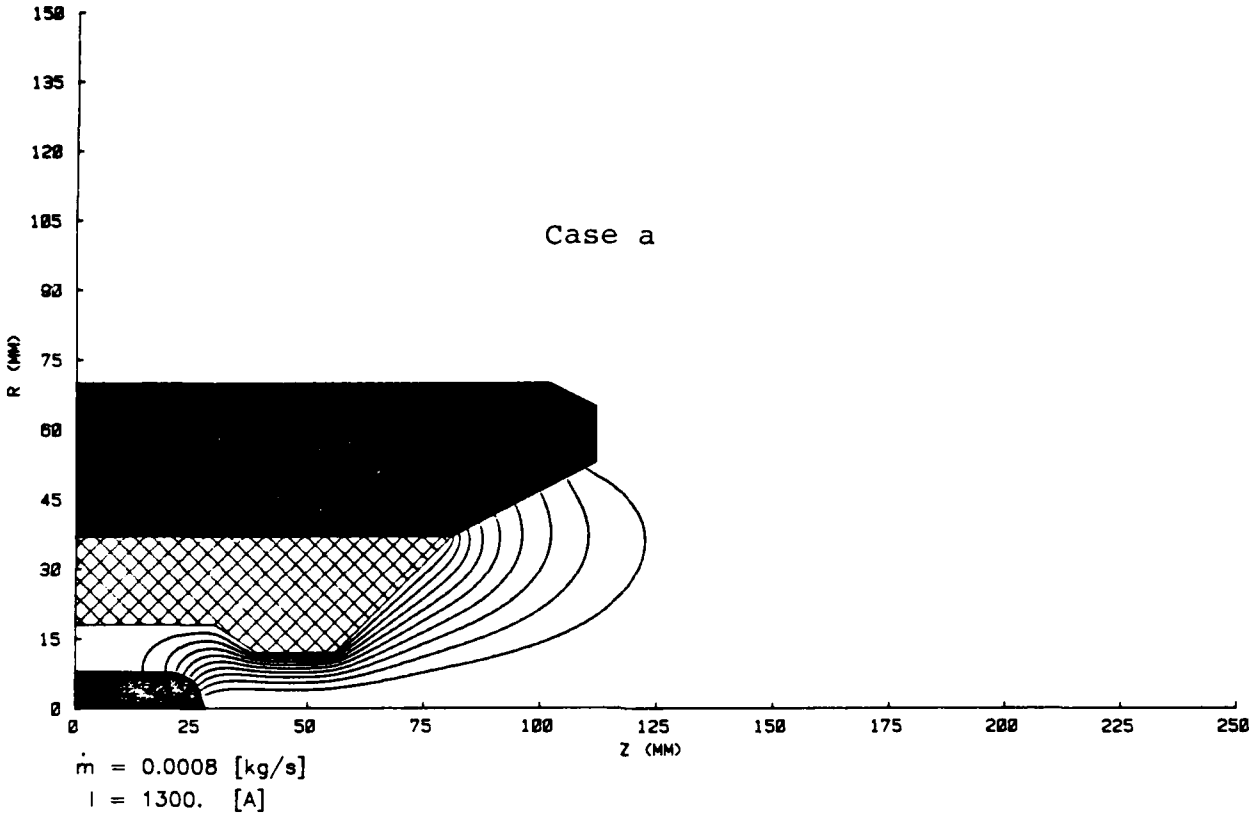

Fig 6a Current Contour Lines

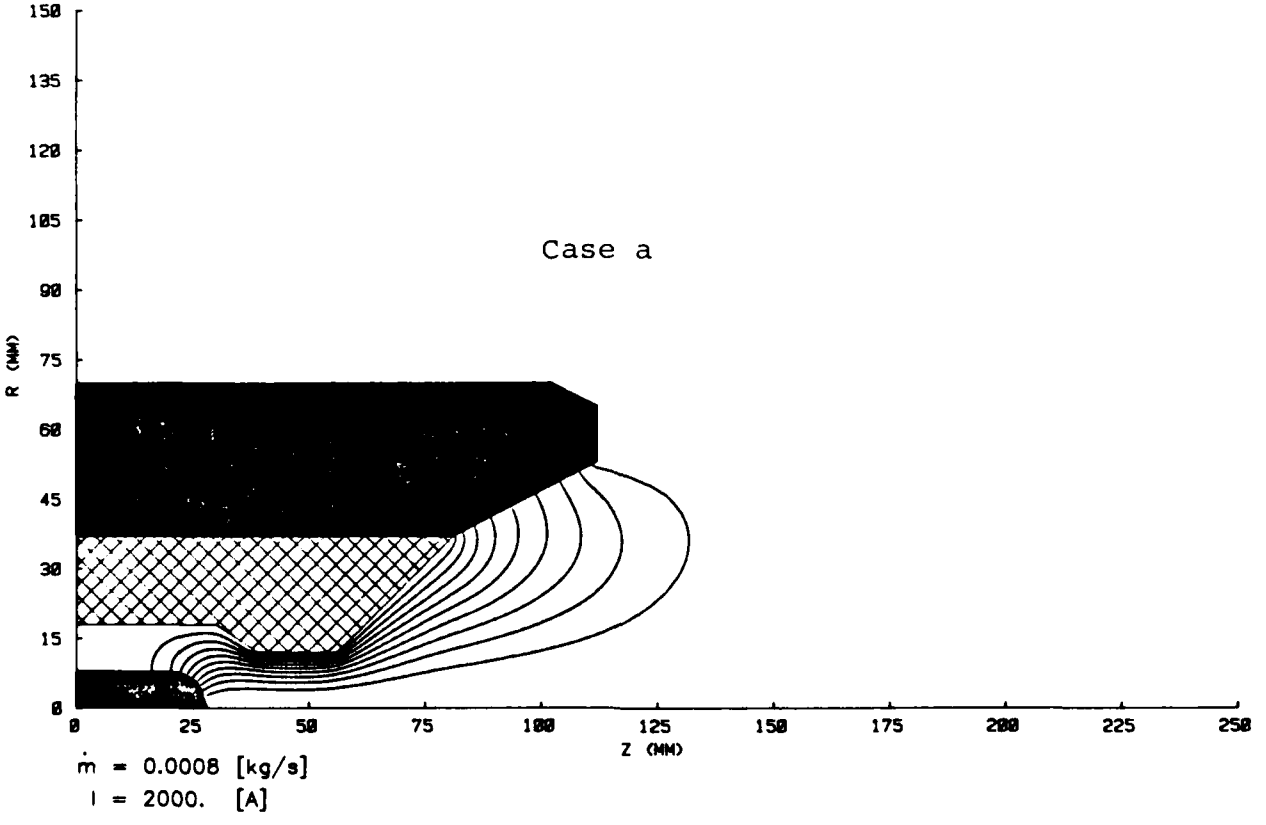

Fig 6b Current Contour Lines

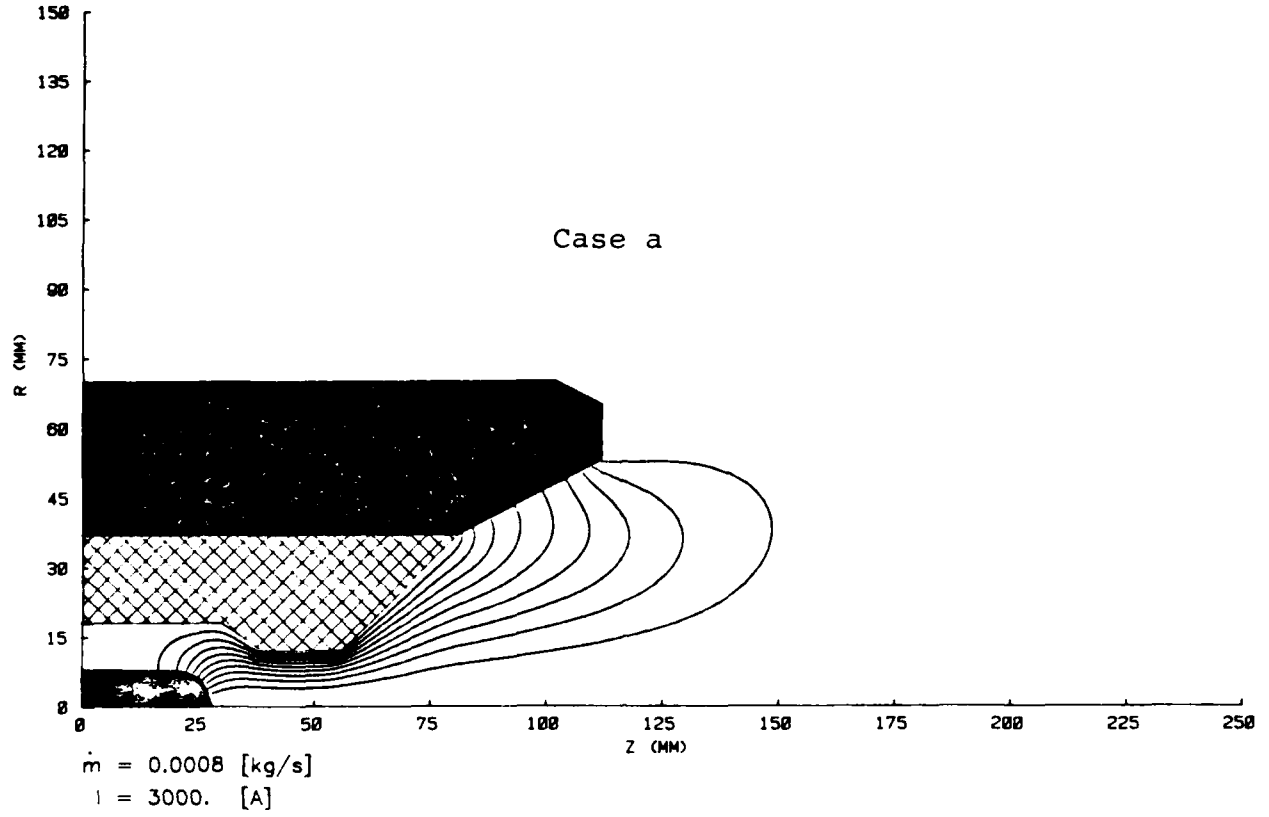

$\dot{m}$ = 0.0008 [kg/s]
I = 3000. [A]

Fig 6c Current Contour Lines

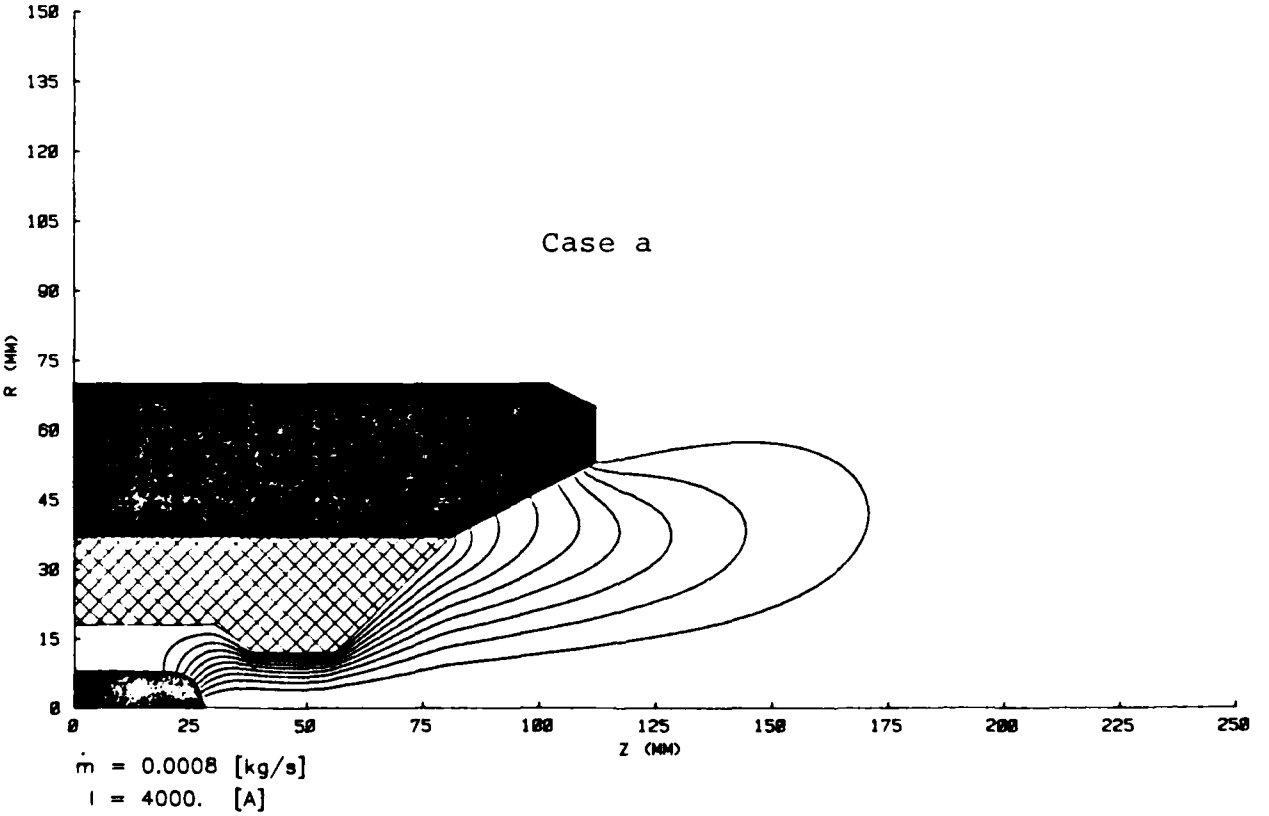

$\dot{m}$ = 0.0008 [kg/s]
I = 4000. [A]

Fig 6d Current Contour Lines

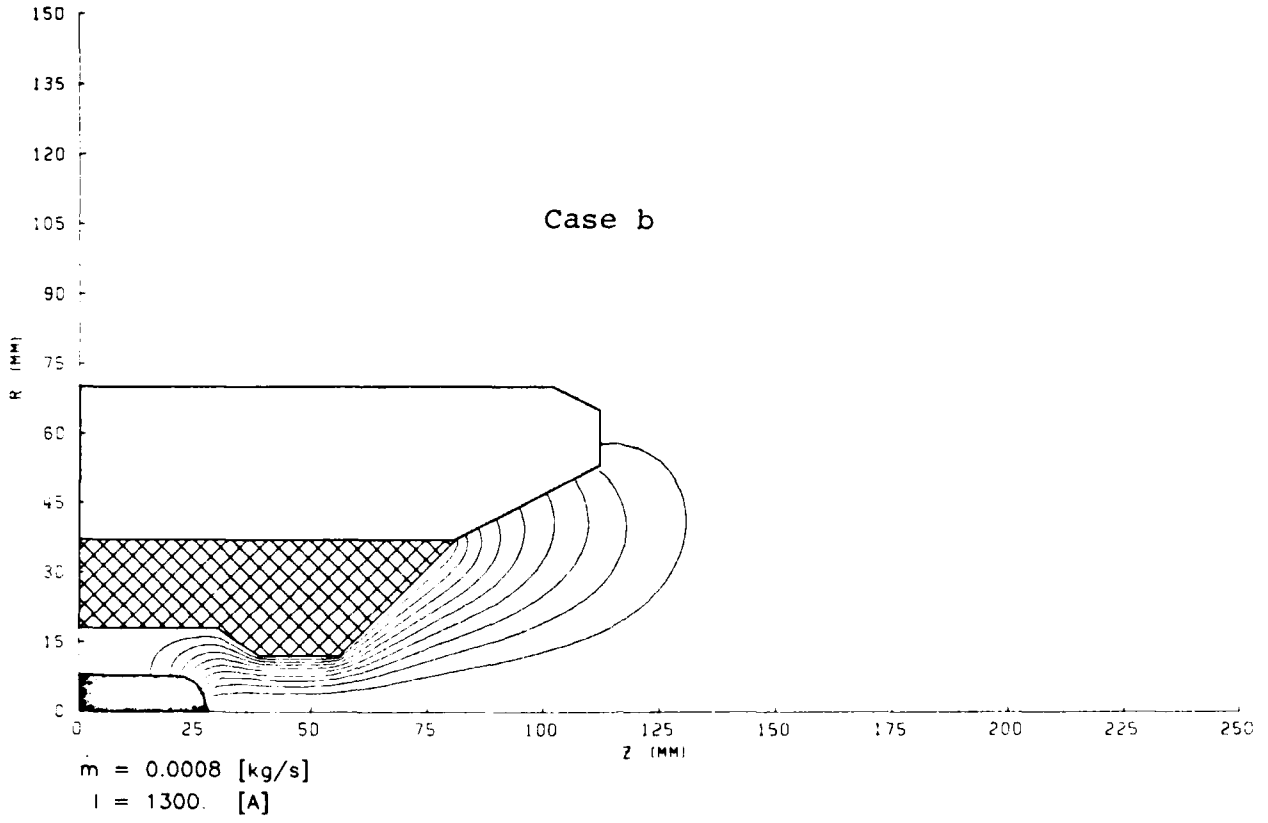

$\dot{m}$ = 0.0008 [kg/s]
I = 1300. [A]

Fig 7a Current Contour Lines

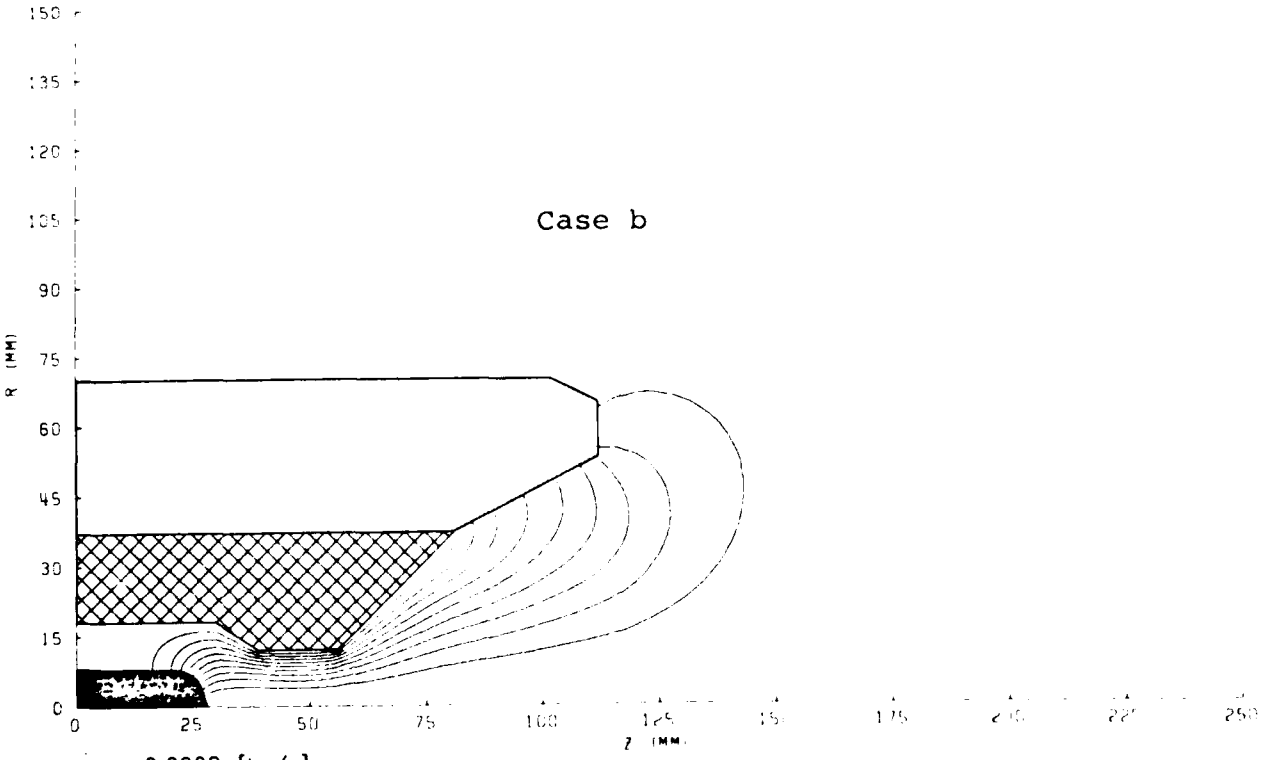

$\dot{m}$ = 0.0008 [kg/s]
I = 2000. [A]

Fig 7b Current Contour Lines

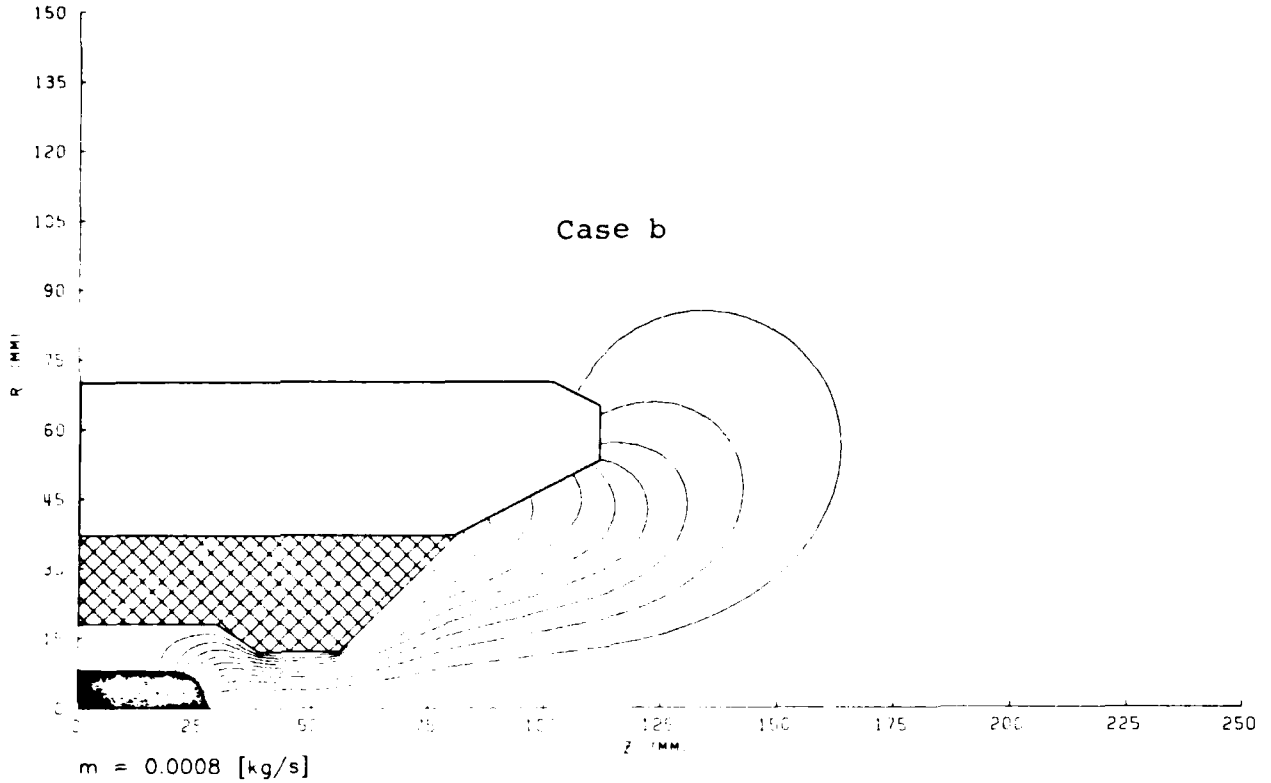

m = 0.0008 [kg/s]
I = 3000 [A]

Fig 7c Current Contour Lines

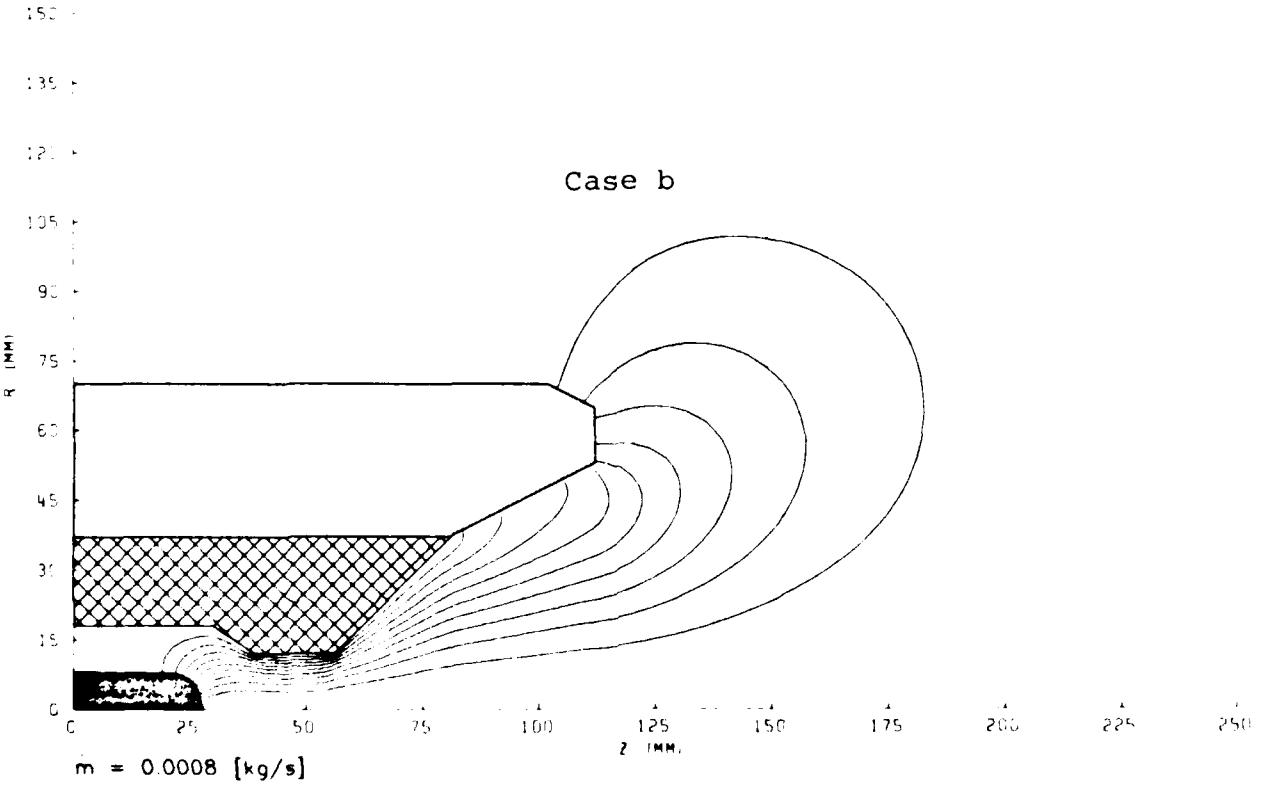

m = 0.0008 [kg/s]
I = 4000 [A]

Fig 7d Current Contour Lines

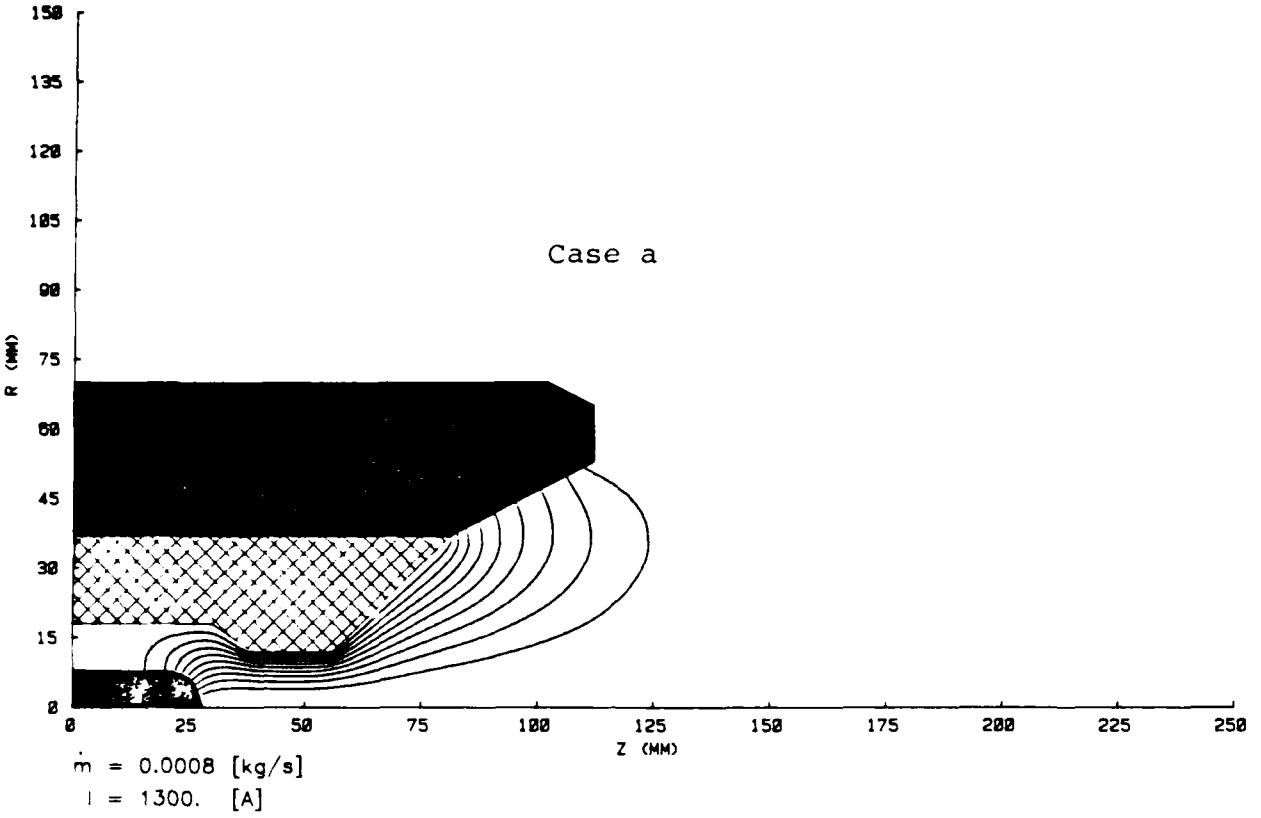

Fig 8a Current Contour Lines Step 2

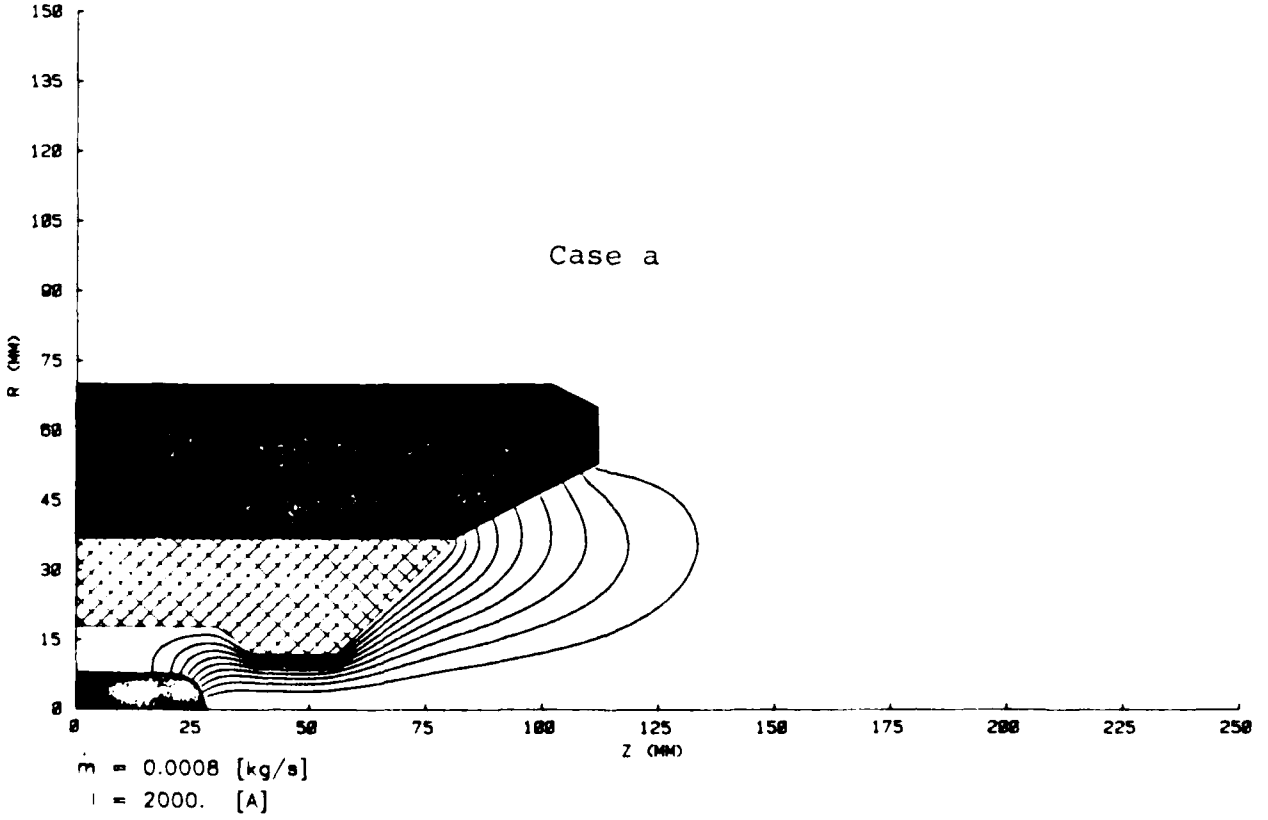

Fig 8b Current Contour Lines Step 2

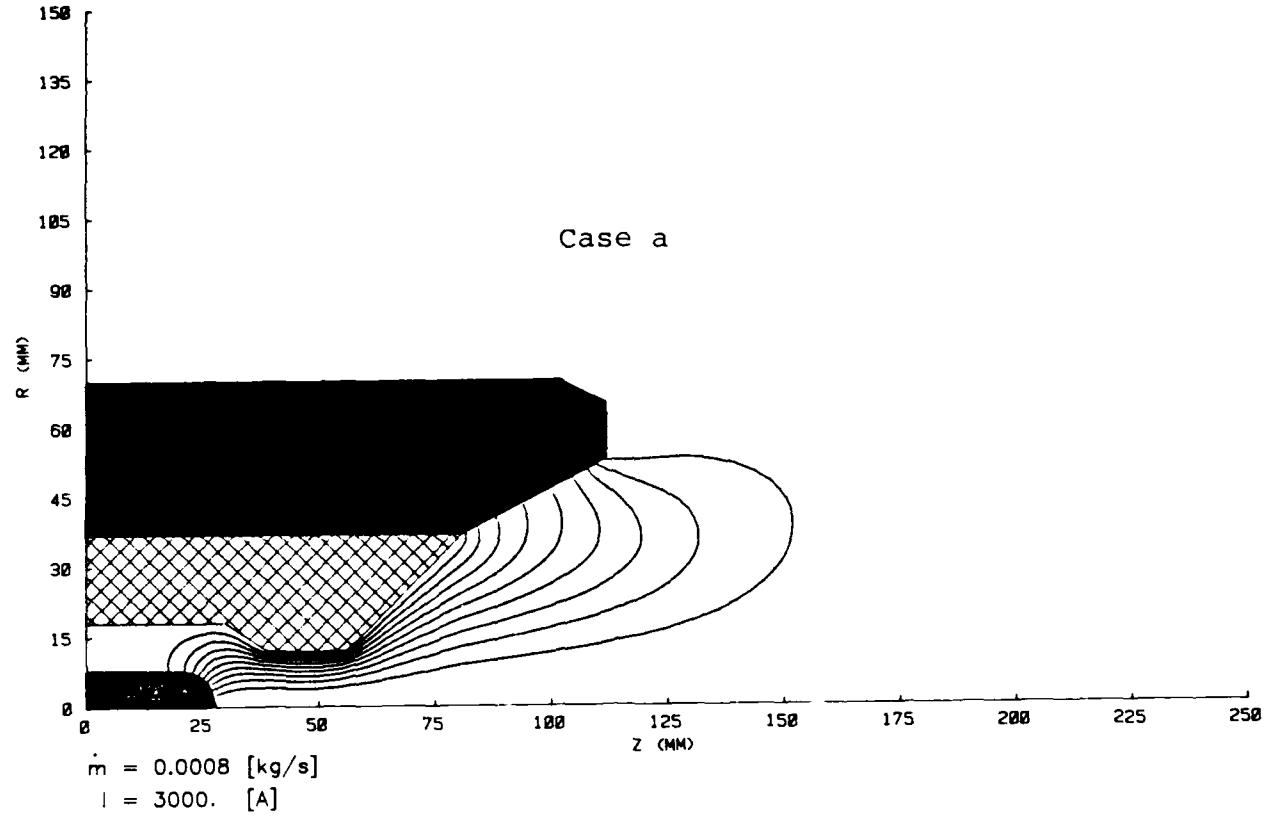

Fig 8c Current Contour Lines Step 2

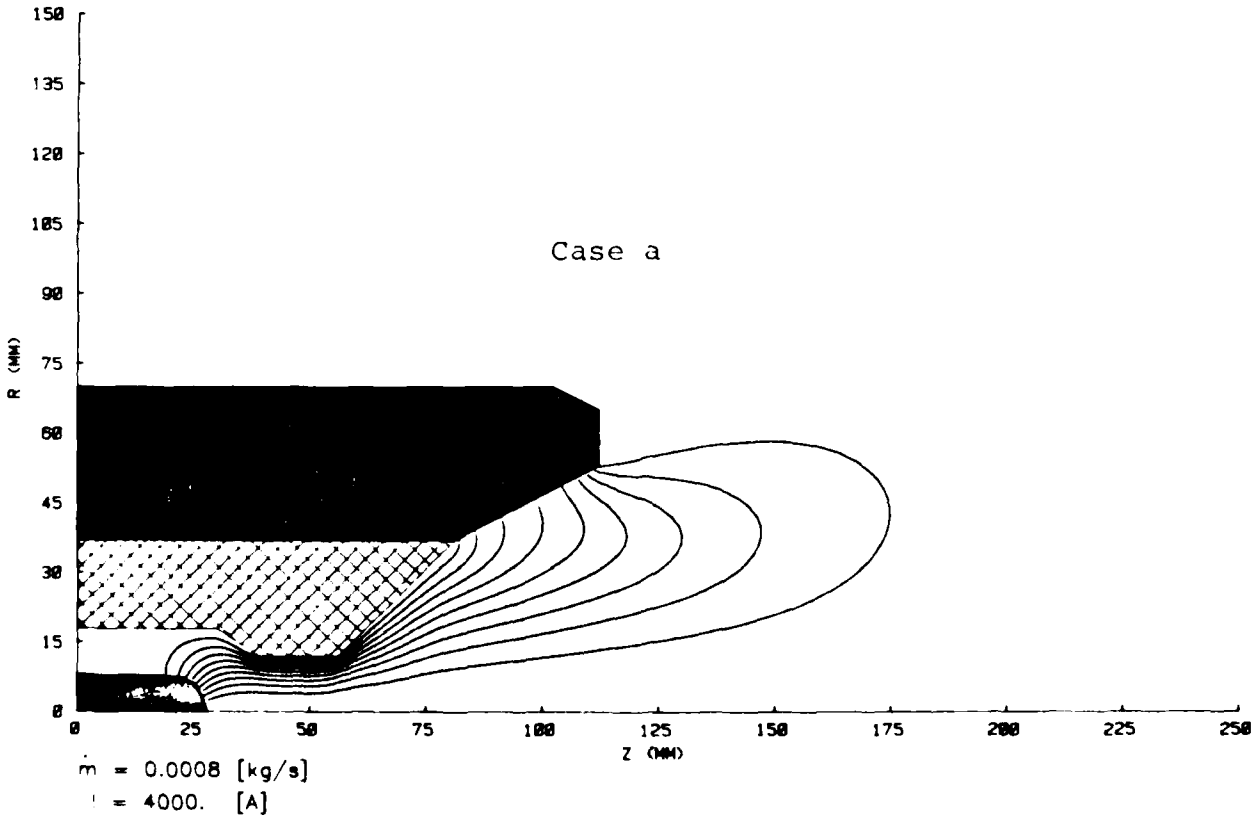

Fig 8d Current Contour Lines Step 2

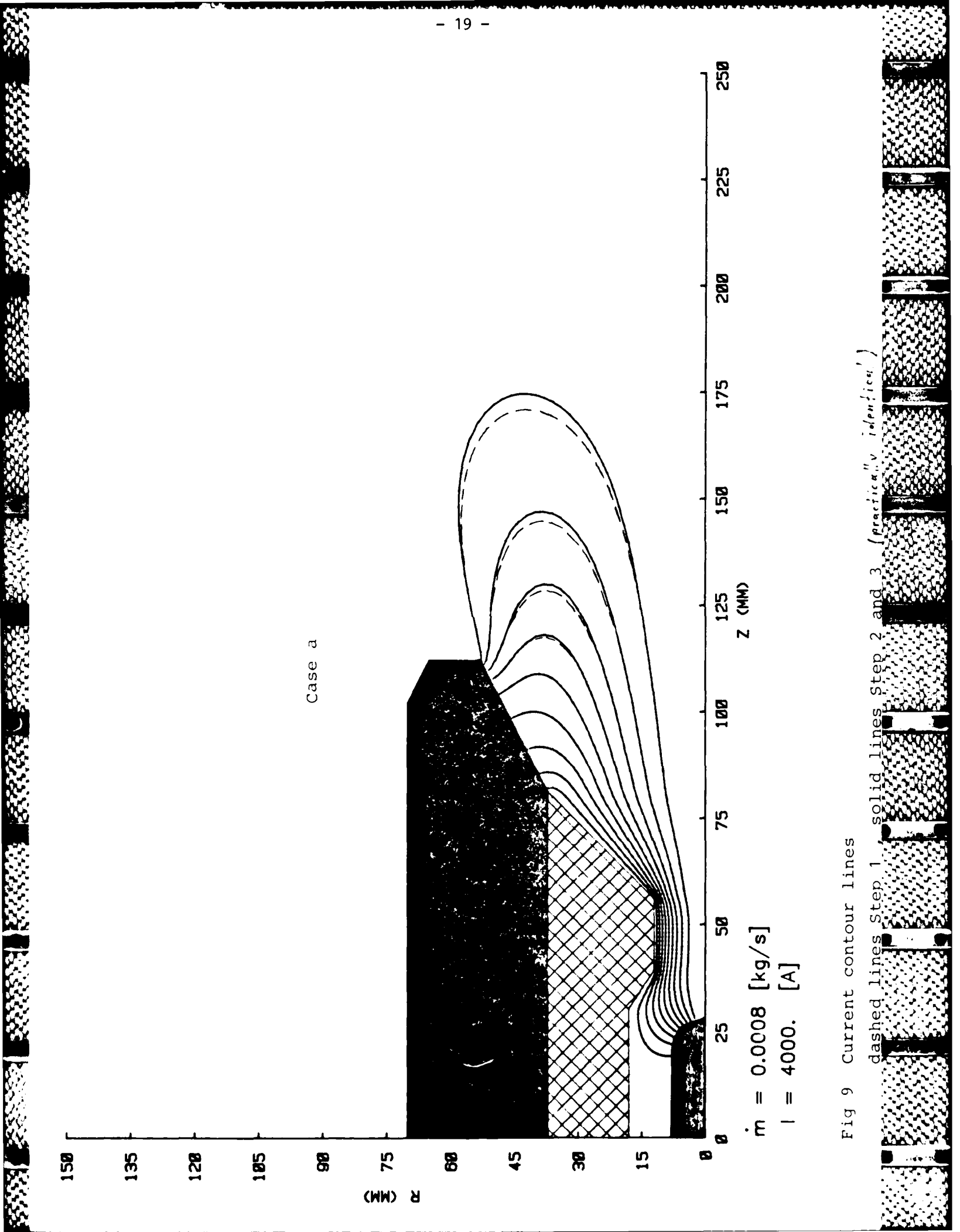

Fig 9 Current contour lines
dashed lines Step 1, solid lines Step 2 and 3 (practically identical)

one may conclude that after two steps the current contour lines do not change anymore and even a first step approach gives good results. This fact is the more valid since for lower current rates the deviation is even smaller.

Compared to this minor deviation between the results of Steps 1 and 2, the deviations between the contour lines of case (a) with a conical plume and case (b) with the hyperbolic expansion (see also Figs. 6abc and 7abc) outside the nozzle are much more pronounced. Nevertheless, for the low current of 1300 A both contour line patterns agree quite well with each other. In Figs. 10a and 10b, this calculated current pattern is compared with the experimentally measured contour lines of the same current and show good agreement for the 10% and even 20% current contour lines. The fact that in the measured case (Fig. 10b) the anode attachment is more concentrated downstream to the nozzle end than in the calculated case (Fig. 10a) may be attributed to the theoretical model which neglects the boundary layer along the nozzle and anode walls.

One is now able to calculate the thrust and the specific impulse according to the known $\vec{j} \times \vec{B}$ force configuration and the flow conditions after eq. (7) and eq. (8), respectively. The results of these calculations are shown by the upper curves in Figs. 11 and 12. Compared with the measured values they are by a factor of about two larger for small currents (1000-2000 A) and approach the experimental values within less than 20% at a current above 4000 A.

By properly matching the thrust coefficient c_{Th} and assuming an isothermal behavior for the electrons and heavy particles from the chamber on downstream to the nozzle throat, one may calculate the thrust according to eq. (1a). The chamber pressure p_0 can now be related to the nozzle throat conditions by

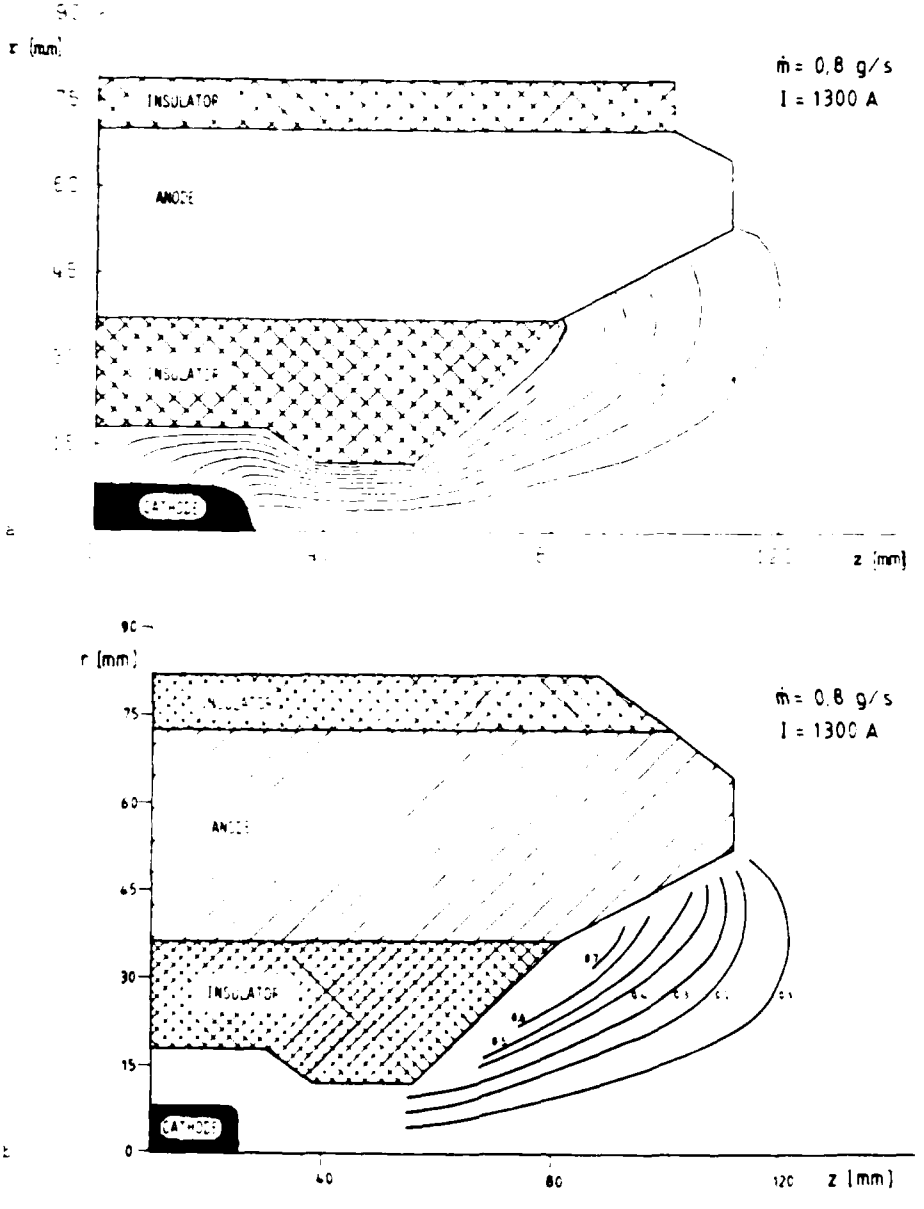

Fig. 10 a) Calculated and b) measured current contour lines of an MPD discharge in a nozzle-type plasma thruster.

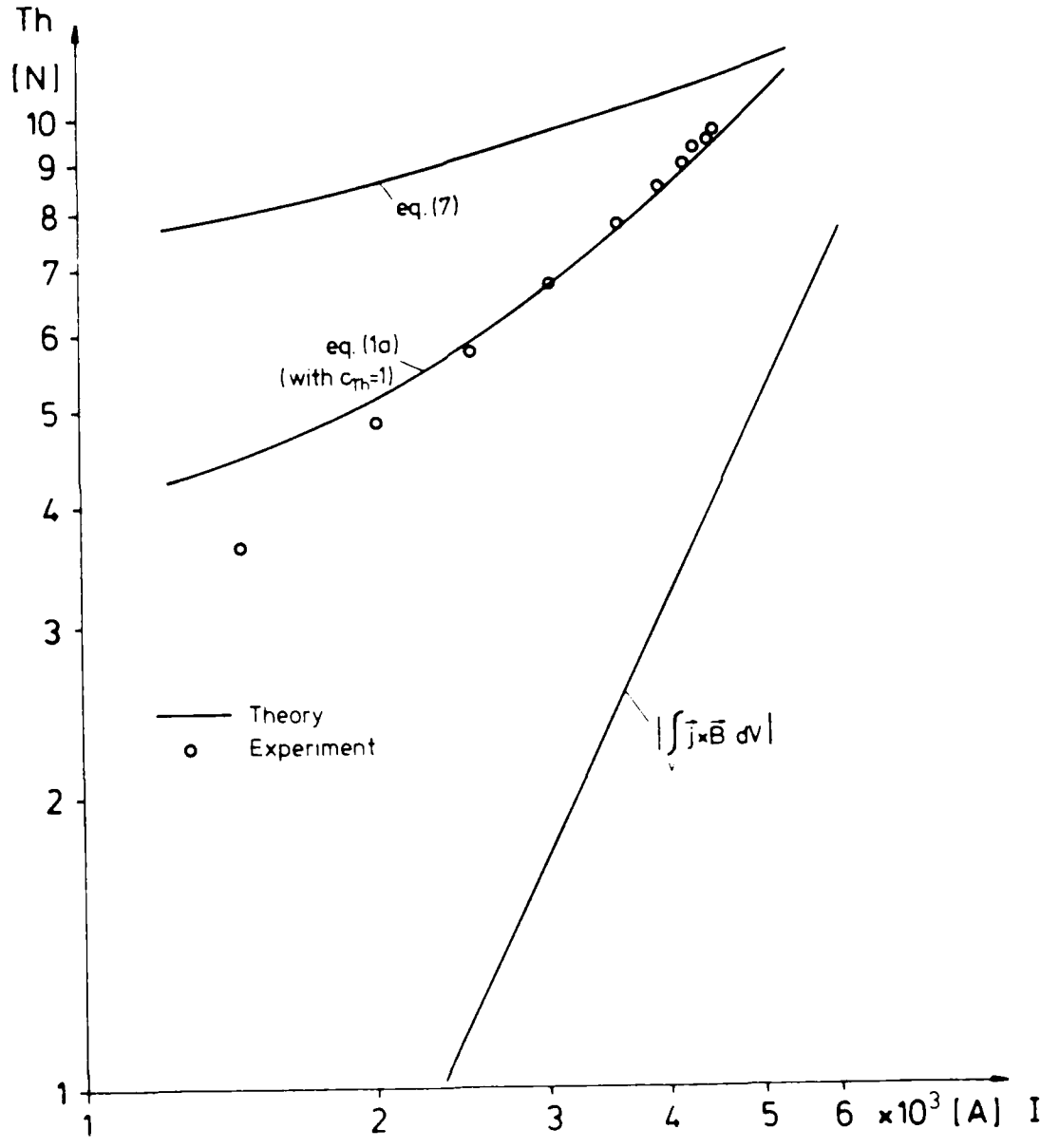

Fig. 11 Comparison between calculated and measured thrust of the Stuttgart self-field MPD thruster with argon as propellant.

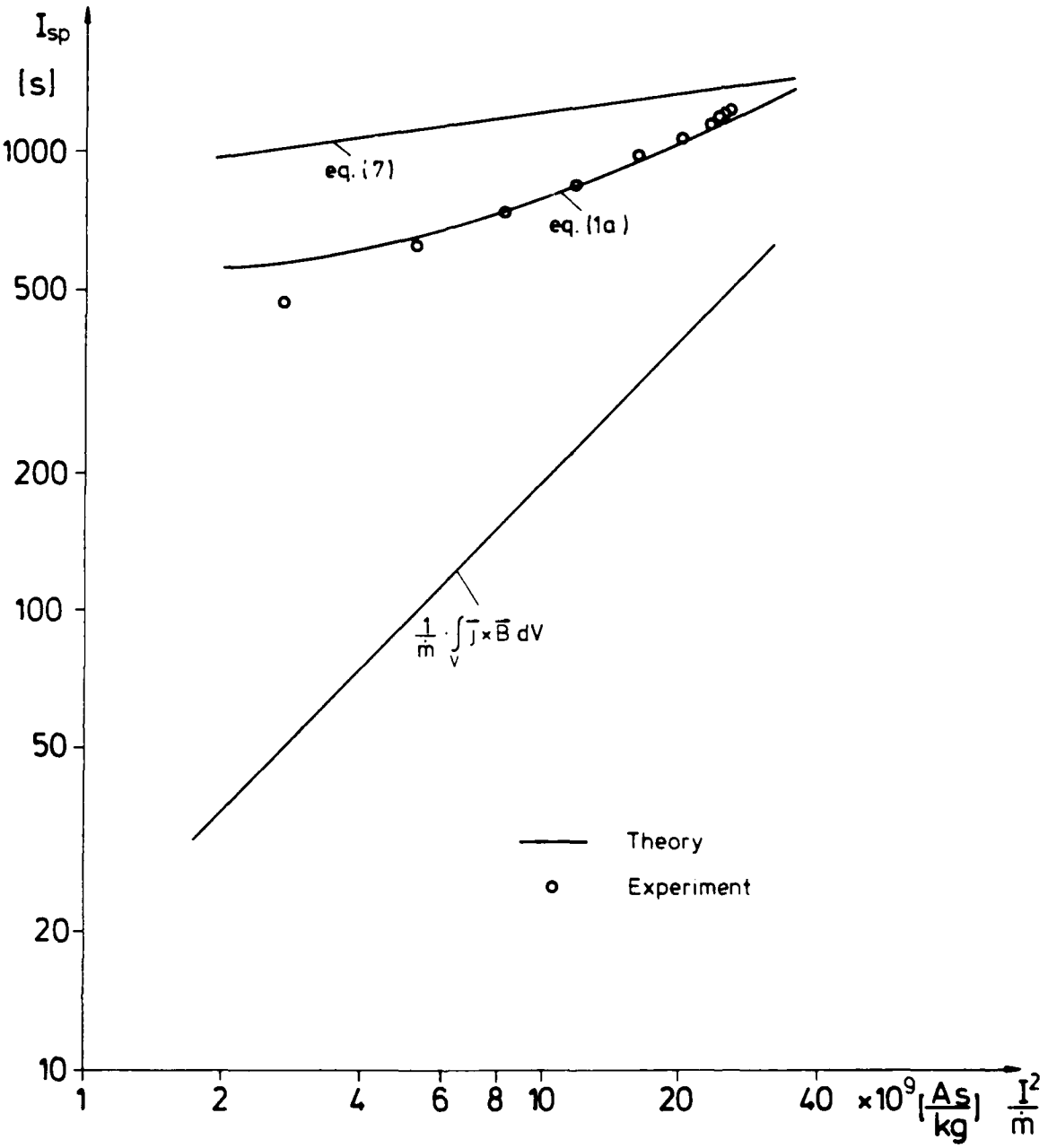

Fig. 12 Calculated specific impulse of the Stuttgart self-field MPD thruster.

$$p_0 = \frac{\dot{m}\, v_t}{A_t} \cdot 1.65 \qquad (26)$$

(see Appendix 3). If one takes $c_{Th} = 1$, the thrust follows by

$$Th = 1.65\, \dot{m} v_t + \left| \int_{V=V_1+V_2} \vec{j} \times \vec{B}\, dV \right| \qquad (27)$$

The result based on this formula is also shown as the middle line in Figs. 11 and 12.

As expected, they show excellent agreement with the experimental measurements in the upper current range ($I > 3000$ A), and even down to 1300 A the deviation is less than 30%. The pure electromagnetic thrust and the corresponding specific impulse curve are given by the lower curves in Figs. 11 and 12. One can see that the electromagnetic thrust reaches about 50% of the total thrust at a current of about 4500 A.

In order to investigate the radial effects of the $\vec{j} \times \vec{B}$ forces on the density distribution of electrons and ions, one assumes a balance between the radial $[\vec{j} \times \vec{B}]_r$ and pressure forces. The results of these calculations are shown in Fig. 13ab and Fig. 14ab for the two cases (a) and (b), respectively. In these model calculations the expansion process is taken similarly as in the examples before; however, now it is based on an average temperature and density across a nozzle cross section or across the ellipsoid area in case (b) for the flow outside the nozzle.

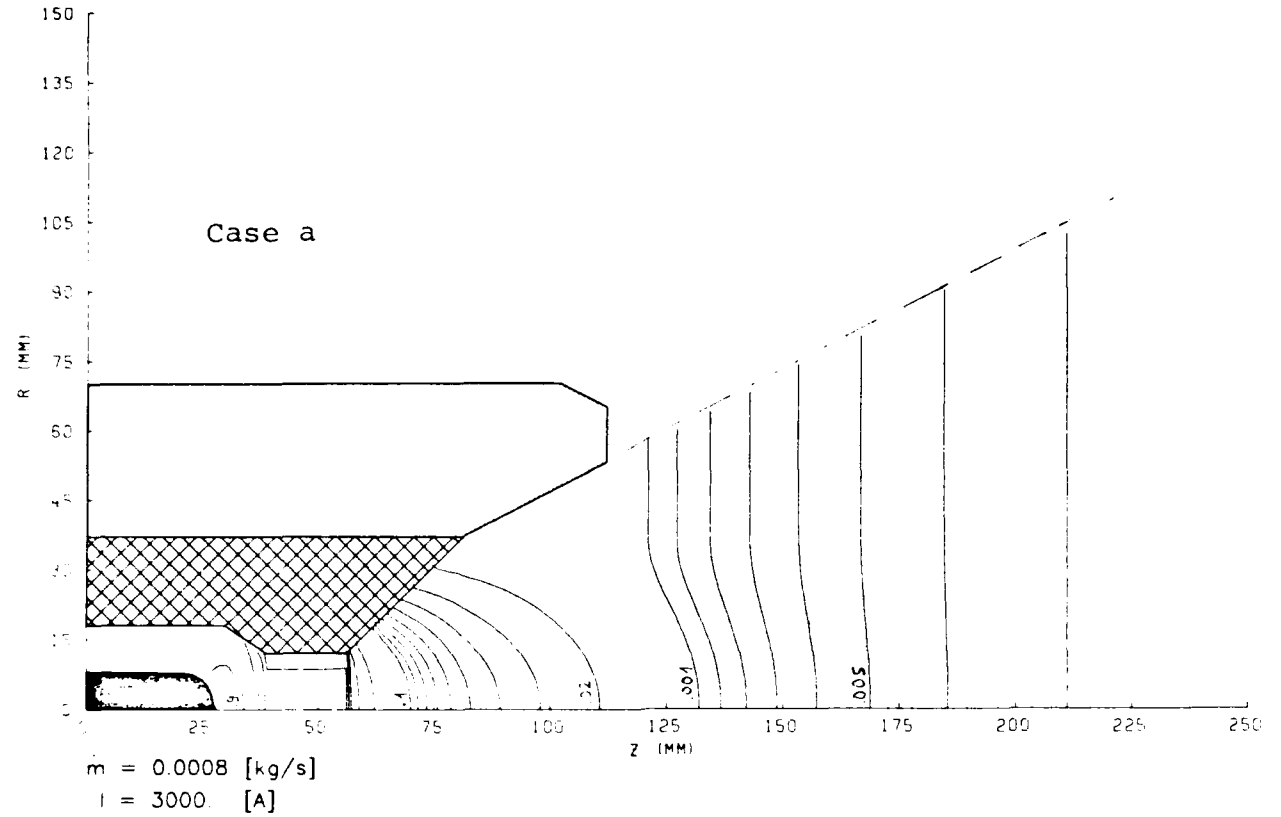

$\dot{m}$ = 0.0008 [kg/s]
I = 3000 [A]

Fig 13a Constant Density Lines

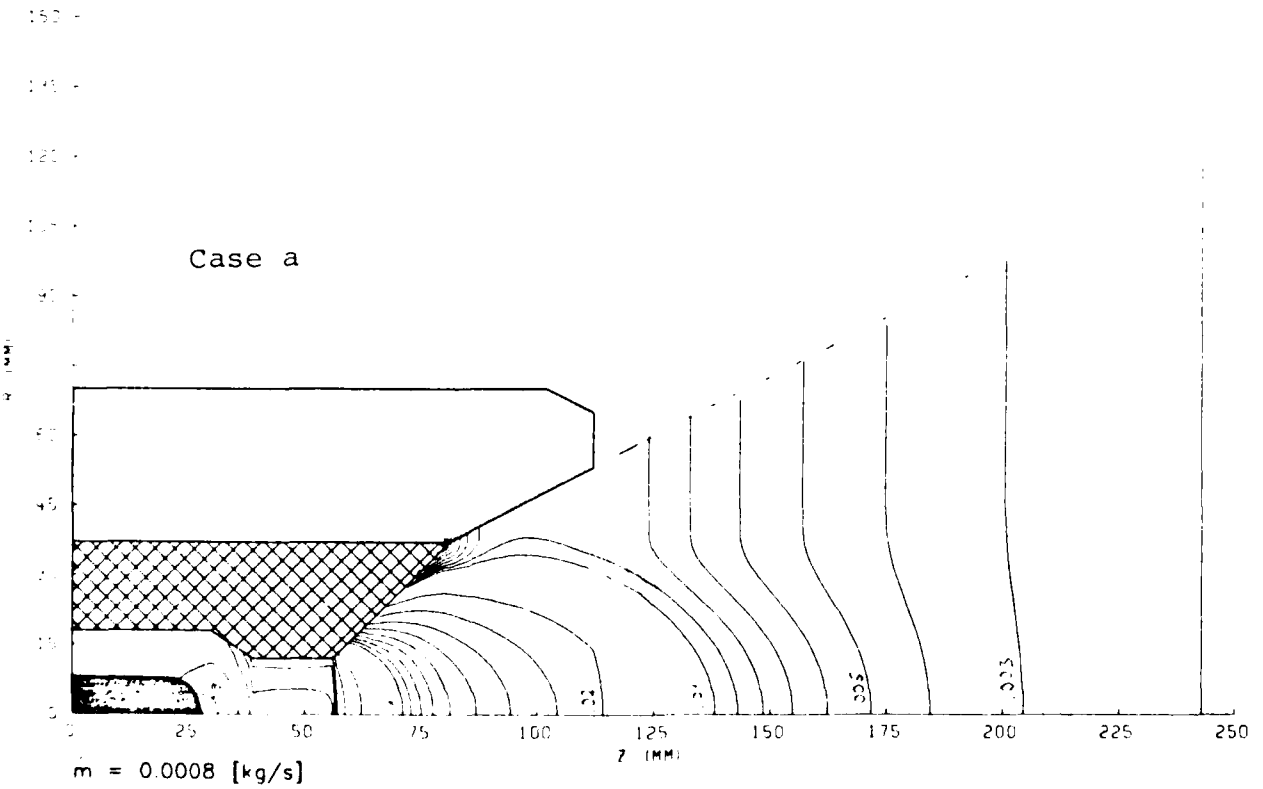

$\dot{m}$ = 0.0008 [kg/s]
I = 4000 [A]

Fig 13b Constant Density Lines

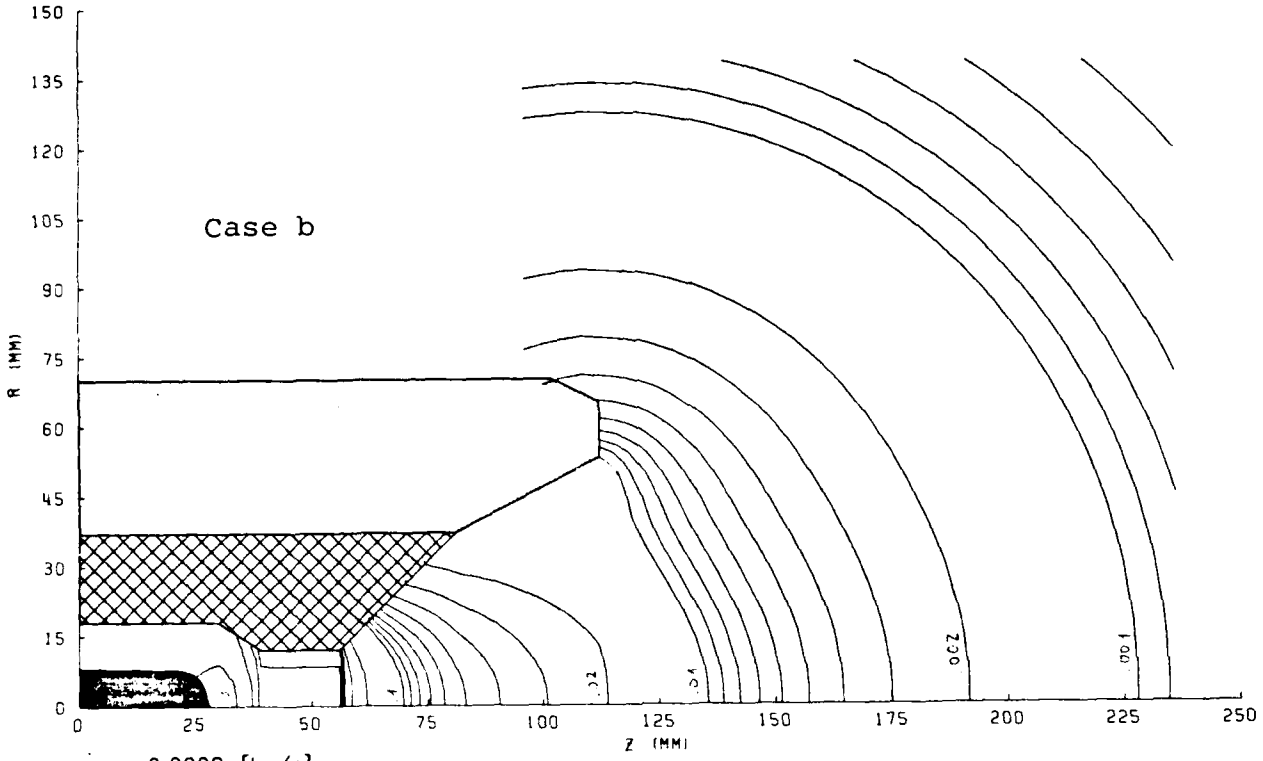

$\dot{m}$ = 0.0008 [kg/s]
I = 3000. [A]

Fig 14a Constant Density Lines

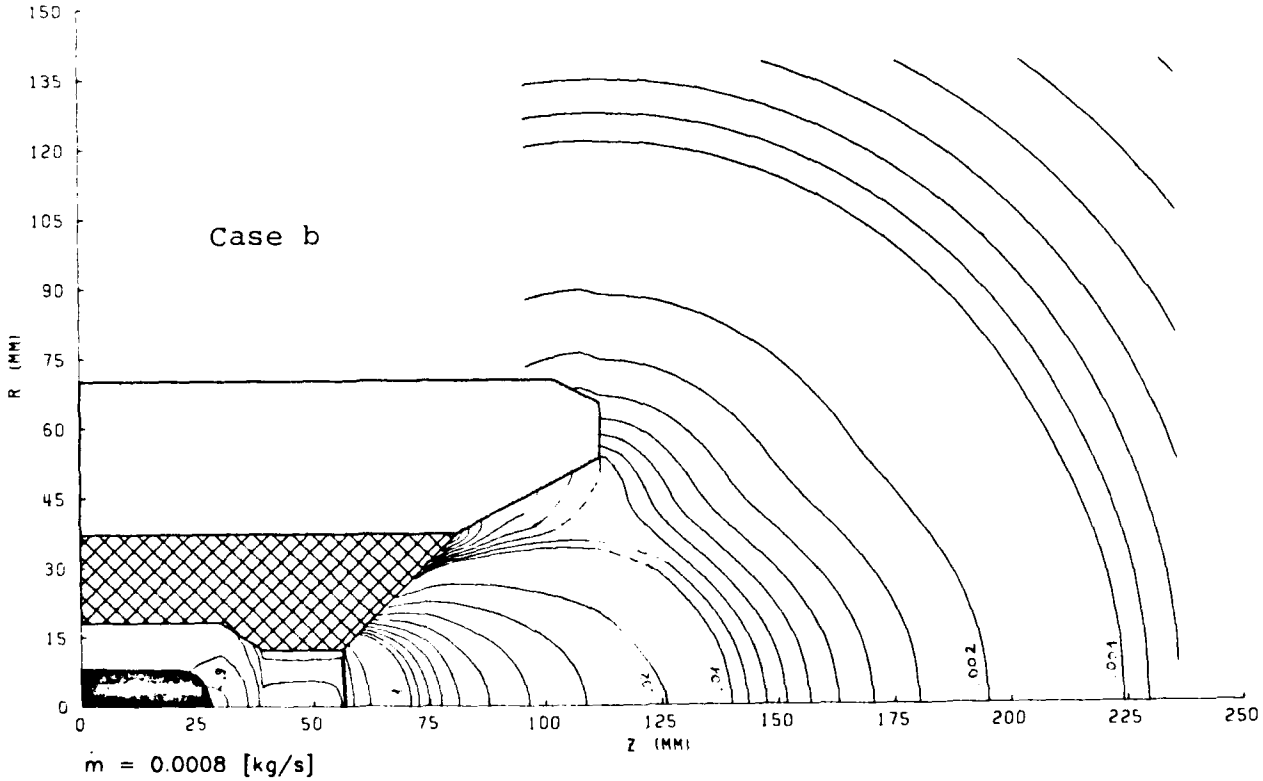

$\dot{m}$ = 0.0008 [kg/s]
I = 4000. [A]

Fig 14b Constant Density Lines

2.2 Cylindrical MPD Thruster Investigations
(Time Dependent Calculation)

In addition to the nozzle-type MPD arc, a detailed numerical code has been developed which allows the calculation of the plasma properties within a cylindrical MPD arc as shown in Fig. 15. This experimental thruster consists of a thoriated tungsten rod in the center and water-cooled ring segments, the last three of which can be either individually or all three together used as the anode. The propellant argon (or a hydrogen/nitrogen mixture) is fed through a small opening in the backplate and enters somewhat downstream of the flow discharge region. There it is heated up and axially accelerated due to the self-induced magnetic field effects. The thruster can be run in pulsed mode or continuously in steady state mode.

The geometrical configuration on which the computation is based is shown in Fig. 16. The radii of cathode and anode are taken according to the dimensions of the real device; however, the length of the cathode is assumed to be of the same length as the anode and matches the length of the three last segments (Anode 1, 2 and 3). The calculations are taken time-dependent and proceed in the following way:

The initial conditions are the total mass flow m_0, the temperature T_0, and the Mach number M_{a0}; likewise the current distribution at the starting time, $t = 0$ is assumed radially parallel and homogeneous from the anode to the cathode (see dotted line in Fig. 16). The current rise is taken according to a sine square function ($\sim \sin^2[\pi/2 \cdot t/t_0]$) and, after $t_0 = 200$ µs, reaches the plateau of its constant maximum value. For this current, the time dependent flow pressure and temperature field and the development of the current contour lines are numerically calculated.

The basic equations are the continuity equation, the two equations of motion in the r and z directions, and the energy equation

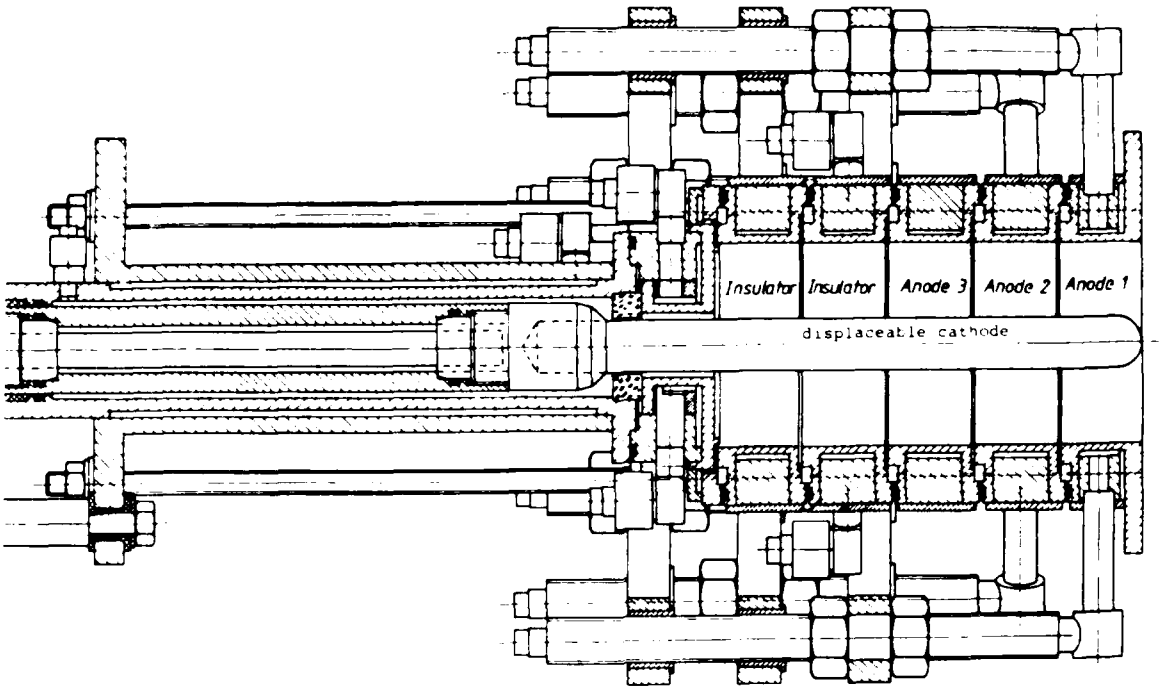

Fig. 15

Stuttgart University Cylindrical Continuous MPD Thruster ZT1

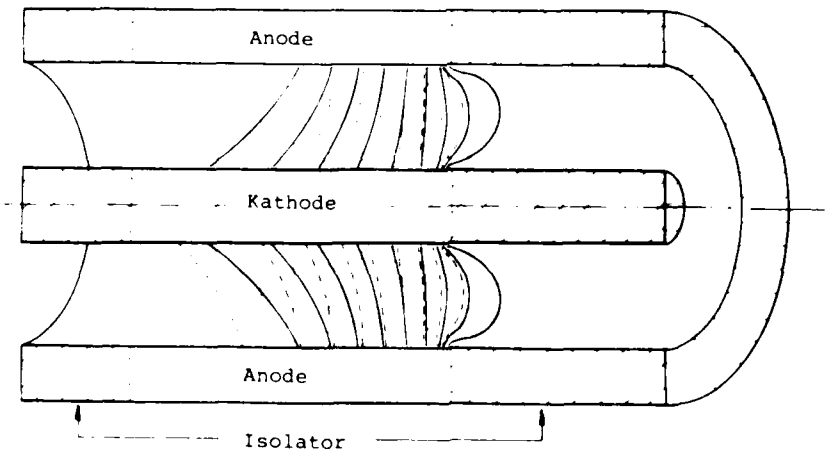

Fig. 16 Calculated current contour lines in a cylindrical MPD thruster. Dotted lines at t = 20 μs, dashed lines after 160 μs, and solid lines after 200 μs.

$$\left|\begin{matrix}\rho\\ \rho v\\ \rho u\\ e\end{matrix}\right|_t + \left|\begin{matrix}\rho v\\ p+\rho v^2\\ \rho vu\\ (p+e)v\end{matrix}\right|_r + \left|\begin{matrix}\rho u\\ \rho uv\\ p+\rho u^2\\ (p+e)u\end{matrix}\right|_z + \left|\begin{matrix}\rho v/r\\ \rho v^2/r - j_z xB\\ \rho vu/r - j_r xB\\ (p+e)\frac{v}{r} - \vec{j}^2/\sigma\end{matrix}\right| = 0 \qquad (28)$$

which are iteratively solved for a given current contour by an extended MacCormack Code, as well as the Maxwell's equation and Ohm's Law

$$\nabla \times \vec{B} = \mu_0 \vec{j} \qquad (29)$$

$$\nabla \cdot \vec{B} = 0 \qquad (30)$$

$$\vec{j} = \sigma\left(\vec{E} + (\vec{w} \times \vec{B})\right) - \frac{\omega\tau}{B}\left(\vec{j} \times \vec{B}\right) \qquad (31)$$

which yield the current contour lines for a given temperature, pressure and flow field by means of a Relaxation Gauss-Seidel Code similar to that described in Section 2.1.

The calculations proceed now in small time steps, in which for a given current contour the new pressure, temperature and flow fields are calculated by means of an extended MacCormack Code. With these new data, a new current contour is determined for the next time step with the new total current by means of a Relaxation Gauss-Seidel Code, and so on. This iterative program is quite extensive and needs the relatively large computing time of 30-50 min on the Cray 2 at the Computer Center of the University of Stuttgart. The results so far are quite promising and are based on the following initial values

$\dot{m}_0$ = 20 g/s argon

T_0 = 8000 K

M_{a_0} = 1.2

and the time function of the current given by

$$I(t) = I_{Max} \sin^2 \frac{\pi}{2t_0} t$$

with t = 200 µs, I_{Max} = 10 kA

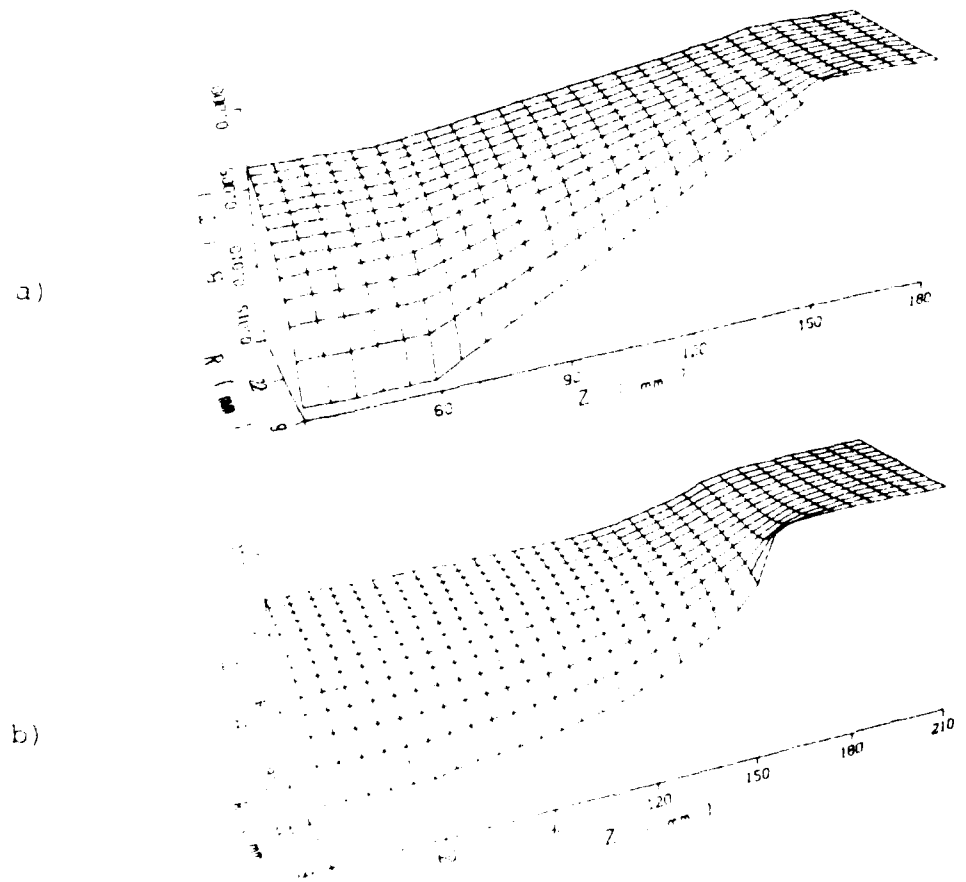

Fig. 17 Initial values of the magnetic induction for a current maximum of 12 kA a) after 20 µs, b) after 200 µs.

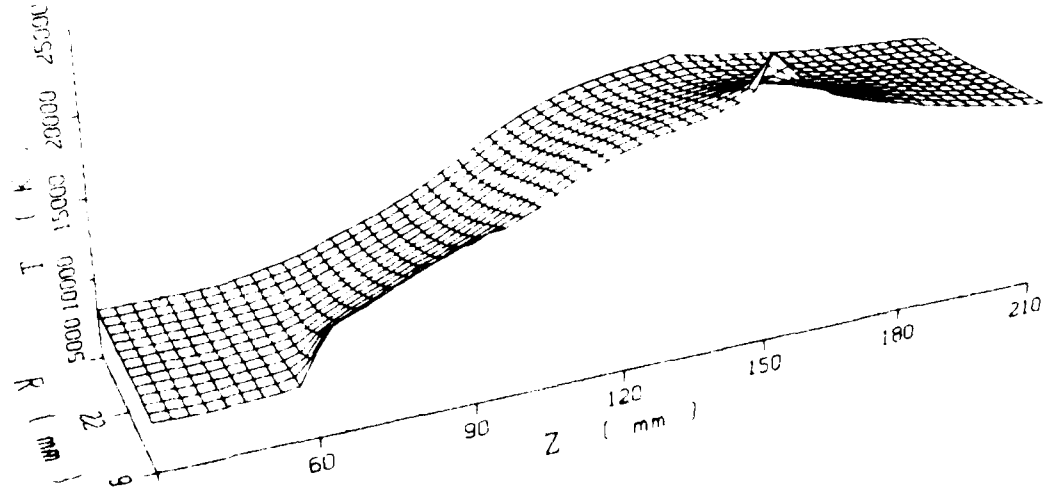

Fig. 18 Temperature distribution in a cylindrical MPD accelerator after 200 µs.

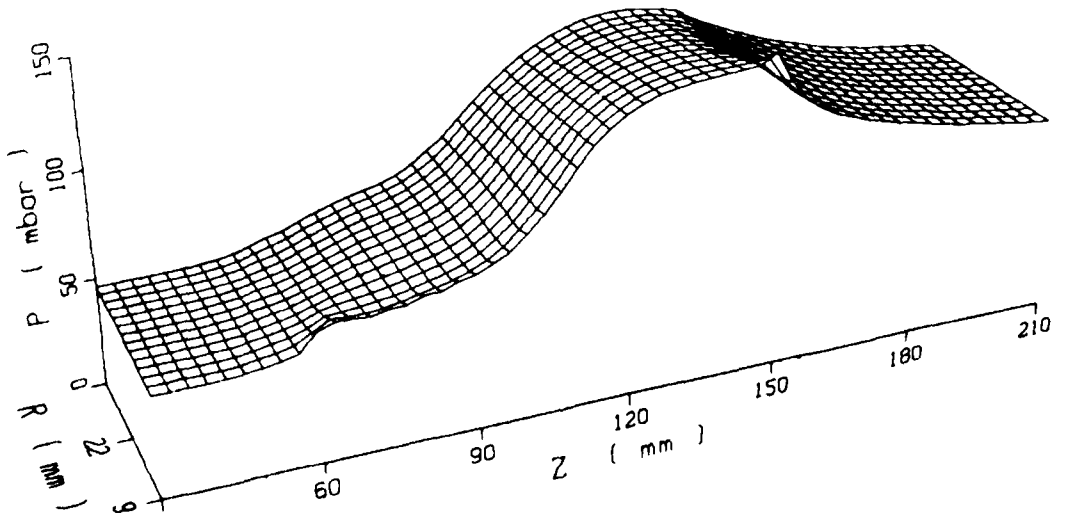

Fig. 19 Pressure distribution in a cylindrical MPD accelerator after 200 µs.

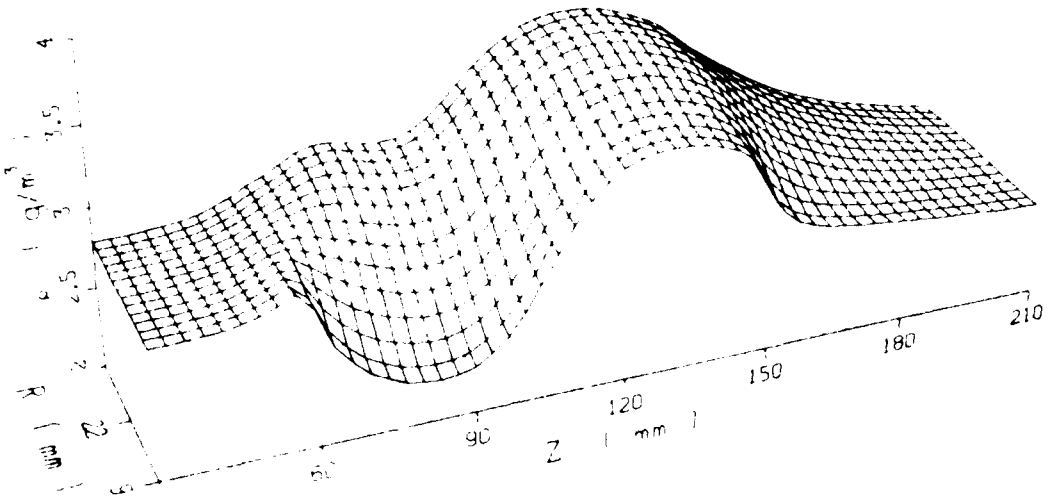

Fig. 20 Density distribution in a cylindrical MPD accelerator after 200 μs.

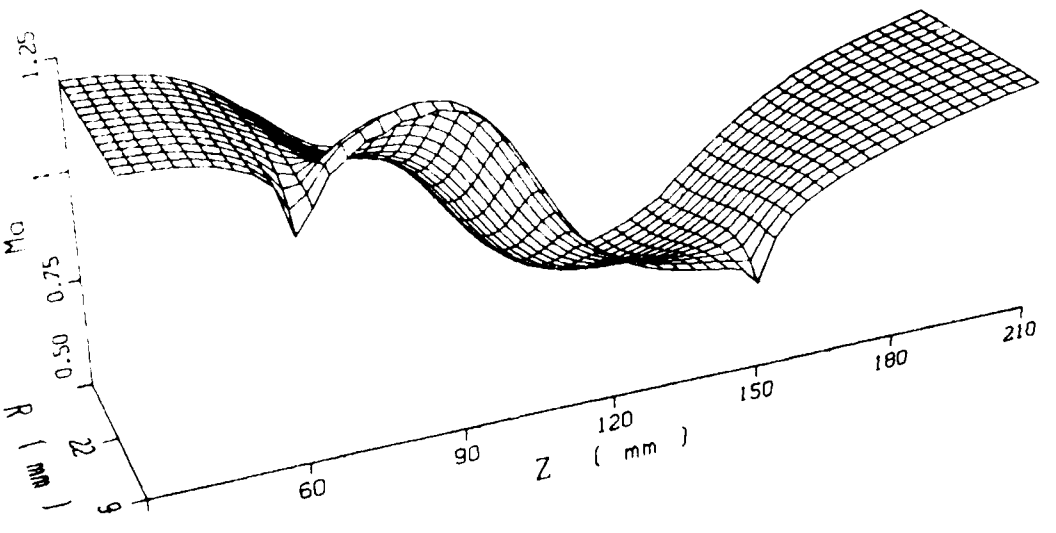

Fig. 21 Mach number distribution in a cylindrical MPD accelerator after 200 μs.

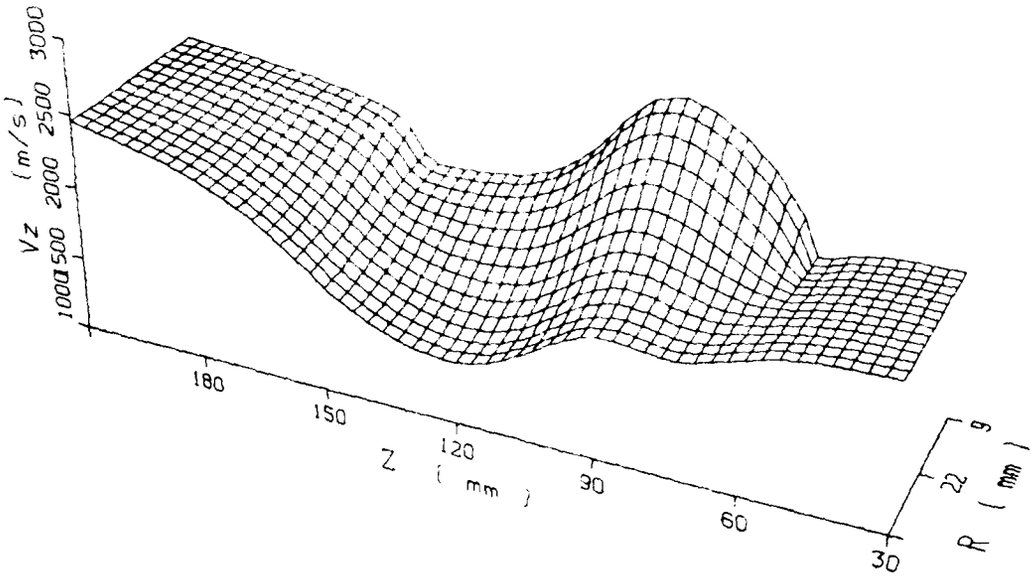

Fig. 22a Axial velocity distribution in a cylindrical MPD accelerator after 200 μs.

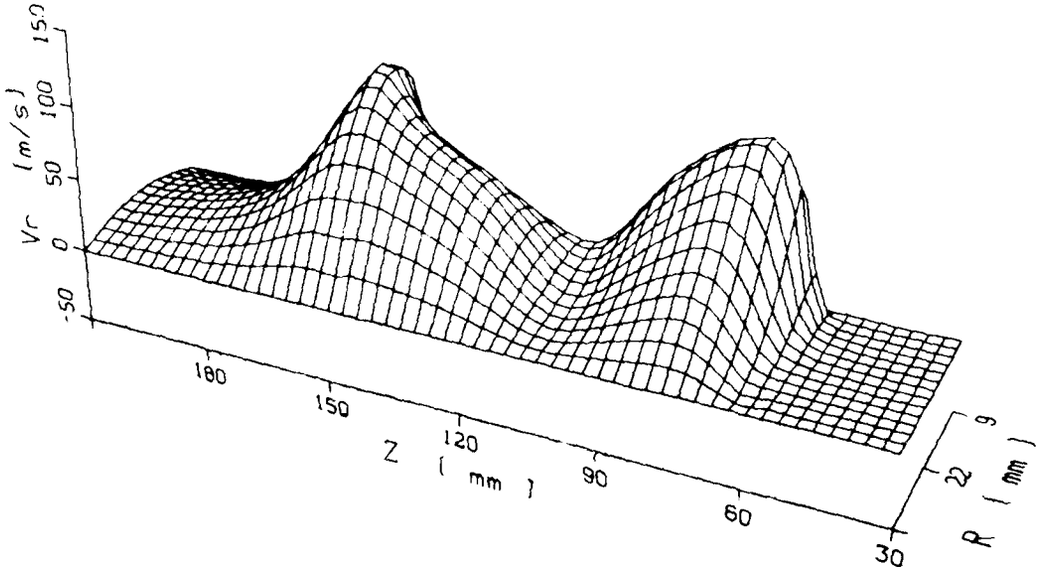

Fig. 22b Radial velocity distribution in a cylindrical MPD accelerator after 200 μs.

3. Stability Theory

3.1 General Theory

The stability behavior of a current-carrying plasma channel has been discussed based on a unique theoretical approach. One considers any arbitrarily configuratin of such a channel within a fixed laboratory system (x_L, y_L, z_L; see Fig. 23). The theory starts from the equation of motion, the continuity equation and the Maxwell's equation

$$\frac{\partial}{\partial t}\left(\rho \vec{v}_L\right) + \nabla\left\{\rho \overleftrightarrow{v_L v_L} + \ddot{P}\right\} = \vec{j} \times \vec{B} \tag{32}$$

$$\frac{\partial}{\partial t}\rho + \nabla\left(\rho \vec{v}_L\right) = 0 \tag{33}$$

$$\nabla \times \vec{B} = \mu_0 \vec{j} \tag{34}$$

$$\nabla \vec{B} = 0 \tag{35}$$

where

ρ = Plasma density

$\vec{v}_L$ = Plasma velocity measured within the laboratory frame of reference

$\overleftrightarrow{v_L v_L}$ = Tensor dyode of $\vec{v}_L$

$\ddot{P}$ = Pressure tensor

$\vec{j}$ = Electric current density

$\vec{B}$ = Magnetic Induction

One now replaces the velocity vector $\vec{v}_L$ of the fixed system (x_L, y_L, z_L) by

$$\vec{v}_L = \vec{v} + \vec{v}_s \tag{36}$$

i.e. the sum of the plasma velocity $\vec{v}$, measured within the channelbound system (x,y,z; see Fig. 23) and the axis velocity $\vec{v}_s$ which has only transverse components with respect to the channel axis

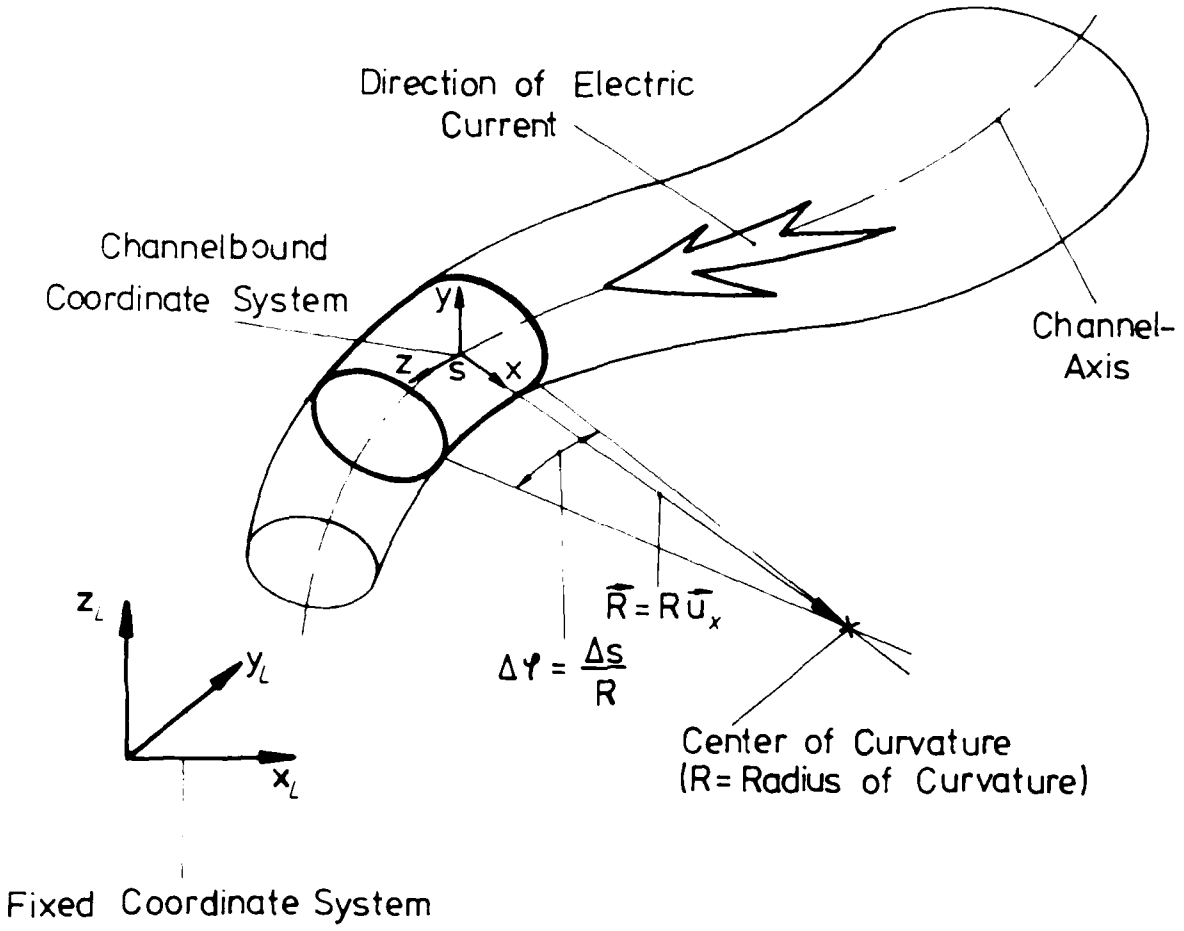

Fig. 23 : Illustration of the Channelbound (x, y, z) and the Fixed (x_L, y_L, z_L ; with respect to the Laboratory frame of reference) Coordinate System.

$$\vec{v}_s = \begin{bmatrix} v_{sx} \\ v_{sy} \\ 0 \end{bmatrix} \tag{37}$$

After integration of the equation of motion over a channel segment of length Δs (see Fig. 23) one eventually obtains the force balance for the channel segment in the form

$$(\Delta m) \frac{d\vec{v}_s}{dt} = \vec{X}\, \Delta s \tag{38}$$

where $\Delta m = \int_{\Delta V} \rho \, dV$ is the mass of the plasma within the segment of volume ΔV and length Δs

$\vec{X}\, \Delta s$ is the sum of all forces which act on the segment and accounts for

a) all gas dynamic surface forces like propelling, friction, and pressure effects
b) the volume forces due to electromagnetic effects between the current-carrying elements inside and outside the segment and
c) all fictitious forces like Coriolis and centrifugal forces due to an axial flow within a curved and/or twisted current-carrying plasma channel.

This force $\vec{X}$ per unit channel length has now been calculated among others as a function of the local channel geometry like channel radius r_0, axis curvature R, channel twist, convergence or divergence, and also as a function of the channel orientation with respect to an applied magnetic field, $\vec{B}_0$ and/or flow field.[2] The transverse and axial component of $\vec{X}$ follows by

---

[2] H. O. Schrade, "Magnetoplasmadynamic Effects in Electric Arcs," Interim Scientific Report, AFOSR 82-0298, Aug. 1983.

$$\vec{X}_{\perp} = \{\frac{1}{2\mu_0} \int_{A_z} \vec{B}_s^{\,2}\, dA_z + \frac{\mu_0}{8\pi} I^2 \left[1 + \frac{r_0}{R}\left(\alpha + \frac{3}{4}\frac{r_0}{R}\right)\right]$$

$$- \int_{A_z} \rho v_z^{\,2}\, dA_z + \frac{1}{8\pi}\frac{r_0}{R}\beta \frac{dA_z}{ds}\left(\vec{I}\cdot\vec{B}_0\right)$$

$$+ R\frac{d\gamma}{ds}\int_{A_z} \rho v_z\,(v_y + v_{sy})\, dA_z\Big\}\frac{\vec{R}}{R^2}$$

$$+ \left\{\frac{1}{4\pi}\frac{dA_z}{ds}\left(\vec{I}\cdot\vec{B}_0\right)\left[1 + \frac{1}{2}\frac{r_0}{R}\alpha\right] - \frac{\mu_0}{8\pi} I^2 \frac{r_0}{R}\beta\right.$$

$$\left. + R\frac{d\gamma}{ds}\int_{A_z} \rho v_z\,(v_x + v_{sx})\, dA_z\right\}\frac{\vec{I}\times R}{IR^2} - \frac{r_0}{R}\alpha\left[\vec{I}\times\vec{B}_0\right] \qquad (39)$$

$$\vec{X}_{\parallel} = -\left\{\frac{\mu_0}{8\pi} I^2 \frac{1}{A_z}\frac{dA_z}{ds}\left[1 + \alpha^2 + \beta^2 + 2\frac{r_0}{R}\left(\alpha + \frac{3}{4}\frac{r_0}{R}\right)\right]\right.$$

$$- \frac{d}{ds}\left[\frac{1}{2\mu_0}\int_{A_z} \vec{B}_s^{\,2}\, dA_z\right] - \frac{1}{R}\int_{A_z} \rho v_z\,(v_x + v_{sx})\, dA_z \qquad (40)$$

$$\left. + \frac{1}{4\pi}\frac{dA_z}{ds}\left[\frac{\vec{B}_0\cdot\left[\vec{I}\times\vec{R}\right]}{R^2}\right]\left(1 + \frac{1}{2}\frac{r_0}{R}\alpha\right) + \frac{1}{2}\frac{r_0}{R}\beta\,\frac{I\left(\vec{B}_0\cdot\vec{R}\right)}{R^2}\right]\Big\}\frac{\vec{I}}{I}$$

where

$A_z = \pi r_0^{\,2}$ channel cross section

$\frac{dA_z}{ds} = 2\pi r_0 \frac{dr_0}{ds}$ channel divergence or convergence

$\int_{A_z} \ldots dA_z = \int_{\theta=0}^{2\pi}\int_{r=0}^{r_0} \ldots r\, dr\, d\theta$ summation over the cross sectional area

$\frac{d\gamma}{ds}$ = Twist; change of the twist angle along the channel axis

$$\left.\begin{matrix}\alpha \\ \beta\end{matrix}\right\} = \frac{1}{I}\int_0^{2\pi}\int_0^{r_0} j_z \frac{r}{r_0}\left\{\begin{matrix}\cos\theta \\ \sin\theta\end{matrix}\right\} r\, dr\, d\theta \qquad (41)$$

the first moments of the current density distribution across A_z with respect to the x- and y-axis, respectively

$\vec{I} = I\,\vec{u}_z$ current vector with $\vec{u}_z$ = unit vector in the z-direction

$\vec{B}_s$ the self magnetic induction due to the current through the channel segment

$\vec{B}_0$ magnetic induction due to the applied field

In this calculation one assumes that, inside the discharge channel and in its immediate vicinity, the time derivation of the channelbound impulse density can be neglected, or that flow and pressure field adjust in a relaxation-free manner to the $\vec{j} \times \vec{B}$ forces and vice versa. This assumption, however, is valid as long as the change of the channel diameter $d(2r_0)/dt$ or the motion of the discharge channel $|\vec{v}_s|$ is small compared to the average speed of sound within the considered channel segment, i.e.

$$\frac{d(2r_0)}{dt} \; ; \quad |\vec{v}_s| \ll \bar{a} \sim \sqrt{\frac{R}{\bar{M}}\,\bar{T}} \tag{42}$$

The validity of this inequality can be proven from case to case and, as discussed elsewhere,[2] is fulfilled for even extreme conditions. Since one distinguishes here only between stable and unstable channel configurations and does not consider the real change in time of an unstable channel, the validity of the above assumption or the inequality (42) cannot be questioned any longer.

Based on the knowledge of $\vec{X}$, one may now determine "balanced" and "stable" discharge channel configuration. A balanced channel is characterized by the fact that the transverse force $\vec{X}_\perp$ is zero along the channel axis. In addition, such a balanced configuration is also a stable one if for all possible small disturbances $\vec{\delta}$ off this configuration a force $\vec{X}_\perp$ acts on the channel in the opposite direction with respect to $\vec{\delta}$ and therefore tends to restore the original balanced state (see Fig. 24).

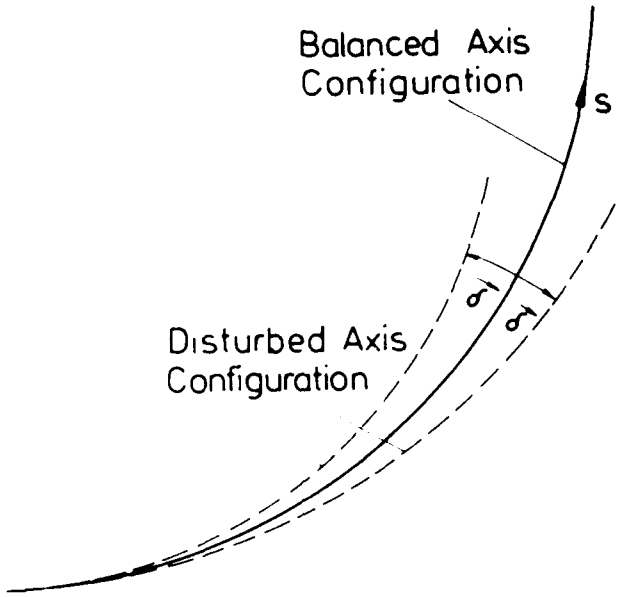

Fig. 24 Illustration of a disturbed axis configuration.

The requirement for a balanced axis configuration is therefore

$$\vec{X}_{\perp} = 0 \tag{43}$$

and for a balanced and stable configuration

$$\vec{X}_{\perp} \cdot \vec{\delta} < 0 \tag{44}$$

In the following sections this criteria will be applied a) to a nozzle-type MPD arc in order to investigate its stability behavior and b) to the spot conditions of the arc cathode attachment in order to better understand the electrode phenomena.

3.2 Onset Phenomenon Explained by a Flow Discharge Instability

It is a well known phenomenon in quasi-steady pulsed and in continuously run, coaxial MPD arc thrusters that by keeping the mass flow rate constant and increasing the current above a certain critical value, called "onset current", the arc becomes unstable. This phenomenon is characterized by a rapidly increasing terminal voltage, the appearance of high frequency oscillations of the terminal voltage on the order of 100 kHz and up to several 10 MHz and severe ablation of thruster components.

Many explanations have been offered and are briefly summarized by J. W. Barnett and R. G. Jahn.[3] Here a new explanation is presented which is based on the instability theory of section 3.1 and which shows that for a nozzle-type thruster above a certain current the rotational symmetry of the discharge channel is destroyed. In order to explain this, at first qualitatively, let us consider the current tube of an MPD arc jet as shown in Fig. 25 by the shaded area.

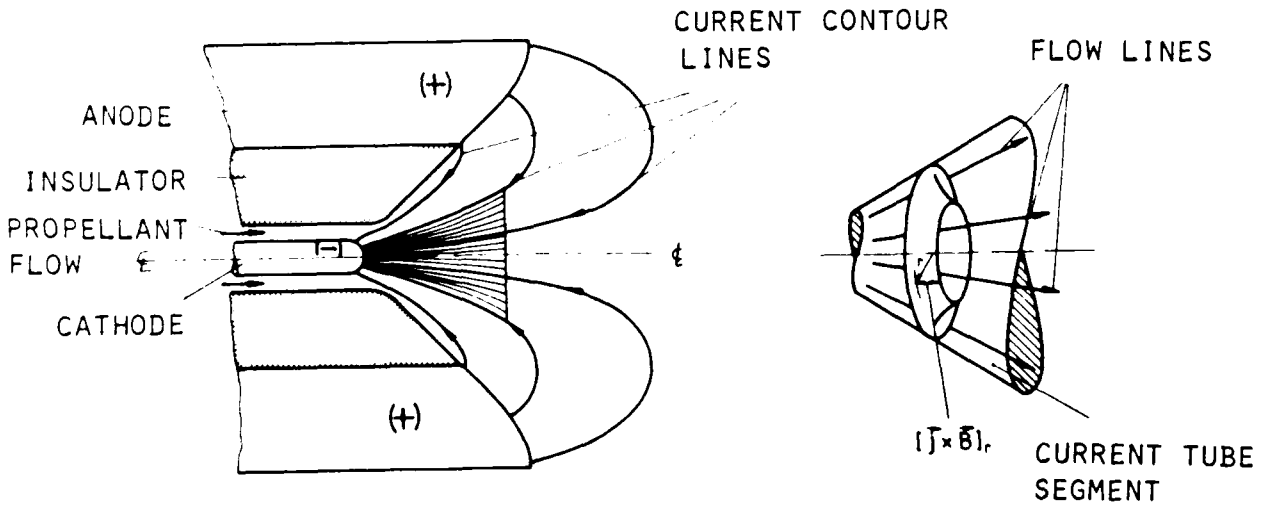

Fig. 25 Illustration of a coaxial current tube within an MPD arc.

---

[3] J. W. Barnett and R. G. Jahn, "Operation of the MPD Thruster with Stepped Current Input," Ph.D. Dissertation, Department of Mechanical and Aerospace Engineering Faculty of Princeton University, April 1985.

As mentioned before, in this undisturbed flow discharge configuration, the $\vec{j} \times \vec{B}$ forces have axial and radial components, both of which are rotationally symmetrical. If one plots the radial component on the cross section of a current channel, a volcano-like distribution is obtained. According to this force distribution, the plasma pressure towards the center of the discharge increases, which is known as pinch pressure. If, however, the current tube is somehow deflected or disturbed (see Fig. 26, shaded area; axis - displacement = $\vec{\delta}$) this radial $\vec{j} \times \vec{B}$ force component across the channel becomes asymmetrical.

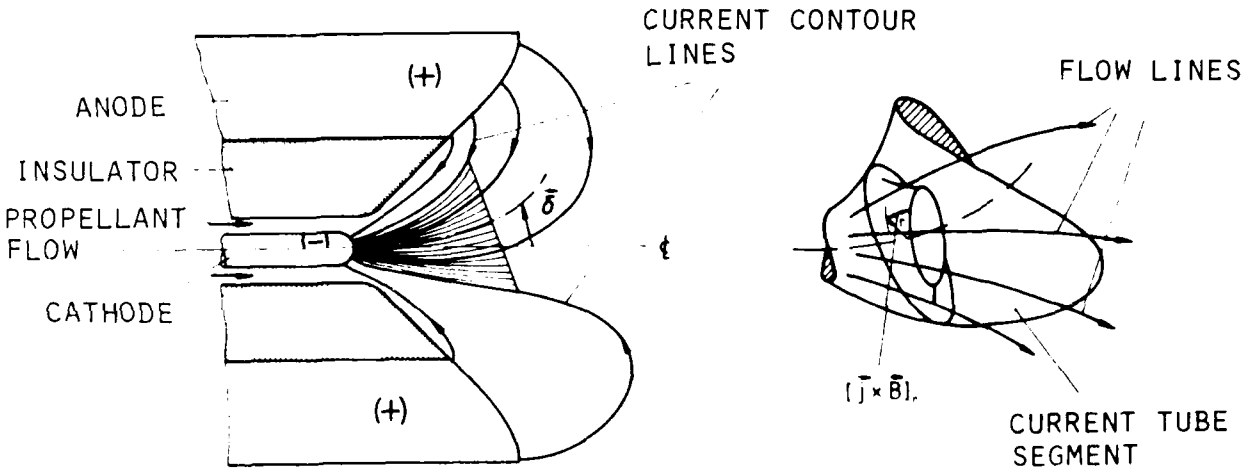

Fig. 26 Illustration of a disturbed current tube within an MPD Arc.

On the concave site of the channel, i.e. towards the center of curvature, the self magnetic field and hence the radial $[\vec{j} \times \vec{B}]_r$ forces increase. As a consequence of this asymmetry, the ohmically heated higher pressure plasma within the bent tube cannot be confined by the $[\vec{j} \times \vec{B}]_r$ force configuration and expands out on the weak magnetic field side of the discharge tube. The process within the considered current-carrying channel may be somehow compared with the propulsion effect of a rocket in which the combustible, heated gas is confined under higher pressure within a chamber and

expands out through an opening or a nozzle throat. Now, however, instead of solid walls, we are dealing with magnetic forces and an ohmically heated gas which should, however, create the same gas-dynamic propulsion effect transverse to the current-carrying plasma tube. A typical banana or horseshoe-like plot of lines of constant radial $[\vec{j} \times \vec{B}]_r$ forces across a cross sectional area of the bent tube is shown in Fig. 27 and indicates a similarity to the wall configuration of a rocket engine.

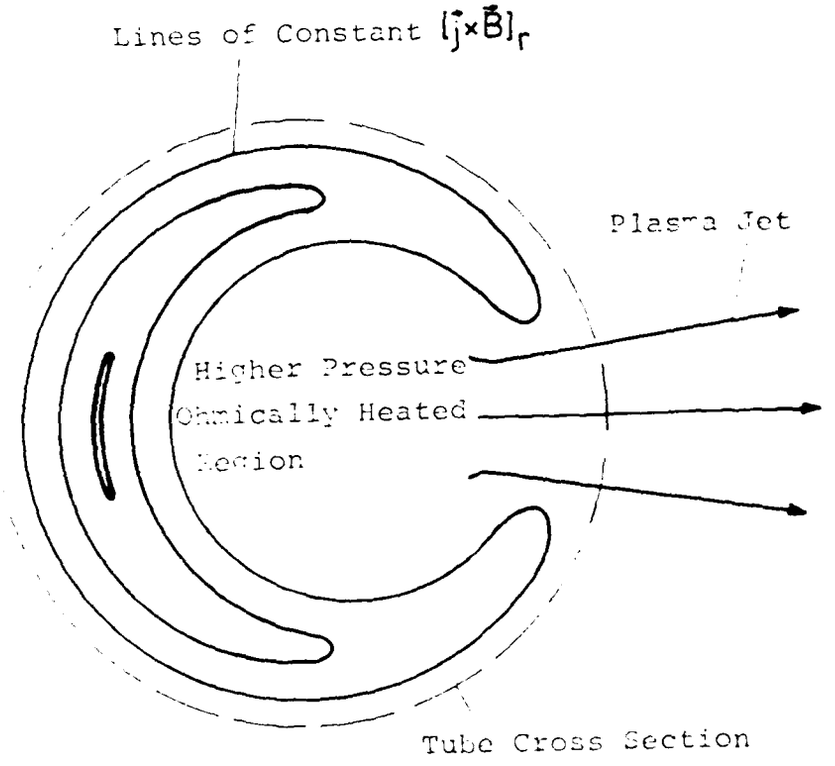

Fig. 27 Lines of constant radial $[\vec{j} \times \vec{B}]_r$ forces with transverse plasma jet.

According to this electromagnetically induced expansion flow, a propulsion effect is impressed on such a current tube, or more precisely, a resultant gas-dynamic force acts on the control volume of a tube segment (see Fig. 28). It is

$$\vec{S} = \int_{A_M} \Delta\vec{F}\ \Delta s + \vec{K}(s+\Delta s) + \vec{K}(s) \qquad (45)$$

where the first term on the right represents the sum over the surface forces around the mantel and the two others are the forces which act on both cross sectional endplanes.

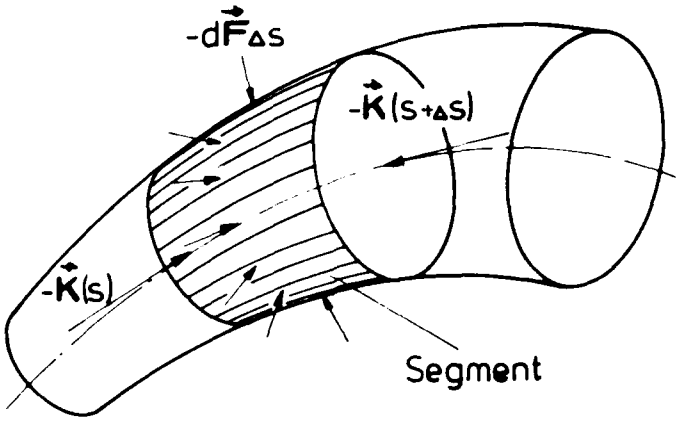

Fig. 28 Illustration of the gas-dynamic surface forces which act on a tube segment of length Δs.

It can be shown that under certain conditions this resultant gas-dynamic force becomes predominant and therefore bends the current tube more and more. As a consequence of this bending, the rotational symmetry of the discharge will be destroyed, and the nozzle wall and/or anode ring on one side will be locally overheated, which leads eventually to an anode spot and to serious damage to the thruster. Now the sum of all forces per unit axis length given by the surface forces, volume or field forces and the fictitious forces like centrifugal and Coriolis forces acting transversely on a current tube is given by $\vec{X}_\perp$ according to eq. (39). Inasmuch as one allows only a bent and not a twisted disturbance, the force $\vec{X}_\perp$ reduces in a first order approximation of r_0/R (channel radius divided by axis curvature) to the following expression

$$\vec{X}_\perp = \left\{\frac{1}{2\mu_0} \int_{A_z} \vec{B}_s^{\,2}\, dA_z + \frac{\mu_0}{8\pi} I^2 - \int_{A_z} \rho v_z^{\,2}\, dA_z\right\} \frac{\vec{R}}{R^2} \qquad (46)$$

The requirement eq. (43) for a balanced channel configuration is therefore fulfilled for a straight discharge tube ($R \to \infty$) as shown in Fig. 25. Moreover, since any disturbance $\vec{\delta}$ (see Fig. 26) points in the direction of $\vec{R}$, the stability requirement follows by

$$\frac{1}{2\mu_0} \int_{A_z} \vec{B}_s^{\,2}\, dA_z + \frac{\mu_0}{8\pi} I^2 - \int_{A_z} \rho v_z^{\,2}\, dA_z \quad \begin{matrix} < \\ = \\ > \end{matrix} \quad \begin{matrix} \text{stable} \\ \text{indifferent} \\ \text{not stable} \end{matrix} \qquad (47)$$

It has been shown[4] that instability should occur at first in a current tube somewhat downstream of the nozzle throat. This instability, however, affects then only a part of the entire discharge. Now the entire arc becomes unstable if the conditions within the nozzle throat are such that the appertaining quantities, as shown on the left side of eq. (47), become larger than zero.

One can now model the current density within the nozzle throat in different ways and obtain for the integral with the square of the self-magnetic induction field $\vec{B}_s$ the expression

$$\frac{1}{2\mu_0} \int_{A_z} \vec{B}_s^{\,2}\, dA_z = \frac{\mu_0}{8\pi} I^2 f \qquad (48)$$

where f is a number of the order 1, which depends on the current density distribution. By taking a paraboloid of grade n, it is

$$f = f(n) = \frac{1}{2n^2} \left\{ (n+2)^2 - 16 \frac{n+2}{n+4} + \frac{8}{n+2} \right\} \qquad (49)$$

---

[4] H. O. Schrade, M. Auweter-Kurtz, and H. L. Kurtz, "Stability Problems in Magneto Plasmadynamic Arc Thrusters," AIAA-85-1633, 18th Fluid Dynamics and Plasmadynamics and Lasers Conference, July 1985.

For a Gaussian distribution with a cutoff radius of r_0 and a half width of r_c, one obtains

$$f = f\left(\frac{r_0}{r_c}\right) = \frac{1}{\left[1 - e^{-\left(\frac{r}{r_c}\right)^2}\right]^2} \int_0^{r_0} \frac{\left[1 - e^{-\left(\frac{r}{r_c}\right)^2}\right]^2}{\left(\frac{r}{r_c}\right)^2} \, d\left(\frac{r}{r_c}\right) \qquad (50)$$

The axial impulse flux in eq. (47) can now be related to the total mass flow rate and the average speed of sound within the nozzle throat. It is

$$\int_{A_z} \rho v_z^2 \, dA_z = \dot{m} \, \bar{a}_t = \dot{m} \sqrt{2 \frac{R_0}{M} \bar{T}_t} \qquad (51)$$

According to Appendix II eq. (II.24), the average temperature $\bar{T}_t$ is now a function of the current and the nozzle throat radius r_t; here one assumes a current density distribution of the shape of a paraboloid. A similar relation can be obtained if one takes a Gaussian distribution. In that case, it is

$$\bar{T}_t = \left(\frac{7}{8\pi^2} \frac{1}{\alpha\gamma}\right)^{1/5} \left(\frac{I}{r_t}\right)^{2/5} \psi\left(\frac{r_0}{r_c}\right) \qquad (52)$$

where $\psi(r_0/r_c)$ is now a function of the quotient cuttoff radius r_0 divided by the half width r_c.

One now replaces in eq. (47) the two integral expressions according to eqs. (48) and (51) and sets for $\bar{T}_t$ either the relation (II.24) or (52); after some transformation one obtains the requirement for a stable or unstable arc in the form

$$\frac{I^{9/5} M^{1/2} r_t^{1/5}}{\dot{m}} \begin{matrix} < \\ = \\ > \end{matrix} 4.15 \cdot 10^{10} \cdot \phi \qquad \begin{matrix} \text{stable} \\ \text{indifferent} \\ \text{not stable} \end{matrix} \qquad (53)$$

where now ϕ is a function either of n or of r_0/r_c, depending on which modelling of the current density distribution, paraboloid, or Gaussian one takes. It is

$$\phi = \frac{\sqrt{\psi}}{1+f} \tag{54}$$

In criteria (53), the arc current I is measured in [A], the mass flow rate $\dot{m}$ is measured in [kg/s], M is the molecular weight (e.g. argon: $M_A = 40$) and r_t is the radius of the nozzle throat in [m].

In Figs. 29 and 30 the critical current is now plotted as a function of the mass flow rate according to eq. (53) for the Stuttgart nozzle-type thruster (see Fig. 2) with $r_0 = 0.012$ and $\dot{m} = 0.8$ g/s argon as propellant mass flow rate, taking n and (r_0/r_c) as parameter, respectively. The curves with $n = 1/2$ and $r_0/r_c = 2$ show excellent agreement with experimental onset values; both correspond to the value $\phi = \phi(n) \approx \phi(r_0/r_c) \approx 0.31$. In the 1 g/s and 1.5 g/s mass flow rate tests, the onset conditions were not reached even at 5000 A and 6000 A, respectively.

Based on this analysis, the onset phenomena are explained by an MPD instability within the flow discharge region.

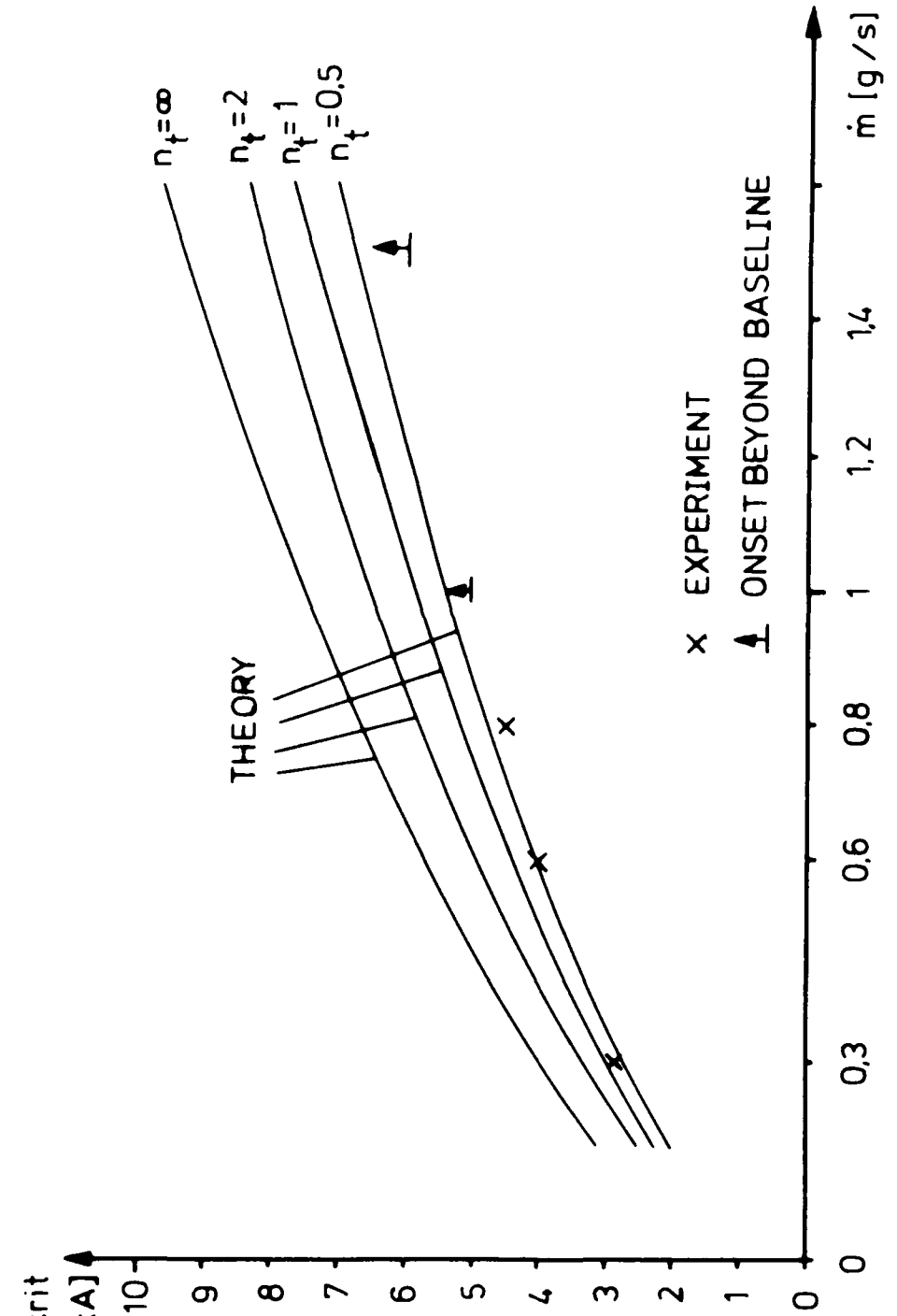

Fig. 29 Comparison between theoretical and experimental onset current as a function of the mass flow rate for the Stuttgart nozzle-type thruster. Current density modelled by a parabola of grade n.

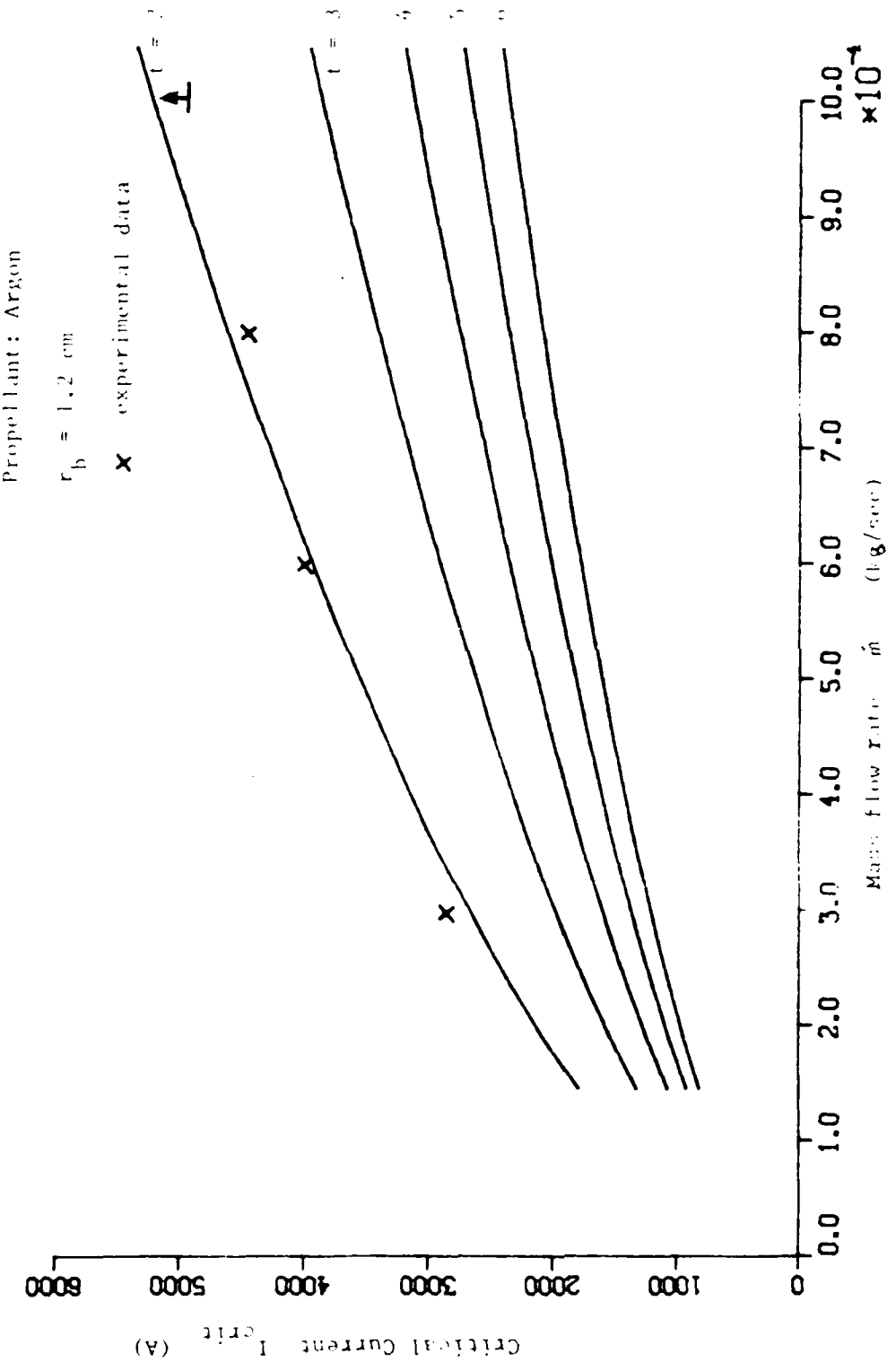

Fig. 30 Comparison between theoretical and experimental onset current as a function of the mass flow rate for the Stuttgart nozzle-type thruster. Current density modelled by a cutoff Gaussian distribution

$t = r_0/r_C$ = cutoff radius/halfwidth.

3.3 Instability of a Cathode Spot

It is a known phenomenon that in a pulsed MPD thruster[5,6,7] and during the starting phase in a continuous MPD thruster[8,9] the arc cathode attachment consists of many hot spots of high current density. These spots are usually highly non-stationary and jump statistically across the cathode surface.[10] In the presence of an applied magnetic field parallel to the cathode surface these spots jump preferably in the retrograde direction, i.e. opposite to the Lorentzian force direction.[11] If the magnetic field lines are inclined with respect to the cathode surface, one observes a drifting of the arc foot points or spots away from the retrograde direction. This drift motion was experimentally investigated by Robson[12] and therefore is named after him. This seemingly

---

[5] T. Yoshikawa, Y. Kagaya, K. Kuriki, "Thrust and Efficiency of New K-III MPD Thruster," AIAA 82-1887, 16th IEPC, New Orleans, 1982.

[6] K. E. Clark and R. G. Jahn, "Magnetoplasmadynamic Thruster Erosion Studies, Phase I," Interim Report, AF Contract R 04611-79-C-0039, April 1983.

[7] K. Kuriki et al., "MPD Arc Jet System Performance Test," IAF 83-392, 34th IAF Congress, Budapest, Hungary, 1983.

[8] H. Hügel and G. Krülle, "Phänomenologie und Energiebilanz von Lichtbogenkathoden bei niedrigen Drücken und hohen Stromstärken," Beiträge Plasmaphysik, Vol. 9, p. 87, 1969.

[9] H. O. Schrade, M. Auweter-Kurtz, and H. L. Kurtz, "Plasma Thruster Development," IRA Report 85 P3, Institut für Raumfahrtantriebe, Universität Stuttgart, April 1985.

[10] A. E. Guile and B. Jüttner, "Basic Erosion Processes of Oxided and Clean Metal Cathodes of Electric Arcs," IEEE Transactions on Plasma Science, Vol. P.S.8, p. 259, 1980.

[11] L. P. Harris, "Arc Cathode Phenomena," Contr. in "Vacuum Arcs, Theory and Applications," J.M. Lafferty, ed., John Wiley & Sons, New York, 1980.

[12] A. E. Robson, "The Motion of a Low Pressure Arc in a Strong Magnetic Field," J. Physics D. Applied Physics, Vol. II, p. 1917, 1978.

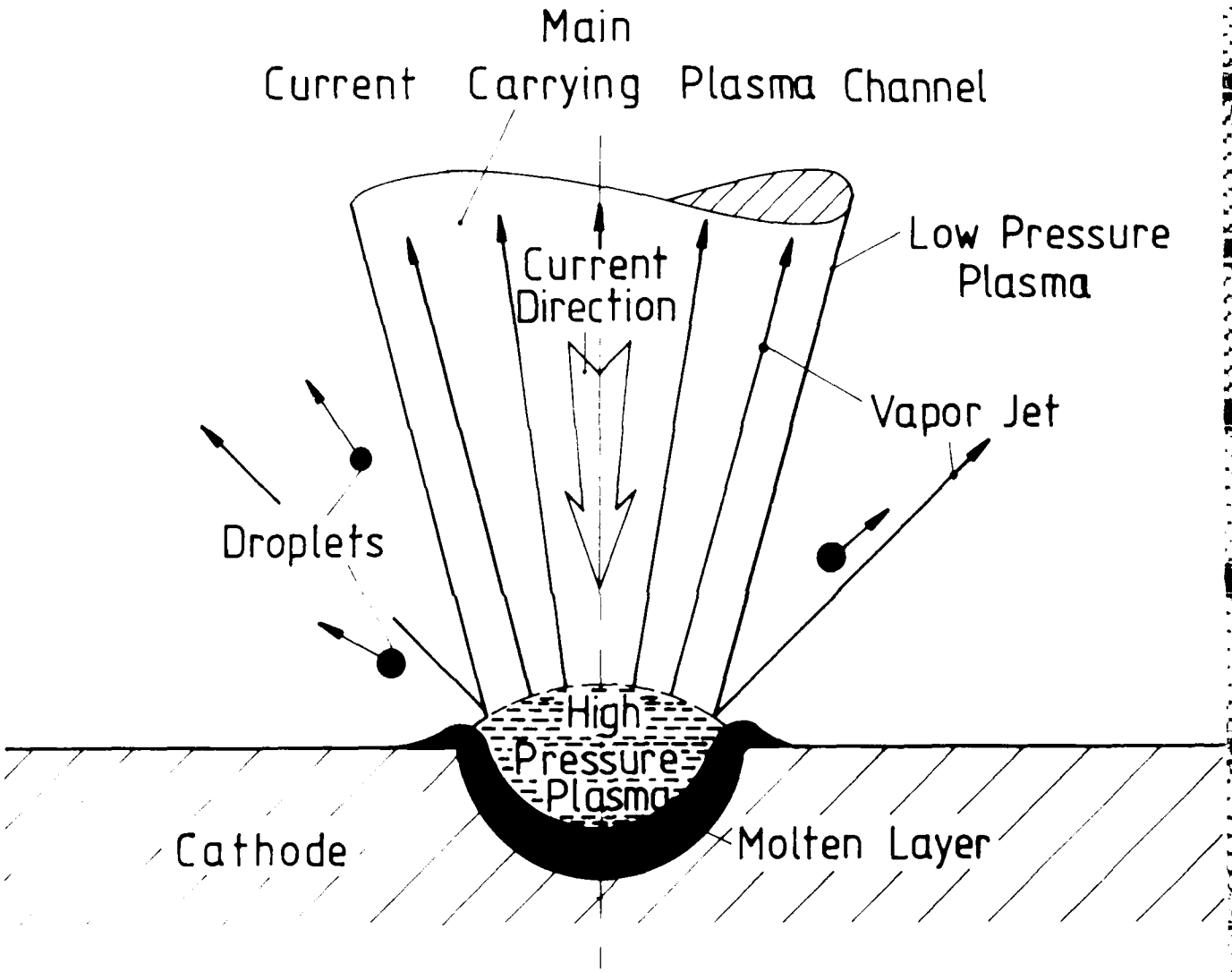

Fig. 31 : Schema of a Spot Discharge with a Straight Discharge Channel

strange spot behavior can be explained by a similar MPD instability shown for the arc jet in the preceeding section. Now the vapor and plasma jet which proceeds from a superheated cathode spot has microscopic dimensions (of the order of microns); the jet is electrically conductive and thus contains a current-carrying channel (see Fig. 31) which electrically connects the cathode spot and thus the cathode with the plasma of the interelectrode gap and thereby with the anode. To the current-carrying channel of such a spot one can now apply the same balance and stability requirements eqs. (43) and (44) together with eq. (39) as done before. First of all, in order to account for not rotationally symmetric current density distributions within the discharge channel, one models this distribution by any "eccentric paraboloid of grade n". Such a distribution follows from a concentric parabola through shifting the maximum to a point of the channel cross section with the coordinates (r_M, θ_M) as shown in Fig. 32. Based on this modelling one obtains[2]

$$\frac{1}{2\mu_0} \int_{A_z(s)} \vec{B}_s^{\,2}\, dA_z = \frac{\mu_0}{8\pi} I^2 f(n) \left\{1 + g(n) \frac{r_M}{R} \cos\theta_M\right\} \qquad (55)$$

and

$$\begin{Bmatrix}\alpha \\ \beta\end{Bmatrix} = \frac{1}{I} \int_0^{2\pi} \int_0^{r_0} j \frac{r}{r_0} \begin{Bmatrix}\cos\theta \\ \sin\theta\end{Bmatrix} r\, dr\, d\theta = \frac{1}{n+3} \frac{r_M}{r_0} \begin{Bmatrix}\cos\theta_M \\ \sin\theta_M\end{Bmatrix} \qquad (56)$$

where f(n) according to eq. (49) and g(n) are plotted in Fig. 33. The transverse force $\vec{X}_\perp$ per unit channel length follows now in third order approximation of r_0/R from eq. (39) by

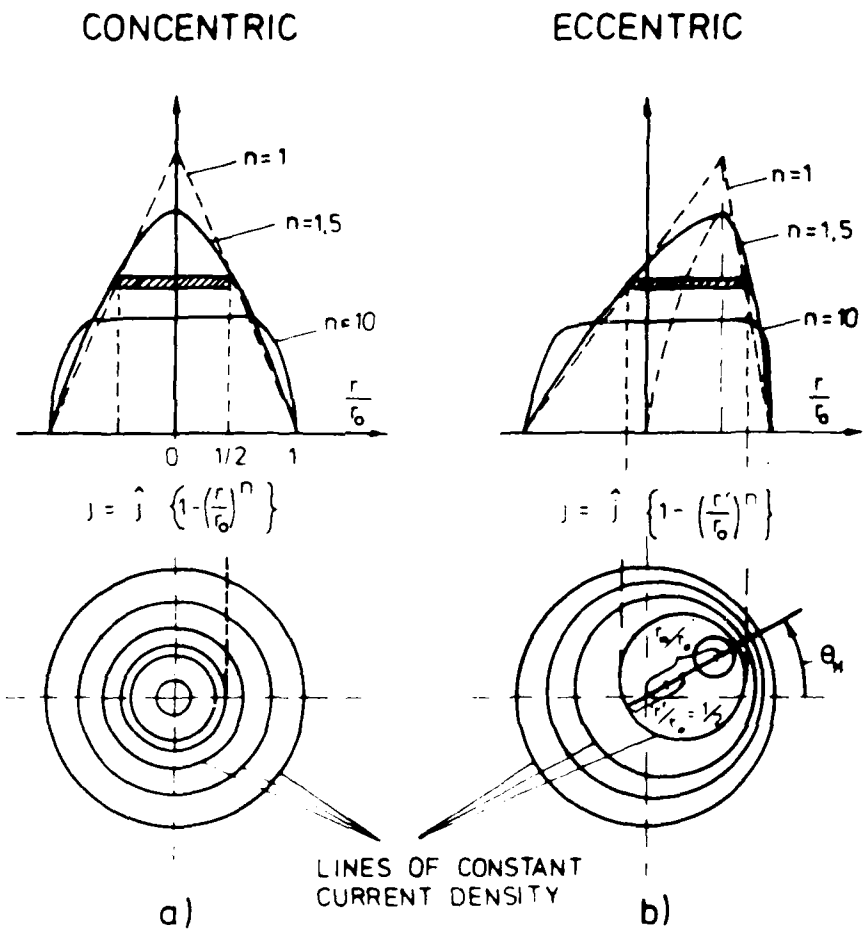

Fig. 32 Current distribution modelled by a) a concentric and b) an eccentric paraboloid of grade n.

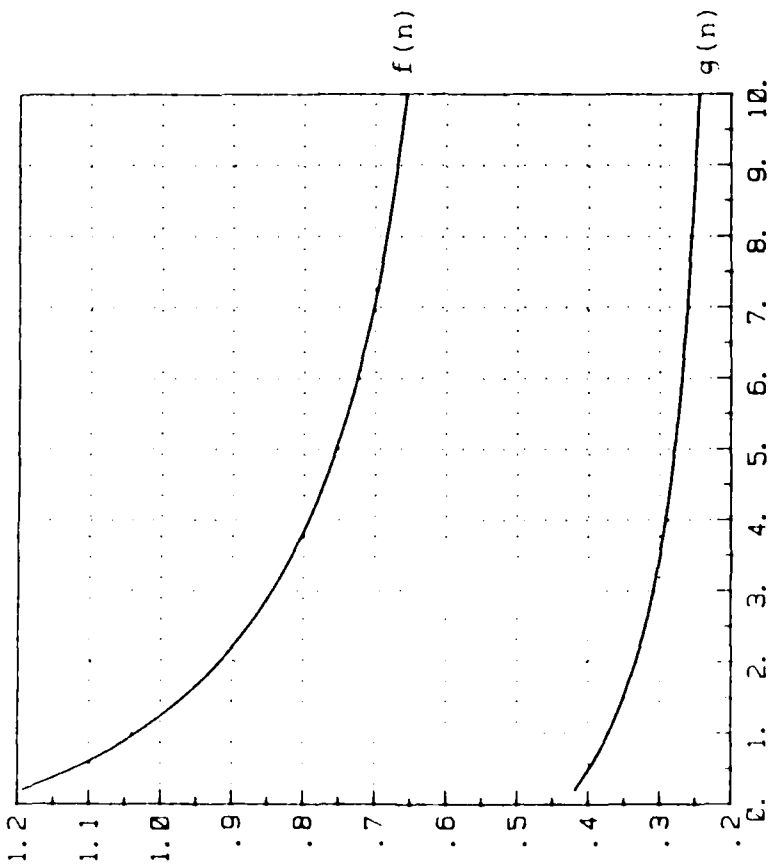

Fig. 33: Plot of the functions f(n) and g(n)

$$\vec{X}_{\perp} = \{\frac{\mu_0}{8\pi} I^2 \left[1 + f(n) + \frac{r_0}{R}\left(f(n)g(n)(n+3) + 1\right)\alpha + \frac{3}{4}\left(\frac{r_0}{R}\right)^2\right]$$

$$+ \frac{1}{8\pi}\frac{r_0}{R}\beta\frac{dA_z}{ds}(\vec{I}\cdot\vec{B}_0) - \int_{A_z}\rho v_z^2\, dA_z$$

$$+ R\frac{d\gamma}{ds}\int_{A_z}\rho\, v_z(v_y + v_{sy})\, dA_z\}\frac{\vec{R}}{R^2}$$

$$+ \{\frac{1}{4\pi}\frac{dA_z}{ds}(\vec{I}\cdot\vec{B})\left[1 + \frac{1}{2}\frac{r_0}{R}\alpha\right] - \frac{8\pi}{\mu_0}I^2\frac{r_0}{R}\beta$$

$$+ R\frac{d\gamma}{ds}\int_{A_z}\rho\, v_z\,(v_x + v_{sx})\, dA_z\}\frac{\vec{I}\times\vec{R}}{IR^2} - \frac{r_0}{R}\alpha\,\vec{I}\times\vec{B}_0 \qquad (57)$$

If one now introduces the inclination angle ξ and the disturbance angle ϕ according to Fig. 36 for such a current channel segment emanating from a fixed cathode spot crater, one can write the transverse force per unit axis length by

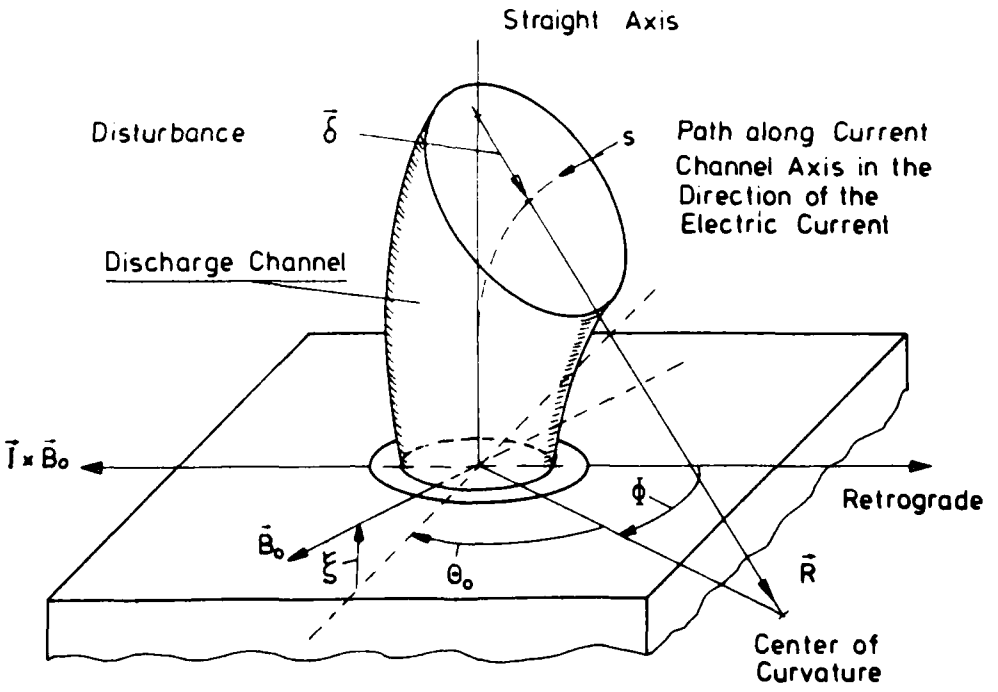

Fig. 34 Illustration of a disturbed current-carrying channel at the cathode surface with inclined magnetic field.

$$\vec{X}_{\perp} = -\frac{\mu_0}{8\pi}\frac{I^2}{R}\left\{\varepsilon - \frac{\alpha}{\lambda}\cos\xi\cos\phi - \frac{r_0}{R}\left[\alpha k + \frac{3}{4}\frac{r_0}{R} - \frac{1}{4}\frac{dr_0}{ds}\frac{\beta}{\lambda}\sin\xi\right]\right\}\frac{\vec{R}}{R} - \frac{\mu_0}{8\pi}\frac{I^2}{R}\left\{\frac{1}{2}\frac{dr_0}{ds}\frac{1}{\lambda}\sin\xi + \frac{\alpha}{\lambda}\cos\xi\sin\phi + \frac{r_0}{R}\left[\beta + \frac{1}{4}\frac{dr_0}{ds}\frac{\alpha}{\lambda}\sin\xi\right]\right\}\frac{\vec{I}\times\vec{R}}{\vec{I}\cdot\vec{R}} \tag{58}$$

where now

$$\varepsilon = \frac{8\pi}{\mu_0}\frac{1}{I^2}\left\{\int_{A_z}\rho\, v_z^2\, dA_z - \frac{\mu_0}{8\pi}I^2\left[1 + f(n)\right]\right\} \tag{59}$$

$$k = k(n) = (n+3)f(n)g(n) + 1 \tag{60}$$

$$\lambda = \frac{\mu_0}{8\pi}\cdot\frac{I}{r_0 B_0} = \frac{\text{average self magnetic induction field}}{\text{applied magnetic induction field}} \tag{61}$$

Herein one assumes that any disturbance $\vec{\delta}$ leads only to a bent (see Fig. 34) but not to a twisted current-carrying channel. According to eqs. (57) and (58), a straight channel (with $R \to \infty$) is again a balanced one, since $\vec{X}_{\perp} = 0$. The direction of any disturbance $\vec{\delta}$ points now in the $\vec{R}$ direction; therefore, a balanced, straight channel is also stable if the braced expression of the $\vec{R}/R$ component of $\vec{X}_{\perp}$ is larger than zero. Neglecting the higher order terms of r_0/R, one therefore obtains as stability requirement

$$\varepsilon - \frac{\alpha}{\lambda}\cos\xi\cos\phi > 0 \tag{62}$$

One may now distinguish between the following three cases

1. No applied magnetic field, $|\vec{B}_0| \sim \frac{1}{\lambda} = 0$.

2. $\vec{B}_0$ parallel to the cathode surface, $\xi = 0$.

3. $\vec{B}^0$ inclined with respect to the cathode surface, $\xi \neq 0$.

Case 1: $|B_0| \sim \frac{1}{\lambda} = 0$

In this case the stability requirement reduces to

$$\varepsilon > 0 \qquad \text{(stable)} \tag{63}$$

which is identical with that of the MPD arc in section 3.2. Here the stability criterion does not depend on the direction of the disturbance given by ϕ (see Fig. 34). Within eq. (59) one may now relate the average impulse transport

$$\int_{A_z} \rho v_z^2 \, dA_z$$

along the channel axis with the vapor and plasma pressure p_v of the spot crater[13] and the ambient pressure p_∞. Therefore, the stability requirement (63) can also be expressed in the form

$$p_v - p_\infty > 3.3 \frac{\mu_0}{8\pi} I_s \bar{j}_s \tag{64}$$

where I_s is the current carried by the spot and $\bar{j}_s$ is the average current density within the spot; the factor 3.3 is valid for a hemispherical crater and changes to about 3.0 for a flat crater.

The pressure difference between the vapor pressure in the spot and the ambient pressure must be therefore more than about three times larger than the average magnetic pressure ($p_M = \mu_0/8\pi \, I_s \bar{j}_s$) in order to maintain a straight, stable spot discharge. If this requirement is no longer fulfilled or if $\varepsilon < 0$, the channel becomes unstable. Any small disturbance will cause the channel to bend more and more, and eventually it will contact the cathode surface at a nearby site off the original spot (see Fig. 35). The new site is heated up and a new spot is created. Again, for this new spot, the stability requirement (63) or (64) must be fulfilled in order to maintain a balanced, stable spot. Since

---

[13] H. O. Schrade, M. Auweter-Kurtz, and H. L. Kurtz, "Analysis of the Cathode Spot of Metal Vapor Arcs," IEEE Transactions on Plasma Science, Vol. PS-11, No. 3, p. 103, 1983.

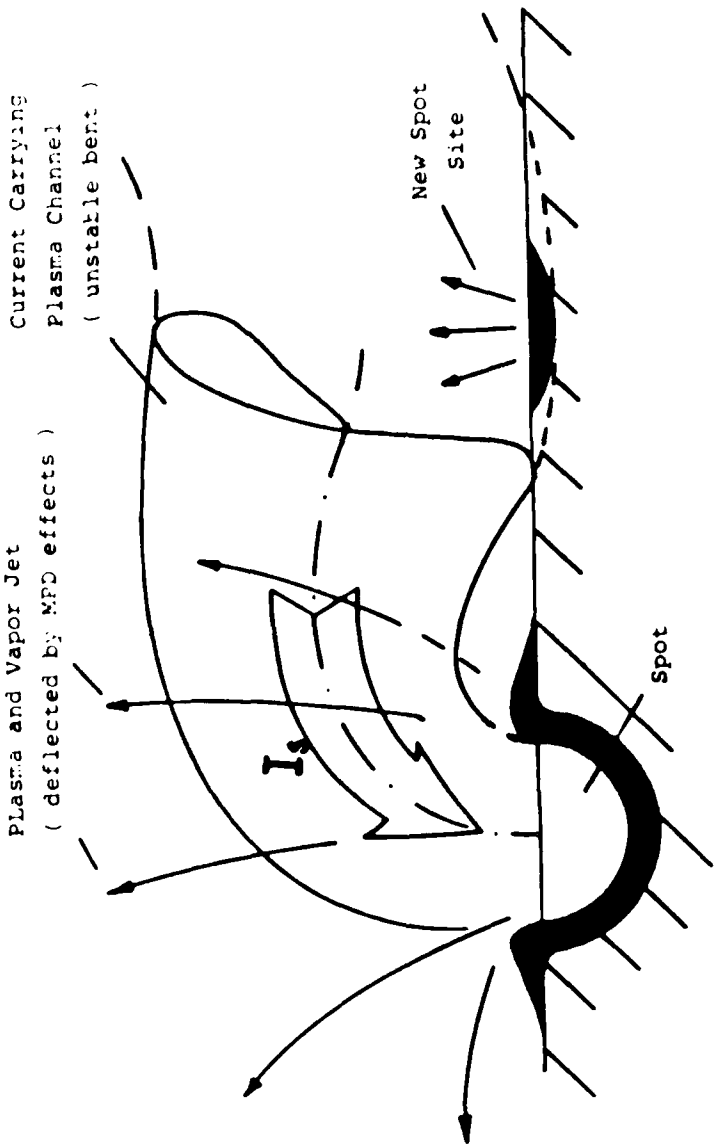

Fig. 35 Spot propagation due to bending of the current channel.

in this case the stability criterion does not depend on the direction of the disturbance, and since one may assume that all possible directions of $\vec{\delta}$ are equally probable, the spots should move or jump statistically over the cathode surface.

Case 2: $\vec{B}_0$ parallel to the cathode surface, $\xi = 0$.

In this case, the stability criterion follows by

$$\varepsilon - \frac{\alpha}{\lambda} \cos\phi > 0 \tag{65}$$

i.e. the channel stability depends now on the direction of the disturbance (ϕ). Moreover, the force component in the $\vec{I}x\vec{R}$ direction of eq. (58) becomes unequal to zero in the first order. It is

$$\vec{X}_{\perp \text{ (in } \vec{I}x\vec{R})} = - \frac{\mu_0}{8\pi} \frac{I^2}{R} \frac{\alpha}{\lambda} \sin\phi \frac{\vec{I}x\vec{R}}{I \cdot R} \tag{66}$$

For $\alpha > 0$, i.e. the current density maximum is shifted towards the center of curvature, the channel is less likely to be stable for any disturbance towards the retrograde side $-\pi/2 < \phi < +\pi/2$ than for a disturbance towards the amperian side $\pi/2 < \phi < 3\pi/2$ (or $-\pi/2 > \phi > -3\pi/2$) which can be verified by means of criterium (65). For any disturbed or curved channel, there acts now a force in the $\vec{I} \times \vec{R}$ direction [eq. (66)] such that the curved channel always turns into the retrograde direction, i.e. $\vec{\delta}$ points finally in the opposite $\vec{I}x\vec{B}_0$ direction. The channel therefore becomes preferably unstable by bending more and more in the retrograde direction.

For $\alpha < 0$, the current density maximum is shifted away from the center of curvature maximum towards the convex side of the channel. According to criteria (65) and eq. (66), the channel should now bend preferably in the amperian direction. One can, however, show that by accounting for the higher order term $(r_0/R)\alpha k$ in eq. (58), the channel this time assumes a curved, stable configuration. The possible

consequence of this is that the channel does not come in contact with the cathode surface on the amperian side of the spot. This is not the case for a retrograde disturbance with $\alpha > 0$, for which the channel is unstable and bends more and more. Observable current channels should therefore be amperically bent or straight while the observation of a retrograde channel configuration would require high time resolutions.

In conclusion to Case 2, a spot prefers to jump or move either in the retrograde or the amperian direction, depending on whether the current density maximum is shifted towards the concave or the convex side of the discharge channel. Because of the unstable channel behavior during the retrograde motion and the stable, bent channel behavior during the amperian motion, one may conclude that the average jump distance is smaller and the number of jumps more frequent for the retrograde moving spots than for the amperian moving ones. For large magnetic fields ($\lambda k \ll 1$, which means about $\vec{B}_0 \gg 1$ Tesla for an experimental value[14] of $I/r_0 \approx 10^7$ A/m) the mechanisms for amperian and retrograde spot motion are practically identical and therefore in both directions equally probable.

Case 3: $\vec{B}_0$ inclined with respect to the cathode surface, $\xi \neq 0$.

According to eq. (62) the current channel is preferably unstable with respect to a disturbance in the retrograde direction and assumes a bent but stable configuration for an amperian disturbance. The principle difference now is given through the force component in the $\vec{I} \times \vec{R}$ direction, which in the first order of r_0/R follows by

---

[14] J. P. Datlov, A. E. Guile, and B. Jüttner, "Unipolar Arc Tracks on Stainless Steel," Beiträge aus Plasmaphysik, Vol. 21, p. 135, 1980.

$$\vec{X}_{\perp\,(\text{in } \vec{I}\times\vec{R})} = -\frac{\mu_0}{8\pi}\frac{I^2}{R}\left\{\frac{1}{2}\frac{dr_0}{ds}\frac{1}{\lambda}\sin\xi + \frac{\alpha}{\lambda}\cos\xi\,\sin\phi\right\}\frac{\vec{I}\times\vec{R}}{I\cdot R} \quad (67)$$

and which turns the disturbed or curved channel around its original straight axis either in the retrograde ($\alpha > 0$) or amperian direction ($\alpha < 0$). Now, however, the disturbance $\vec{\delta}$ finally does not point exactly in these directions but deviates or drifts away from them. The drift angle follows from the requirement that for this position the turning force in the $\vec{I} \times \vec{R}$ direction must be zero. From eq. (67) follows therefore

$$\sin\Phi_{drift} = -\frac{1}{2\alpha}\frac{dr_0}{ds}\tan\xi \quad (68)$$

For a spot motion towards the retrograde side it is $\alpha > 0$, and since the channel in the direction of the current is supposed to converge ($dr_0/ds < 0$), the drift angle ϕ_{drift} is proportional to ξ as long as the angles are small. The retrograde moving spots drift, therefore, under a small angle with respect to the proper retrograde direction towards the right (in the direction of B_0) if the B_0 field points upward and drifts towards the left (opposite to B_0) if the field vector points downward (see Fig. 36a,b). This spot behavior has been experimentally observed and is known as Robson drift motion.[15],[16]

---

[15] A. E. Robson, "The Motion of an Arc in a Magnetic Field," Procedures, 4th International Conference on Phenomena in Ionized Gases IIB, 346, Aug. 1959.

[16] W. Hintze and M. Laux, "On the Motion of Unipolar Arcs in a Tokamak," Beiträge Plamaphysik, Vol. 21, p. 247, 1981.

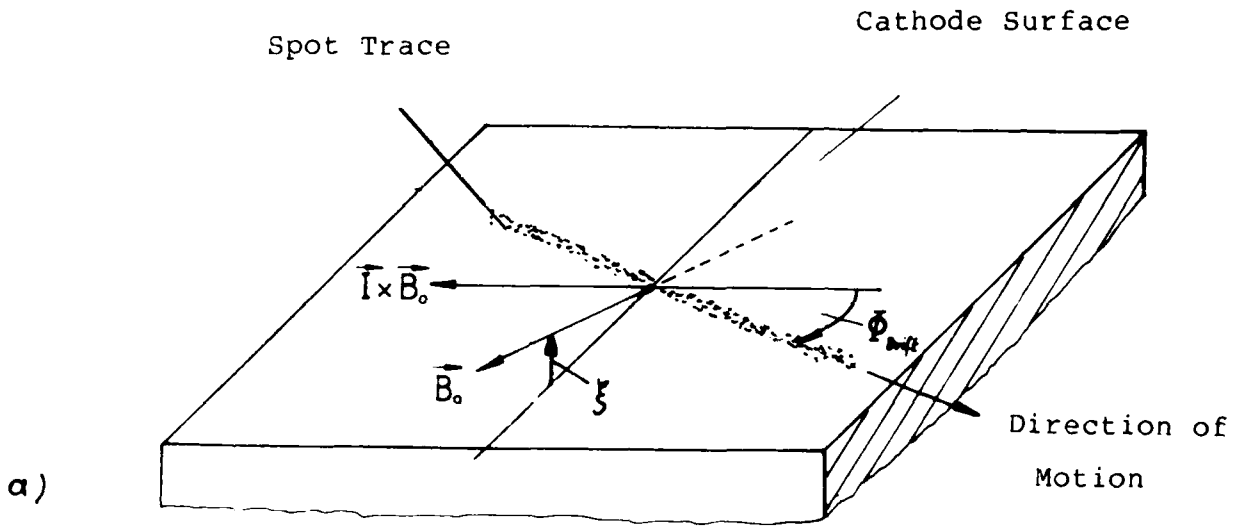

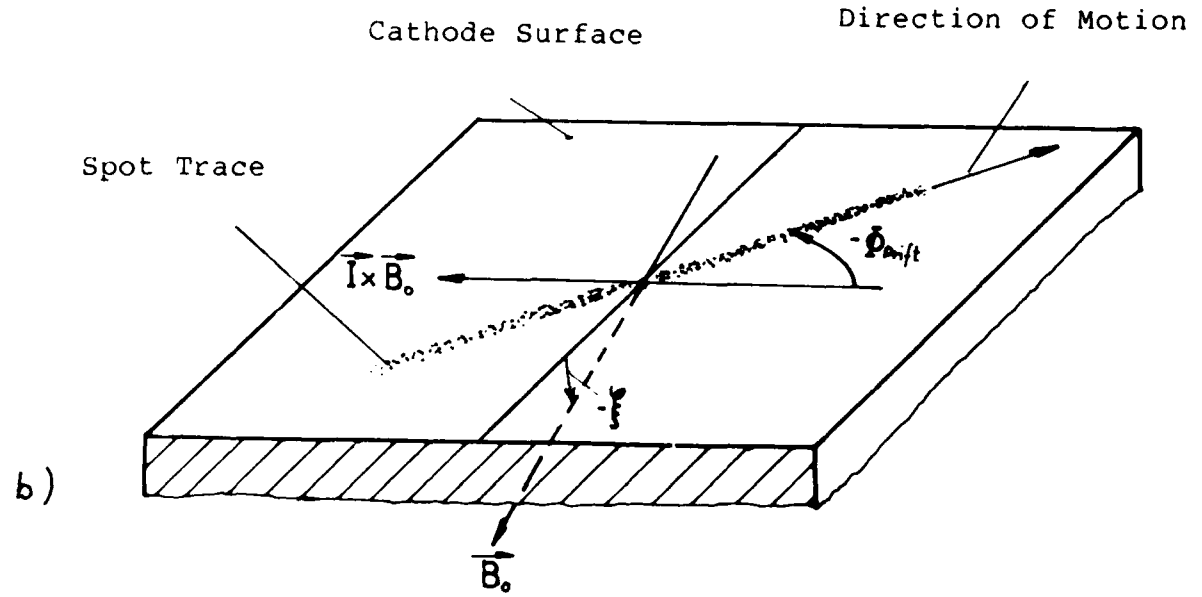

Fig. 36 Retrograde spot motion with an inclined $\vec{B}_0$ field.

4. Electrode Investigations

4.1 Theory

Spot Initiation: If a plasma contacts the metallic surface of a cathode, a space charge layer with a thickness of several Debye length is built up. The metallic surface becomes electro-negatively charged, while in the plasma layer the positive charges predominate. The initiation of a breakdown across this layer may now be explained as follows: the electric field at the tip of a protrusion (see Fig. 37a) at any dust particle on the electrode surface becomes high enough, so that by field or thermal field emission[17] the current density at this tip or surface impurity increases to such an extreme value that a local overheating and an explosive evaporation of cathode material takes place. Such a condition requires, for instance for copper cathodes, current densities of the order of 10^{12} A/m^2 and more[18] in order to overpower conduction cooling within the solid metal by electric heating.

As a consequence of these high current densities, one must expect a strong ionization of the evaporated cathode material and hence also an increase of plasma pressure in front of or around the initial breakdown point. Since this increased plasma pressure also means a higher electron density, the Debye length within the high density plasma decreases and therefore also the thickness of the plasma layer in front of the initial emission point. Due to this effect, the voltage drop across the entire plasma layer causes a higher electric field at the area where a higher density plasma is present than somewhere else where the density is lower (see Fig. 37b). The higher electric field, however, leads to a higher

---

[17] G. Ecker, "Electrode Components of the Arc Discharge," in Erg. exakt. Naturwiss., Vol. 33, p.1, 1961.

[18] G. Ecker, "Theoretical Aspects of the Vacuum Arc," in "Vacuum Arcs, Theory and Application," ed. by J.M. Lafferty, John Wiley & Sons, New York, 1980.

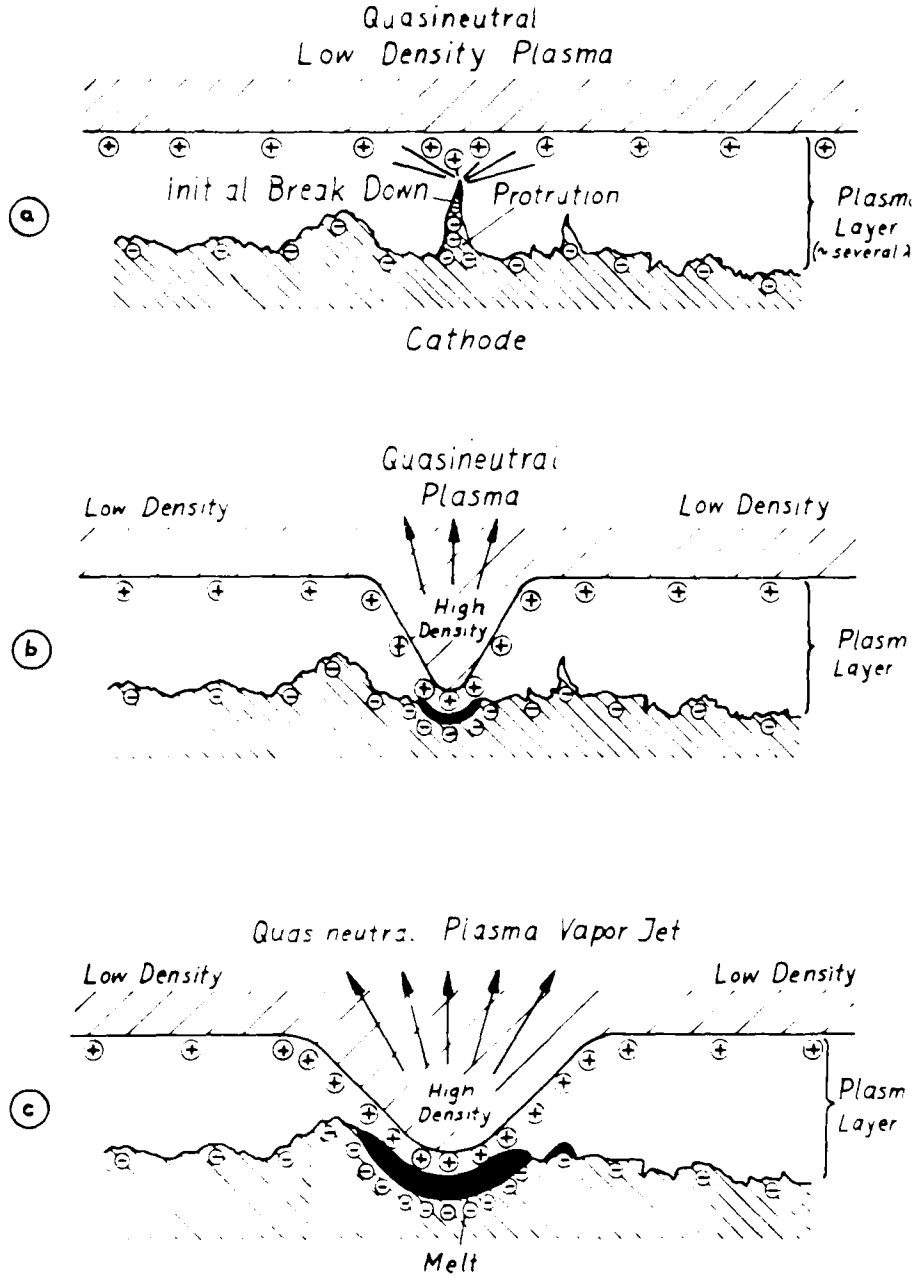

Fig. 37 Development of a microspot: a) initiation of breakdown and vaporization of cathode material, b) plasma layer thickness shrinks drastically, c) spot size growth to its final size due to heat conduction from the plasma to the crater surface (e.g. ion bombardment).

electron emission and therefore to a concentration of the electric current at the initial breakdown point. The high density plasma expands now into the half space, thereby forming a plasma jet; simultaneously the high density plasma is pressed onto the cathode surface, which melts and thereby forms a crater-like pit. Finally, a spot-like discharge as shown in Fig. 37c and discussed in section 3.3 is initiated.

Spot Conditions: The high density, quasi-neutral vapor plasma is now electrically connected with the interelectrode low density plasma and interconnected with the overheated, molten inner crater surface by a space charge layer with a thickness of several Debye length. It can be shown[19] that the Debye length given by

$$\lambda_D = \sqrt{\frac{\varepsilon_0 k T_e}{2e^2 n_e}} = \frac{kT_e}{e}\sqrt{\frac{\varepsilon_0}{2p_e}} \qquad (69)$$

is much smaller than the crater diameter; hence the plasma layer may be treated by a one-dimensional approach. Assuming different temperatures for the electrons T_e and for the heavy particles T_i but taking T_e and T_i constant across the layer, the electric potential U as a function of the distance x from the molten crater surface has been calculated[20] and is plotted in a dimensionless form in Fig. 38. As parameter, one takes here the dimensionless voltage drop, $-(e/kT_e)U_0$, between the electrode or inner crater surface within the range of -0.5 and -10 and the quasi-neutral plasma (at zero potential).

---

[19] H. O. Schrade, M. Auweter-Kurtz, and H. L. Kurtz, "Cathode Erosion Studies on MPD Thrusters," 18th International Electric Propulsion Conference, AIAA 85-2019, Alexandria, VA, 1985.

[20] H. O. Schrade, "Basic Processes of Plasma Propulsion," Interim Scientific Progress Report, Grant AFOSR 82-0298, Sept. 1985.

Fig. 38 shows that the plasma layer width x_d depends on the voltage drop ($-U_0$) and that it can be approximated by

$$x_d \approx \frac{\frac{eU_0}{kT_e} + 1}{\left[\sqrt{\frac{m_i T_e}{m_e T_i}} - 1\right]^{1/2}} \lambda_D$$

$$\approx 4.25 \cdot 10^{-12} \frac{\left(\frac{eU_0}{kT_e} + 1\right) T_e}{\left[\sqrt{M_i}\,\frac{T_e}{T_i} - 0.0234\right]^{1/2} \sqrt{p_e}} \quad [m] \qquad (70)$$

where M_i is the atomic weight of the evaporated and ionized cathode material and p_e is the partial pressure of the electrons in the quasi-neutral plasma above the molten crater surface given in N/m^2. By introducing the ionization degree in the extended form

$$i = \frac{\sum_i z_i n_i}{n_0 + \sum_i n_i} \qquad (71)$$

where n_0 is the number density of the neutral particles and n_i is that of the z_i-times charged ion component, one can replace the partial pressure of the electrons by the plasma pressure p according to the relation

$$p_e = \frac{i\,T_e}{i\,T_e + T_i}\, p \qquad (72)$$

Hence, the plasma layer width becomes

$$x_d \approx 4.25 \cdot 10^{-12} \frac{\frac{eU_0}{kT_e} + 1}{\left[\sqrt{M_i}\,\frac{T_e}{T_i} - 0.0234\right]^{1/2}} \sqrt{T_e + \frac{1}{i} T_i}\, \sqrt{\frac{T_e}{p}} \quad [m] \qquad (72)$$

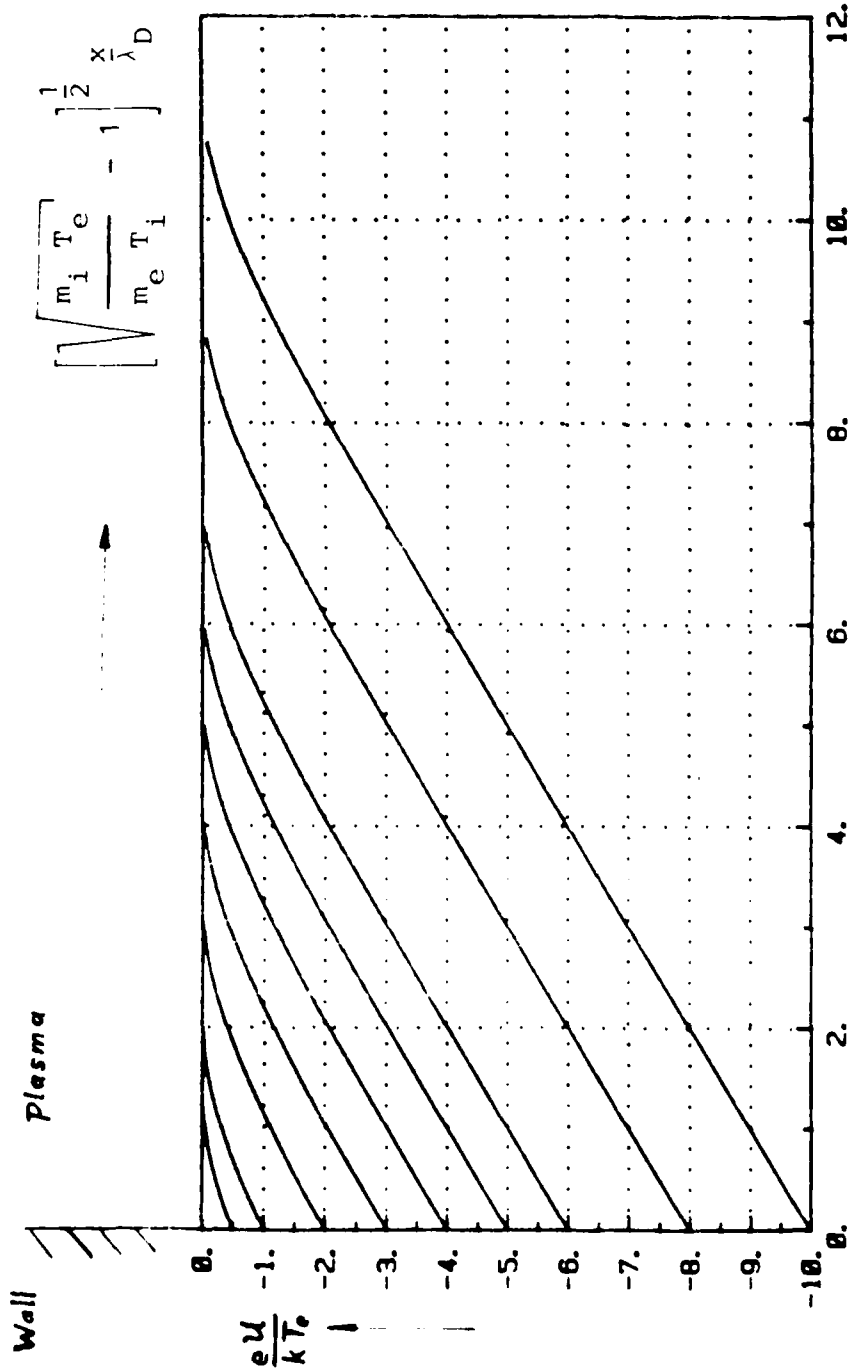

Fig. 38 Normal potential eU/kT_e as a function of the dimensionless distance

$$\left[\sqrt{\frac{m_i T_e}{m_e T_i}} - 1\right]^{1/2} \cdot \frac{x}{\lambda_D}$$

for different wall potentials $-eU_0/kT_e$.

which is for the estimated conditions of the spot plasma ($i \gtrsim 0.1$, $T_e \lesssim 50000$ K $> T_i$, $U_0 < 20$ V and $p > 0.1$ bar = 10^4 N/m^2) $x_d \lesssim 2 \cdot 10^{-8}$ m, i.e. much smaller than the spot size of about 1 µm and more in diameter.

The electric field E_0 at the electrode surface becomes practically independent of the voltage drop and therefore only a function of the plasma properties if eU_0/kT_e exceeds about 2 (see Fig. 38). For this quite reasonable condition, the field at the smooth, molten inner crater surface can be calculated by

$$E(x=0) = E_0 = \frac{kT_e}{e} \frac{1}{\lambda_D} \left[\sqrt{\frac{m_i T_e}{m_e T_i}} - 1\right]^{1/2} \qquad (73)$$

$$\approx 2.03 \cdot 10^7 \left[\sqrt{M_i \frac{T_e}{T_i}} - 0.0234\right]^{1/2} \sqrt{\frac{i\, T_e}{i\, T_e + T_i}\, p}$$

For a tungsten cathode with $M_i = 184$, an ionization degree of $i = 1$ and a plasma pressure of $p > 1$ bar, which is realized in a spot discharge, one obtains for a smooth inner crater surface

$$E_{0,\text{tungsten}} \gtrsim 5 \cdot 10^9 \quad \text{V/m} \qquad (74)$$

Since due to these relatively large fields, small Taylor cones may develop in the crater melt,[21] and the electric field can locally exceed this value by more than one order of magnitude.[19] Now according to Good and Müller,[22] the current density due to thermal field emission is plotted in Fig. 39 as a function of the electric field E_0 for an electron work function of 4.5 eV (tungsten). It shows that

---

[21] G. N. Fursey, "Local Elementary Processes at the Formation and Operation of Vacuum Discharges," presented at the 5th Workshop on Electrode Phenomena (Berlin), May 1982.

[22] R. H. Good Jr. and E. W. Müller, "Field Emission," in Encyclopedia of Physics, "Electron Emission and Gas Discharges I," ed. by S. Flügge, Vol. XXI, Springer Verlag, Berlin, 1956.

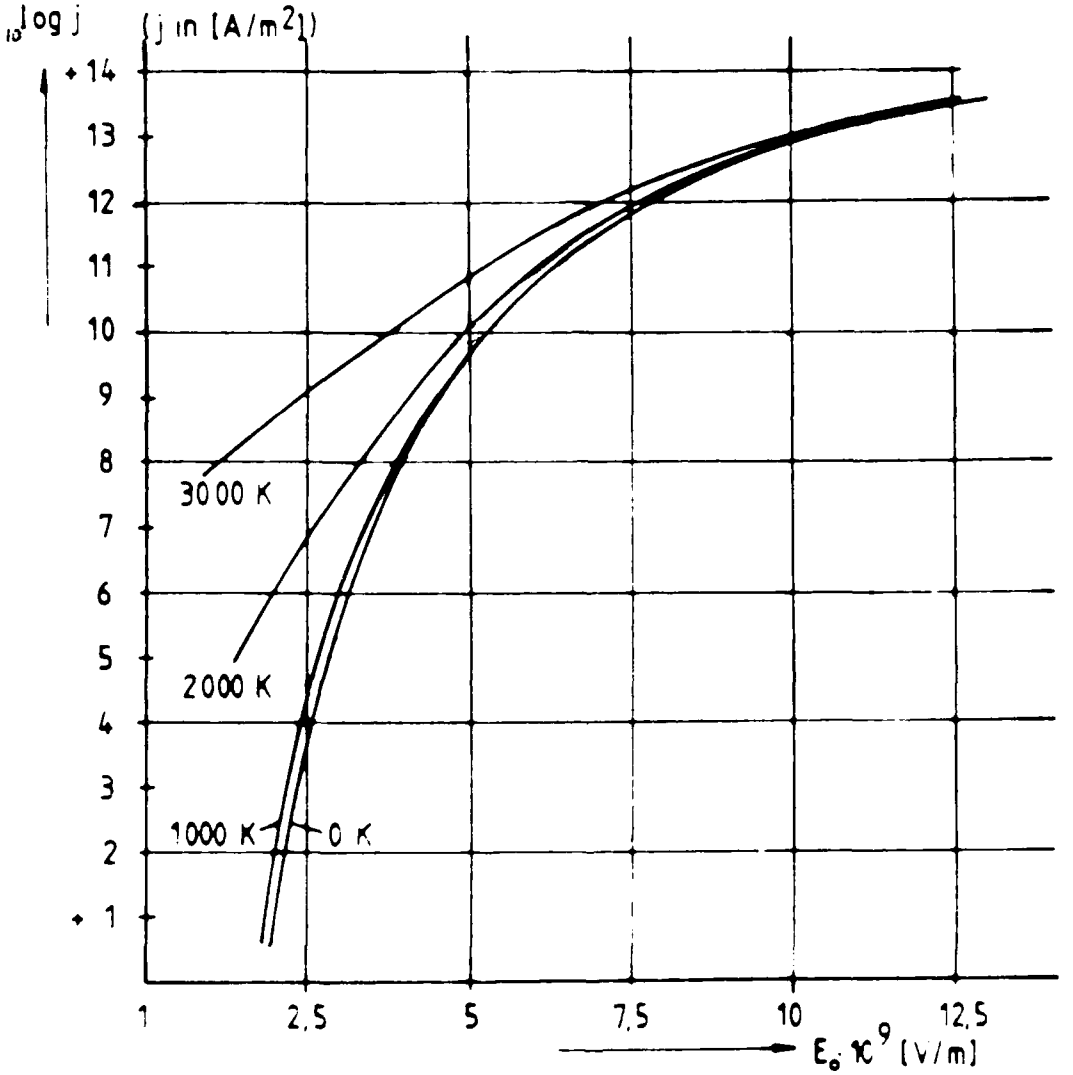

Fig. 39 Current density due to thermal field emission for an electron work function of 4.5 eV (tungsten) according to R. H. Good, Jr. and E. W. Müller.

thermal field emission can explain the extremely high current density values which are observed in spot discharges[23] (up to about 10^{13} A/m^2).

The idea is that at the tip of the Taylor cones the current density may assume values of the order quite beyond that of averaged microspot current densities by measuring the crater sizes and appertaining currents.[15] Based on measured values of I_S/r_0, i.e. spot current divided by spot radius, one can now calculate, by means of criterion eq. (64), the plasma pressure which must be maintained within the crater in order to keep the spot discharge stable. In Table 1, the difference between the critical vapor and plasma pressure p_v and the ambient pressure p_∞ is listed according to the measured (I_S/r_0) values for different cathode materials for a flat and a hemispherical spot crater shape.

Table 1 List of (I_S/r_0) values and the appertaining critical pressure differences $(p_v - p_\infty)$ to maintain a stable spot discharge.

	$\frac{I_S}{r_0}$ [A/m] (measured)	$(p_v - p_\infty)_{crit}$ [bar]	
		flat	hemispherical
W	$2.0 \cdot 10^7$	191	210
Cu	$1.4 \cdot 10^7$	94	103
Mo	$8.3 \cdot 10^6$	33	36
Fe (steel)	$6.0 \cdot 10^5$	0.17	0.19

[23] S. Anders, B. Jüttner, H. Pursch, P. Siemroth, "Investigations of the Current Density in the Cathode Spot of a Vacuum Arc," Contributed in Plasma Physics, Vol. 25, p. 467, 1985.

Spot Dynamics: The microspots are highly nonstationary. They propagate and disappear and, depending on the electrode material (oxide surface layer, surface chemistry) surface roughness, overall temperature and type and pressure of the adjacent residual gas or plasma, these microspots can cluster together to larger spots of different sizes. In a transverse magnetic field, these spots may move discontinuously or jump in the retrograde direction, i.e. opposite to the Lorentzian rule. All these effects are by no means fully understood, but nevertheless the calculations and explanations in the previous section 3.3 show that this strange spot behavior and even Robson drift motion can be explained by a magnetoplasmadynamic instability of the current channel which emanates from the cathode spot. Based on this analysis, a spot discharge becomes unstable (see eq. 64) if the current I_S carried by a spot exceeds a critical value given by

$$I_{s,crit} = 0.55 \cdot \sqrt{\frac{8\pi^2}{\mu_0} r_0^2 (p_v - p_\infty)} \qquad (75)$$

The factor 0.55 is valid for a hemispherical spot crater and changes to 0.58 for a flat one. Instability means that any small disturbance leading to a small bending of the discharge channel causes the channel to bend more and more until it contacts the cathode surface at a nearby site. Thereby the cathode is heated up, the plasma and vapor pressure increase and since the Debye length on the touchdown area becomes very small, a new breakdown and second spot will be initiated. Each of both spots now carries a part of the electric current so that both are stable. By further increasing the current, at least one of the spots will split again. The number of spots will now rise until the final current set by the power supply is reached. The cathode surface will therefore be covered more and more by these microspots, which now, probably due to local accumulation of molten electrode material, cluster together and build larger spots. This spot motion should be statistical if no external

magnetic field and/or flow parallel to the cathode surface is applied, since the instability criterion is independent of the direction of the disturbance, and since the latter is taken ad hoc in all directions equally probable.

If a transverse magnetic field is applied, any disturbance leads either to an unstable bending of the discharge channel in the retrograde direction or to a stable, bent channel configuration in the amperian direction. The consequence is a preferred retrograde spot propagation.

Spot erosion: The erosion rate or material loss due to a spot discharge stems from two mechanisms:

a) evaporation of cathode meterial and
b) ejection of droplets and molten material.

While (a) evaporation starts from the beginning of the spot discharge, the second mechanism (b) occurs after a molten layer has formed and, affected by the high plasma pressure, is thrown out at the rim of the spot crater and/or after that if several unstable spots cause splashing on a preheated molten area. These last mechanisms need a certain time to develop, but they are most destructive and cause not only a dramatic material loss but also a quite severe damage to the cathode surface.

4.2 Experiment

In order to assess the basic processes occuring on cathodes of MPD thrusters and related arc devices, and in order to supplement the theoretical work on cathode phenomena, the following experimental arrangement has been set up and tests carried out.

Experimental Setup: The experimental arrangement is shown in Fig. 40. Within a vacuum test vessel, an electrode system as shown in Fig. 41 is charged with an approximately rectangular current pulse of a PFN.[24] It allows the initiation of an arc discharge of up to 1 kA for about 2 ms at pressures between 10^{-1} and 10^{4} Pa. The anode consists of a molybdenum rod which is rectangularly oriented with respect to a cylindrical cathode. The cathode, a metal rod, is clamped between two water-cooled terminals such that an auxiliary electric current can flow through the cathode rods and so that the samples can be easily exchanged. Using this arrangement, the cathode attachment can be investigated within a defined magnetic field and under different temperatures, depending on the auxiliary current I_a, on the material, and on the diameter d_s of the samples. The transverse magnetic induction field at the surface of the cathode amounts to

$$B_0 = \frac{\mu_0}{\pi} \frac{I_a}{d_s} \tag{76}$$

and the temperature of the sample which now variates along its axis can again be controlled by the auxiliary current setting and the heat conduction at both clamps. The shortcoming of this arrangement, that the magnetic field effects cannot be investigated independently of the surface temperature, are overcome to a certain extent by accounting for the relatively large time to ohmically heat up or cool down the

[24] P. Lehniger, "Designing and Building of a Test Rig in Order to Measure Cathode Erosion Caused by a Pulsed Arc," Senior Thesis, IRS, University of Stuttgart, Sept. 1986.

Fig. 40 Experimental setup.

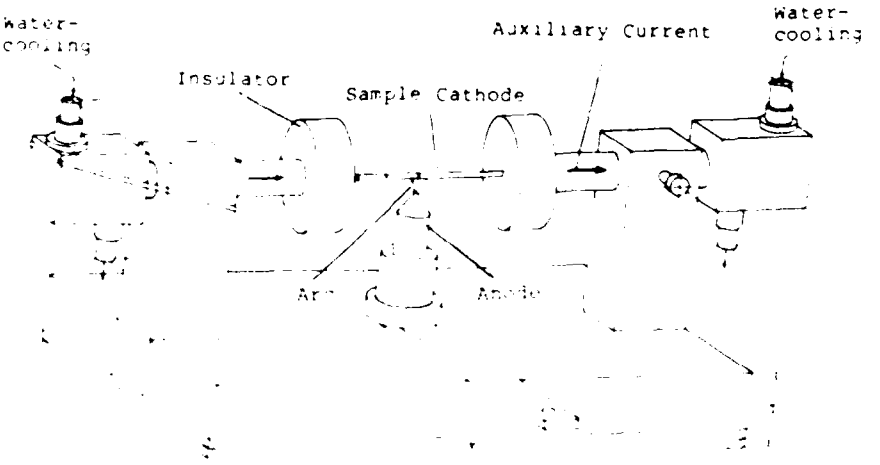

Fig. 41 Electrode test rig.

samples. In order to run the sample at fairly low temperatures with high B_0 fields, one switches on the auxiliary current simultaneously with the main current impulse, and in order to maintain high temperatures with low B_0 fields, one switches it off before starting the main arc current pulse.

The main arc current pulse is initiated by means of an ignition plug which ejects a plasma into the gap region between cathode and anode and hereby discharges the PFN. A typical current-voltage characteristic of the discharge is plotted in Fig. 42, and the average current $\bar{I}$ as a function of the changing voltage U_L is plotted in Fig. 43.

Measurements of the Arc Characteristic: The measurements of the U(t) - I(t) characteristic of the main current pulse occur according to the following experimental set up (see Fig. 44). The arc current is picked up by means of a current transformer (4) and its signal fed to a transient recorder (5) (Biomation Type 802). The voltage pulse is measured via an isolation amplifier (7) and recorded by another Biomation Type 805 (8). The pulse shapes of both the current and voltage traces are then recorded by an x-y plotter (9) and by an oscillograph (6) for rechecking. The pressure in the chamber is taken by means of a Penning vacuum gauge in the range below 10^{-3} mbar and above this range by a Pirani pressure gauge.

Calibration of the Cathode Temperature: In order to calibrate the temperature of the cathode sample (thoriated tungsten) as a function of the B or heating current or as a function of the shunt voltage U_{sh}, the sample temperature was measured at three different locations with NiCr-Ni thermo elements up to a temperature of almost 1800° K and a pyrometer from about 1250° K to almost 2500° K in the middle of the sample. The water-cooling setting of the mounting supports on both ends of the sample remained constant, and the pressure within the chamber was 10^{-4} mbar. The scheme of the test assembly is shown in Fig. 45. The thermocouples

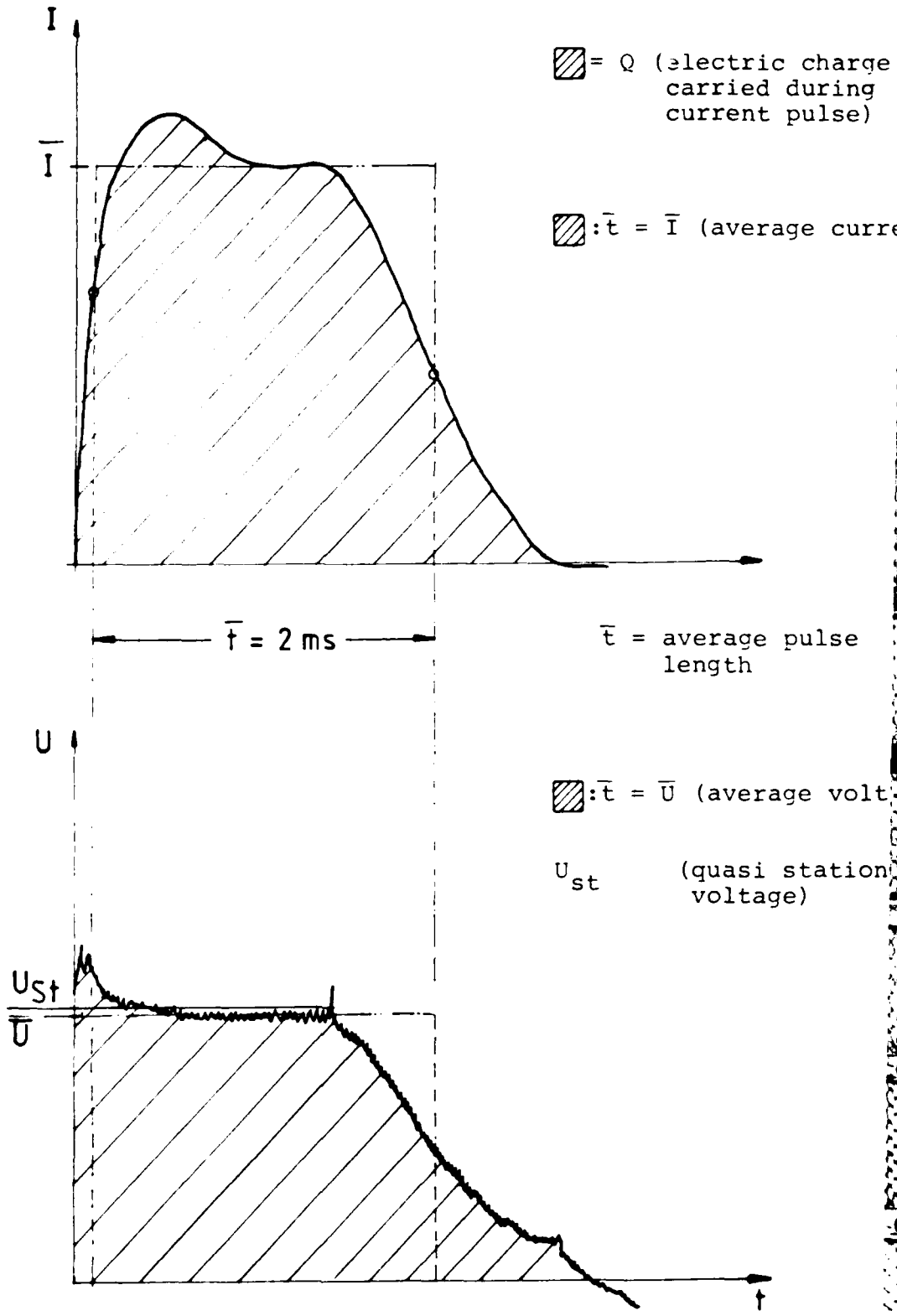

Fig. 42 Typical I(t)- and U(t) Characteristics during the Discharge Pulse

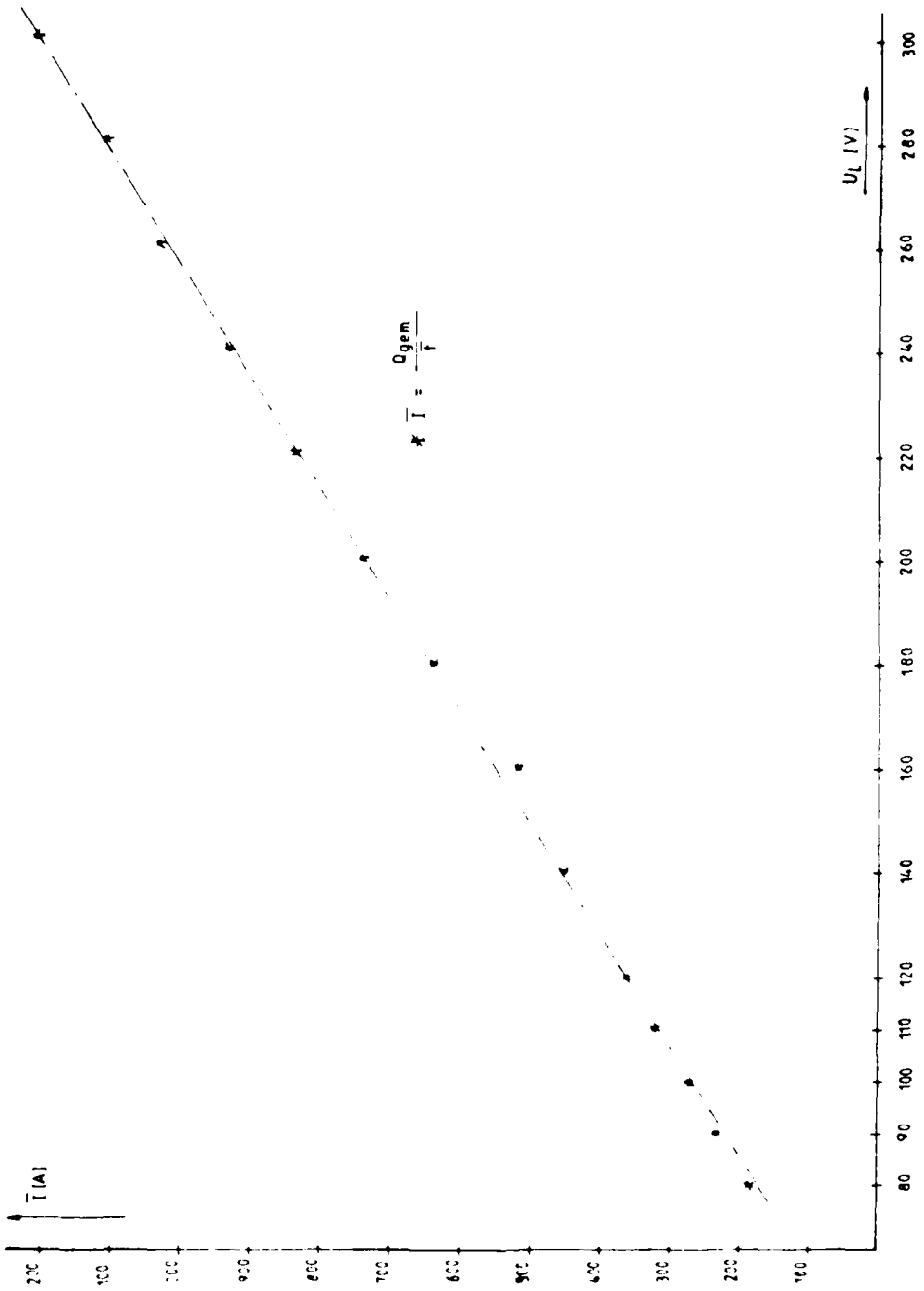

Fig. 43 Average Current $\bar{I}$ as Function of Charging Voltage U_L

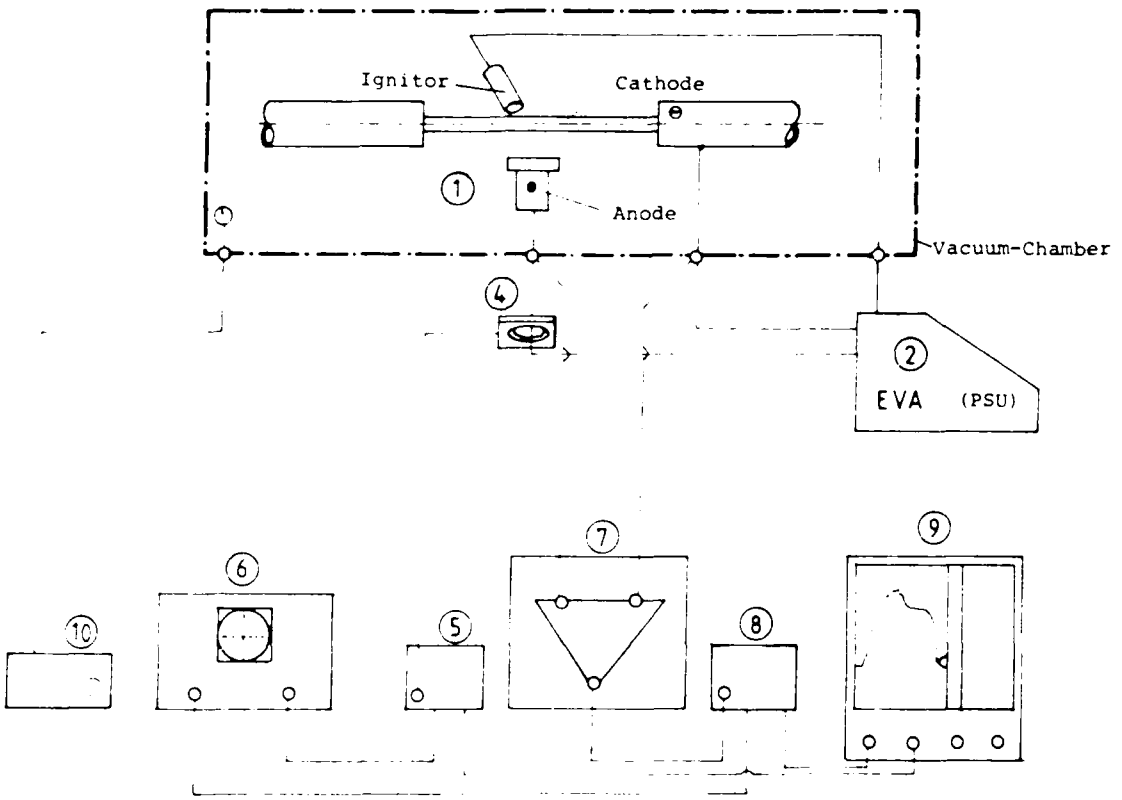

Fig. 44 Test assembly to measure the U(t) and I(t) characteristics of the arc pulse

The numbers stand for:

1 Cathode erosion experiment
2 Power supply unit in form of pulse-forming network
3 Pyrometer (not figured on this page)
4 301X Pearson Current Transformer
5 Transient Recorder Type Biomation 802
6 Oscilloscope Type 556 (Tektronix)
7 Fast Isolation Amplifier (Leverkus Elektronik)
8 Transient Recorder Type Biomation 805
9 x/y-Plotter Type 3077 (Yogawa)
10 Pressure-Gauge and -Indicator (Leybold-Heraeus)

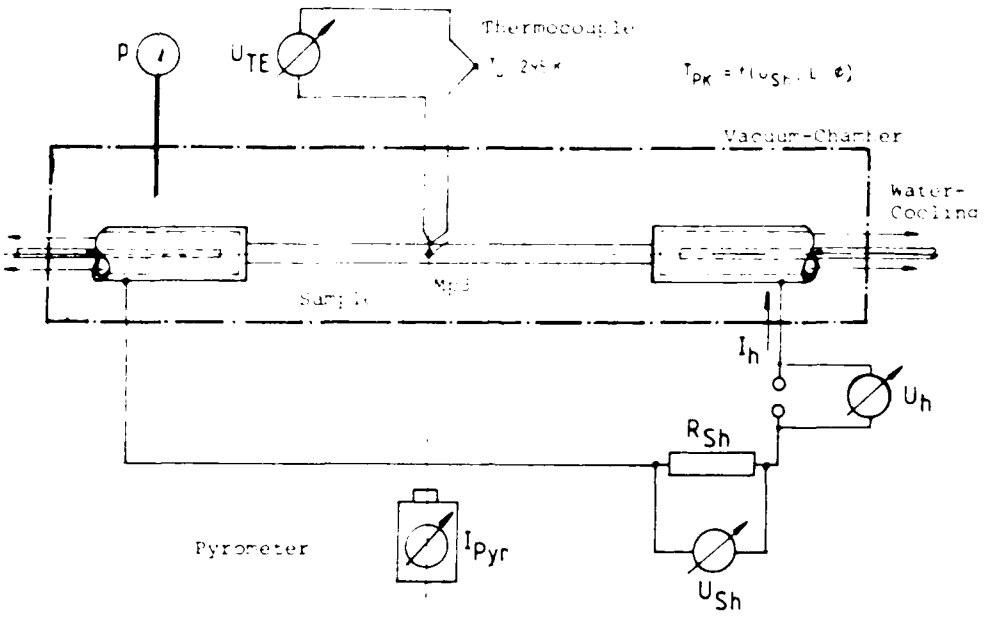

Fig.45 Sheme of Test Assembly for Temperature Calibration

The Abbrevations stand for:

T_{PK}	Sample Temperature
I_h	Heating Current
U_h	Heating Voltage
R_{Sh}	Shunt ($R = 2.4 \cdot 10^{-4}$ Ohm)
U_{Sh}	Shunt Voltage
I_{pyr}	Pyrometer Current
U_{TE}	Thermoelectrical Voltage
p	Pressure in the Vacuum-Chamber
T_u	Thermocouple Reference Temperature

were placed in small holes, and the pyrometer was oriented to these holes in order to approach black body conditions. In Fig. 46, the temperature distribution along the cathode sample is plotted for different auxiliary or heating currents.

Cathode Measurements: The photomicrographs in Fig. 47 show typical arc traces left at the edge of the main arc impact area on a thoriated tungsten electrode at room temperature. The charging voltage and the average current amounted in this experiment to $U_L \approx 160$ V and about $I \approx 550$ A, respectively. The lower picture is a magnification of the lower left crater in the upper picture. In Fig. 48, the traces left on the main arc impact area of a steel cathode are shown for average currents of a) $\approx$ 180 A and b) $\approx$ 550 A. At the lower current, one still observes individual craters of different sizes which partially overlap and/or build larger molten areas of spot clusters. At the higher current (b), the entire frame indicates an overall originally molten area, and it seems reasonable to assume that the arc attachment was still spotty but caused detrimental "splashing" of the surface material. At the edge of the main impact area (see Figs. 49a and b), the molten zones are still confined to small individual craters of about a few tens of a micron to several microns. In Fig. 49b, the middle crater of Fig. 49a is enlarged. The micrographs in Fig. 50a,b show the arc traces on aluminum within the main impact area for 180 and 550 A and look similar to Fig. 48b, i.e. like an overall originally molten area.

It is obvious that the arc attachment on a cold (room temperature) metal cathode is spotty and highly non-stationary. The spots jump around the surface but prefer an area which is closest to the anode. This area, heavily impacted by spots, starts to melt and thus seems to become an even more preferred attachment region. This preferred sticking leads to an increased evaporation of cathode material, to splashing and to droplet ejection. In order to avoid this extreme erosion, one must try to obtain many small spots

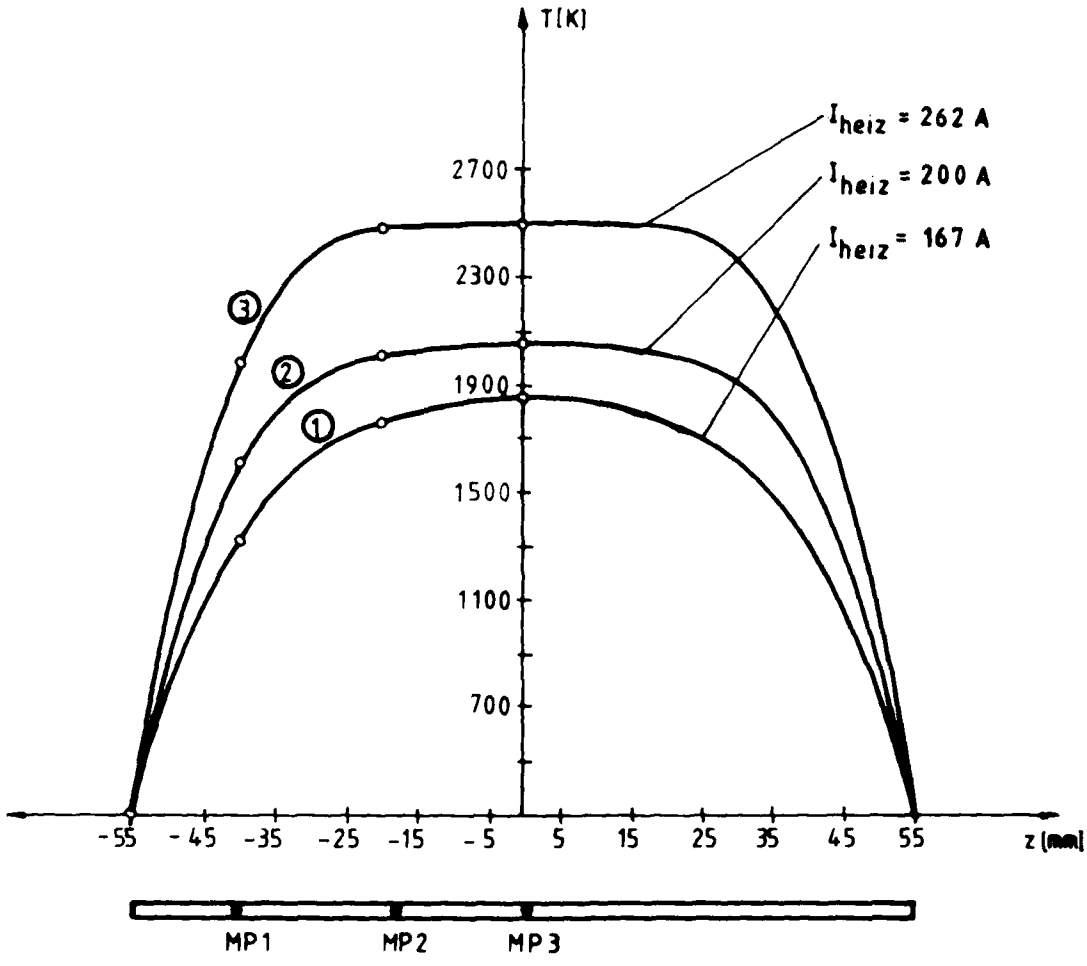

Fig. 46

Temperature Distribution along the Cathode Sample (Tungsten: 2% ThO_2)

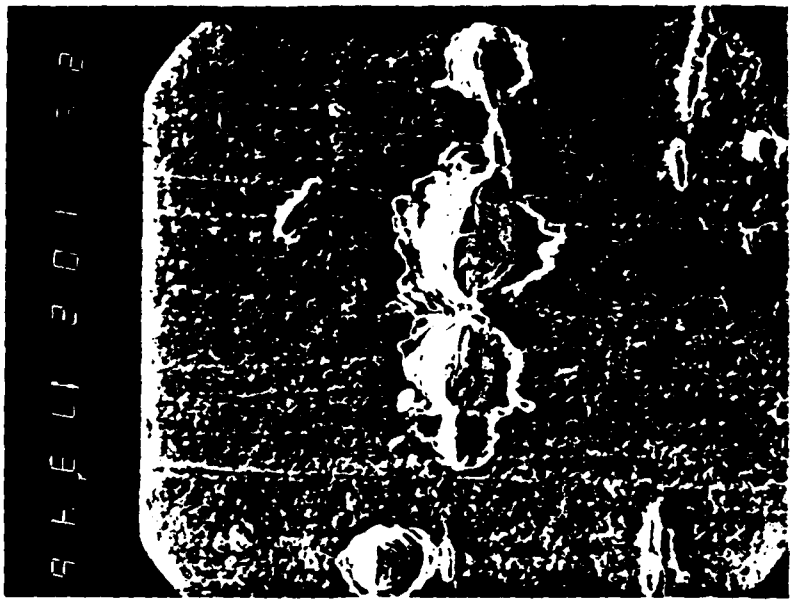

a) Magnification 1000 : 1

b) Magnification 8000 : 1

Fig. 47 Photomicrographs of cathode spot craters on a thoriated (2% ThO_2) tungsten surface

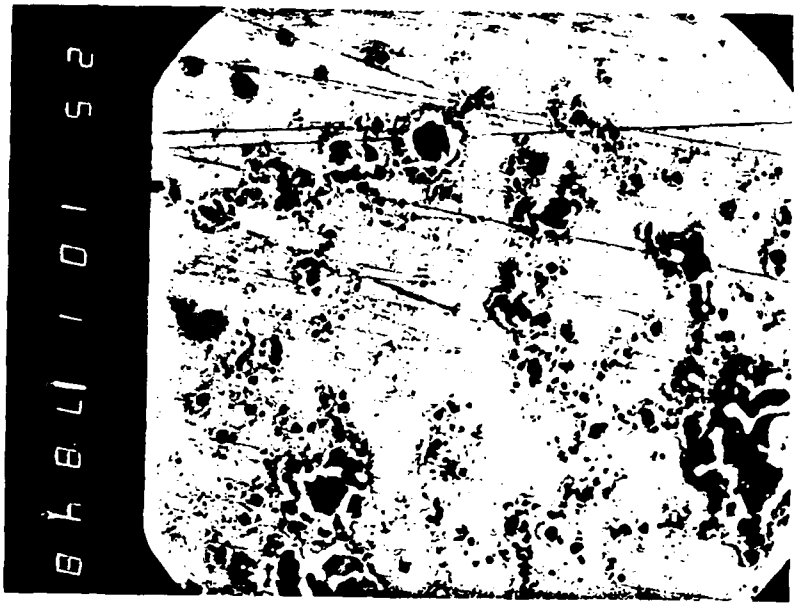

a) Magnification 100 : 1

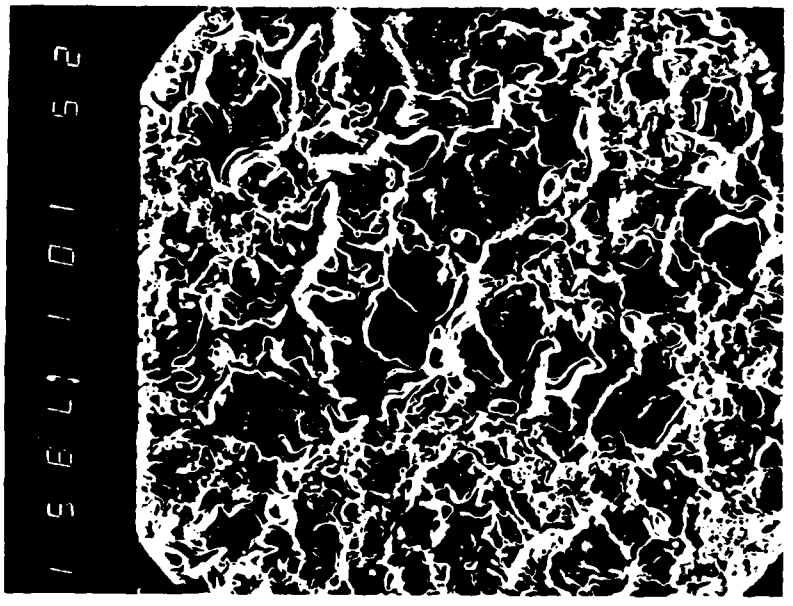

b) Magnification 100 : 1

Fig. 48 Photomicrograph of a steel cathode surface at the main arc impact area for an average current of

a) $\bar{I} \approx 180$ A

b) $\bar{I} \approx 550$ A

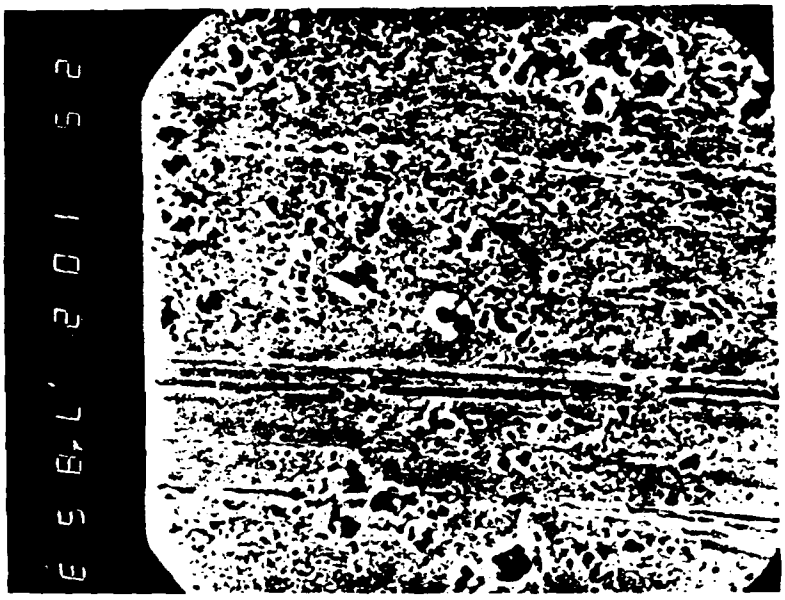

a) Magnification 1000 : 1

b) Magnification 8000 : 1

Fig. 49 Photomicrograph of a steel cathode surface at the edge of the main arc impact area

($\bar{I} \approx 550$ A)

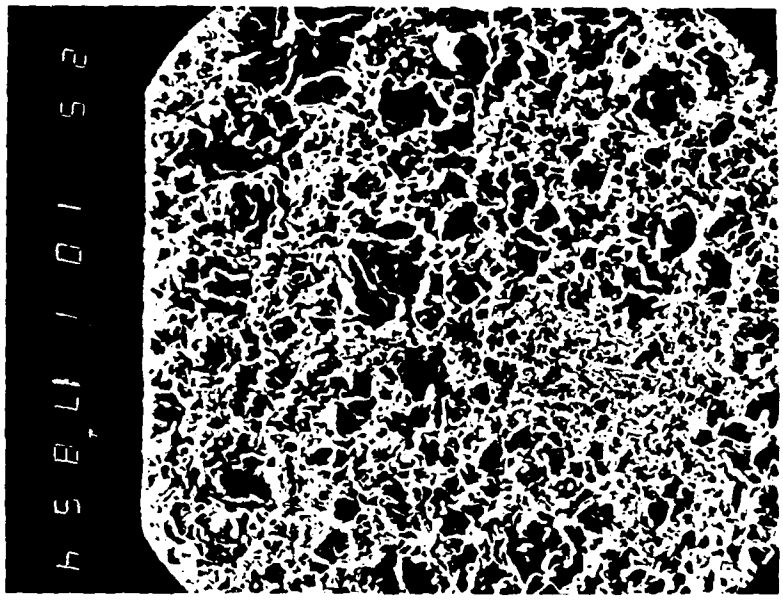

a) Magnification 100 : 1

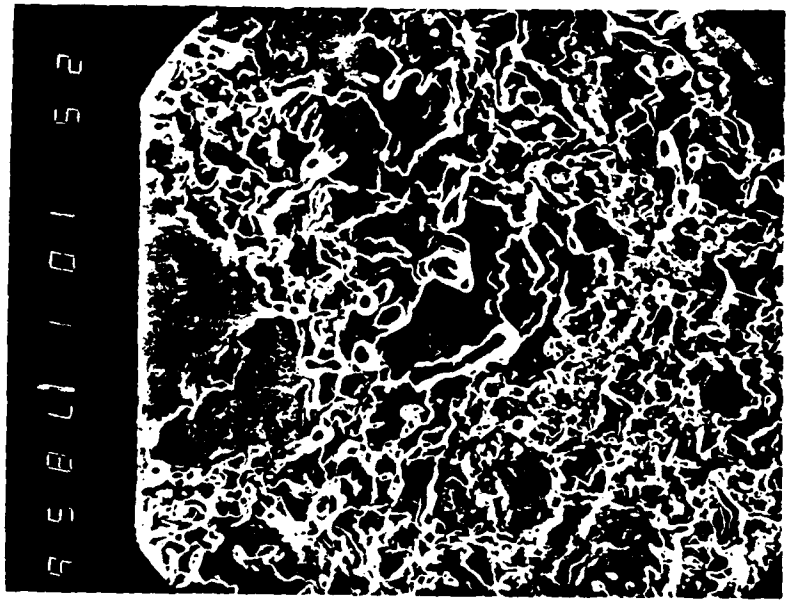

b) Magnification 100 : 1

Fig. 50 Photomicrograph of an aluminum cathode surface at the main arc impact area

a) $\bar{I} \approx 180$ A

b) $\bar{I} \approx 550$ A

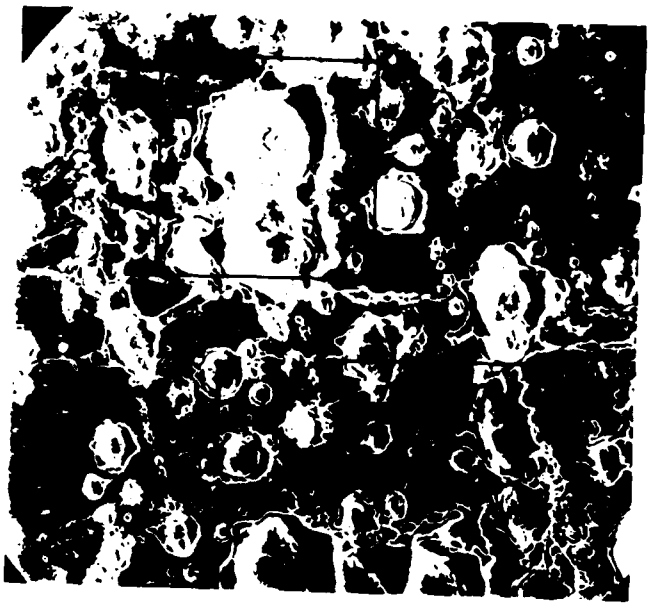

a)

500: 1

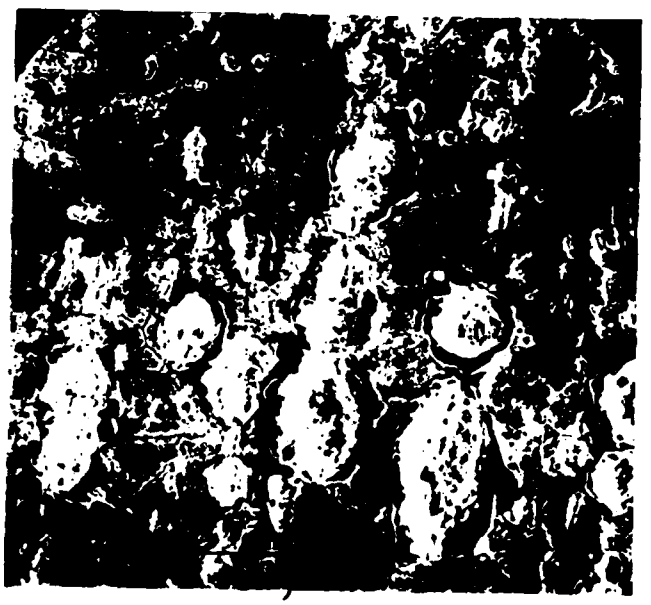

b)

1000 : 1

Fig. 51 Photomicrograph of a thoriated tungsten cathode (2% ThO_2) at a) 1500° K and b) 2000° K.

which rapidly jump over a large area but which should not cause an overall molten surface. This last condition seems to be realized with a so-called thermionically emitting tungsten cathode at fairly high temperatures but below melting point.[19]

Two photomicrographs of spot craters left on thoriated tungsten cathodes heated up to 1500° K and 2000° K are shown in Figs. 51a and b, respectively. At the higher temperature, an alignment of the spots can be seen parallel to the cathode axis, which indicates that due to the B_θ field of the higher auxiliary heating current I_a ($\approx$ 200 A), the spots move now either in the amperian or--what is more likely--in the retrograde direction.

The erosion rate ε has been determined by weighing the electrode mass loss and by measuring the appropriate electric charge transferred across the cathode surface. In order to obtain measurable quantities in mass loss, one adds up hundreds and even thousands of discharge pulses. The results of these automatically run and registered current pulses are shown in Table 2 for different materials at about 50° C.

The erosion rates for thoriated tungsten in these tests are by a factor of about two higher than those measured in a pulsed nozzle-type thruster.[13] This discrepancy is very likely caused by the different geometries of the anode. In this experiment with a pinned anode rod, the arc strikes the cathode in a more confined main impact area, thereby causing a clustering of microspots and a stronger droplet ejection than in a coaxial electrode device, in which the spots are spread over a larger area and therefore do not cluster as much.

Erosion measurements on hot, glowing thoriated tungsten cathodes so far did not result in reliable and reproducible data. With an increasing number of pulses, the brightness of the glowing cathode diminished noticeably, despite a constant heating current. Very likely the radiation or emission

Table 2 Erosion rates for different cathode surfaces.

	Number of Current Pulses	Measured Erosion Rate
Thoriated Tungsten (2% ThO_2) (not polished)	300	35 µg/C
	5000	41 µg/C
Thoriated Tungsten (2% ThO_2) (polished)	100	29 µg/C
	500	34 µg/C
	6000	42 µg/C
Pure Tungsten (not polished)	100	44 µg/C
	500	50 µg/C
	5000	54 µg/C
Copper (not polished)	200	73 µg/C
	800	77 µg/C
Copper (polished)	100	74 µg/C
	800	75 µg/C

constant of the cathode sample changed due to convection and/or chemical effects of evaporated insulator material on the tungsten surface. Even several days of outgasing did not show a marked improvement. In order to avoid any problematic insulation material and to improve the mechanism of both terminal fastening mechanisms, the design is being somewhat altered.

5. List of Reports and Publications

During the period of the research grant, the following reports, papers and student theses have been accomplished.

Reports

Scientific Progress Reports
on the theme
"Basic Processes of Plasma Propulsion" Sept. 1983
Sept. 1984
Sept. 1985

Interim Scientific Reports

H. O. Schrade, "Magnetoplasmadynamic Effects in Electric Arcs" Aug. 1983

H.O. Schrade, H.L. Kurtz, M. Auweter-Kurtz and M. Kirschner, "Analysis of the Dissipation Mechanism within an Instationary Cathode Spot of Metalvapor Arcs" Aug. 1984

Student Theses

J. P. Schleinitz, "Numerical Calculation of the Flow and the Electric Current Contour Lines in an MPD Self-Field Accelerator" June 1985

P. Chr. Sleziona, "Instationary Calculation of the Electric Current Contour Lines and the Flow Field within a Cylindrical MPD Propulsion Device" April 1986

P. Lehniger, "Designing and Building of a Test Rig in Order to Measure Cathode Erosion Caused by a Pulsed Arc" Sept. 1986

Tze Wing Poon, "MPD Effects in Electric Arcs," Postgraduate Student Paper, IRS Report, University of Stuttgart Sept. 1986

Papers and Publications

H. O. Schrade, M. Auweter-Kurtz, and H. L. Kurtz, "Analysis of the Cathode Spot of Metal Vapor Arcs," IEEE Transactions on Plasma Science, Vol. PS-11, p. 103, 1983.

H. O. Schrade, M. Auweter-Kurtz, and H. L. Kurtz, "Stability Problems in Magneto Plasmadynamic Arc Thrusters," AIAA-85-1633, 18th Fluid Dynamics and Plasmadynamics and Lasers Conference, July 1985.

H. O. Schrade, M. Auweter-Kurtz, and H. L. Kurtz, "Cathode Erosion Studies on MPD Thrusters," 18th International Electric Propulsion Conference, AIAA 85-2019, Alexandria, VA, 1985. (Also partially supported through Grant 84-0394.)

6. Summary

In order to gain a more profound understanding of the fundamental processes occuring in coaxial arc jets and MPD arc thrusters, and in order to eventually end up with reliable design criteria and/or predict thruster performances under various conditions, the following research program under the three headings

I. Flow Discharge Calculations
II. Stability Theory
III. Electrode Investigations

has been conducted.

Under heading 1, the current density distribution, flow, pressure, and density fields are calculated for a (quasi-) steady nozzle-type MPD thruster, and a computer program to calculate the thrust as a function of the thruster geometry and as a function of the arc current and the mass flow rate has been written. These model calculations are based on a partially two-dimensional approach, assuming a fully singly ionized plasma with an isothermal electron and an adiabatic ion behavior. The influence of the $\vec{j} \times \vec{B}$ forces on the axial acceleration and on the radial density distribution is presented. The results are compared with experimental findings. Under the same heading, a rigorous computer program is being developed which allows determination of the pressure, flow and density (temperature) fields within a pulsed, cylindrical MPD accelerator. As initial conditions, one assumes a homogeneous radial current within a confined axial electrode region and a supersonic homogeneous axial flow. For a given current rise, the current contour lines and the flow, pressure, and density fields within the cylindrical flow discharge region are calculated as a function of time.

Under heading II, a unique theoretical approach is presented which allows determination of the stability behavior of an arbitrarily shaped current-carrying plasma channel under various conditions. In comparison to the common stability investigations (e.g. Normal Mode), this method is based on the force balance of a discharge channel. The resultant force which acts on a current-carrying plasma channel per unit axis length is calculated among others as a function of the local channel geometry such as channel diameter, radius of curvature, etc. In this resultant force, one also accounts for magnetoplasmadynamically induced propelling effects. The criterion for a balanced and stable channel configuration follows now by the requirement that the resultant force for that configuation must be zero along the discharge axis and that any small deviation from that configuration leads to a force which brings the channel back into its original balanced configuration. Based on this novel stability theory, the onset phenomenon observed in any nozzle-type MPD arc jets can be predicted, and the calculated results compared with measurements so far agree quite well. Moreover, this stability theory can explain the very strange behavior of arc spots and the, until now, seemingly obscure retrograde motion of arcs in a transverse magnetic field.

Under heading III, the cathode attachment of electric arcs are theoretically and experimentally investigated. It is shown that the spotty attachment observed mainly on cold cathode surfaces leaves tracks in the form of craters which are seemingly statistically distributed, with a concentration at the main impact area when no magnetic field is present. Within a transverse magnetic field, these spots align themselves with the amperian or retrograde direction. The erosion effects and the surface damage due to spots are discussed; they stem from evaporation, droplet ejection, and/or splashing. The most severe damage to the cathode surface occurs when many samll spots cluster together and build one or even several larger spots which now cause melting and splashing.

Appendix I

Together with the continuity equation

$$\nabla(\rho\vec{v}) = 0 \tag{I.1}$$

the equation of motion (2) can be written as

$$\rho(\vec{v}\cdot\nabla)\vec{v} + \nabla\cdot\vec{P} = \vec{j} \times \vec{B} \tag{I.2}$$

By taking a one-dimensional approach along the flow axis (z-axis) and by neglecting friction, one obtains

$$\rho v \frac{d}{dz} v + \frac{d}{dz} p = (\vec{j} \times \vec{B})_z \tag{I.3}$$

where v is the average velocity in the z-direction and p the average gas or plasma pressure across a cross sectional area A of the nozzle. Now from the continuity equation it follows that the mass flow rate through all areas A = A(z) is the same, i.e.

$$\dot{m} = \rho v A = \rho_t v_t A_t \tag{I.4}$$

where the index t stands for the nozzle throat. Applying eq. (I,4) one may now rearrange eq. (I,3) into

$$d\frac{v^2}{2} + \frac{dp}{\rho} = \frac{1}{\dot{m}} v\cdot(\vec{j} \times \vec{B})_z \cdot A\, dz \tag{I.5}$$

In order to relate the pressure p with the mass density ρ, it is

$$p = p_e + p_i + p_0 \equiv p_e + p_{i0} \tag{I.6}$$

where $$p_e = n_e k T_e = \alpha \rho \frac{R}{M} T_e \tag{I.7}$$

is the partial pressure of the electrons, T_e is the electron temperature and α is the degree of ionization defined

AD-A179 884 BASIC PROCESSES OF PLASMA PROPULSION(U) STUTTGART UNIV 2/2
(GERMANY F R) INSTR FUER RAUMFAHRTSYSTEME
H O SCHRADE ET AL 30 JAN 87 AFOSR-VR-87-0557
UNCLASSIFIED AFOSR-82-0298 F/G 21/3 NL

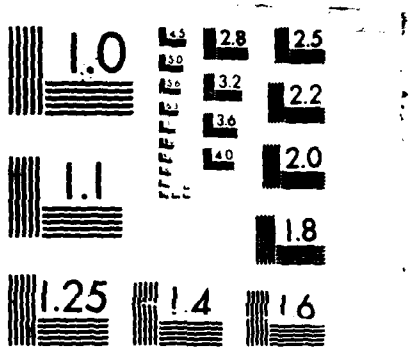

by the quotient of the electron number density and the heavy particle density.

$$\alpha = \frac{n_e}{n_0 + n_i} \tag{I.8}$$

The partial pressure due to all heavy particles like ions and neutrals follows according to their isentropic behavior by

$$p_{0i} = p_0 + p_i = \rho \frac{R}{M} T = p_{0i,t} \left(\frac{\rho}{\rho_t}\right)^{\kappa} \tag{I.9}$$

where T is the heavy particle temperature, R is the universal gas constant, M is the molecular weight of the plasma and κ is the quotient of the specific heat. The index t refers again to the partial pressure and the mass density in the nozzle throat. According to eq. (I,6) together with eqs. (I,7) and (I,9), it follows now that for an isothermal electron and an isentropic heavy particle behavior

$$p = \rho \left\{\alpha \frac{R}{M} T_e + \frac{p_{0i,t}}{\rho_t} \left(\frac{\rho}{\rho_t}\right)^{\kappa-1}\right\} \tag{I.10}$$

and

$$dp = \left\{\alpha \frac{R}{M} T_e + \kappa \frac{p_{0i,t}}{\rho_t} \left(\frac{\rho}{\rho_t}\right)^{\kappa-1}\right\} d\rho \tag{I.11}$$

Herein one assumes that the degree of ionization α remains constant during the expansion process (frozen flow condition). Hence it is also according to eq. (I,9)

$$\frac{1}{\rho} dp = d\left\{\alpha \frac{R}{M} T_e \ln \rho + \frac{\kappa}{\kappa-1} \frac{R}{M} T_t \left(\frac{\rho}{\rho_t}\right)^{\kappa-1}\right\} \tag{I.12}$$

Introduced into eq. (10) yields

$$d\{\frac{v^2}{2} + \frac{R}{M} T_t \left[\alpha \left(\frac{T_e}{T_t}\right) \ln \rho + \frac{\kappa}{\kappa-1} \left[\left(\frac{\rho}{\rho_t}\right)^{\kappa-1} - 1\right]\right]\}$$

$$= \frac{1}{\dot{m}} \int_{z_t}^{z} v(\vec{j} \times \vec{B})_z \cdot A \, dz \qquad (I.13)$$

or since at $z = z_t$, one assumes a fully developed flow, i.e.

$$\frac{dA}{A} = 0 \qquad \text{and} \qquad (\vec{j} \times \vec{B})_z = 0 \qquad \text{at} \qquad z = z_t$$

from eqs. (I,3) and (I,4) follows

$$v_t = \sqrt{\frac{dp}{d\rho}} = \text{speed of sound}$$

$$= \sqrt{(1 + \alpha) \frac{R}{M} T_t} \qquad (I.14)$$

Herein one assumes that within the throat the plasma behaves isothermally. This assumption is plausible, since the average temperature T_t of the throat cross section is determined by ohmic heating and radial heat (and possible radiation) losses (see Appendix A). Hence, according to eq. (I,14), the square of the axial velocity at any cross section z downstream of the nozzle throat follows by

$$v^2 = 2 \frac{R}{M} T_t \left\{\frac{1+\alpha}{2} + \alpha \ln \left(\frac{\rho_t}{\rho}\right) + \frac{\kappa}{\kappa-1} \left[1 - \left(\frac{\rho}{\rho_t}\right)^{\kappa-1}\right]\right\}$$

$$+ \frac{2}{\dot{m}} \int_{z_t}^{z} v \, (\vec{j} \times \vec{B})_z \cdot A \, dz \qquad (I.15)$$

Or by dividing through v_t^2, one obtains an integral equation for $\left(\frac{v}{v_t}\right)$ in the form

$$\boxed{\left(\frac{v}{v_t}\right)^2 = 1 + \frac{2\alpha}{1 + \alpha} \ln\left|\frac{A}{A_t} \left(\frac{v}{v_t}\right)\right| + \frac{2}{1+\alpha} \cdot \frac{\kappa}{\kappa-1} \left[1 - \left(\frac{A_t}{A} \frac{v_t}{v}\right)^{\kappa-1}\right]}$$

$$\boxed{+ \frac{2}{\dot{m} v_t} \int_{z_t}^{z} \left(\frac{v}{v_t}\right) (\vec{j} \times \vec{B})_z \cdot A(z) \, dz \qquad (I.16)}$$

The thrust according to eq. (6) given by

$$Th = \dot{m}\, v_{ex} + A_{ex}\, p_{ex} + \left| \int_{V_2} \vec{j} \times \vec{B}\, dV \right| \qquad (I.17)$$

can now be rewritten by replacing p_{ex} according to (I,10). It is

$$p_{ex} = \rho_{ex} \frac{R}{M} T_t + \frac{R}{M} T_t \left\{ \alpha \left(\frac{\rho_{ex}}{\rho_t} \right)^{\kappa-1} \right\} \qquad (I.18)$$

and introduced into (I,17) yields

$$Th = \dot{m}\, v_{ex} + A_{ex}\, \rho_{ex} \frac{R}{M} T_t \left\{ \alpha + \left(\frac{\rho_{ex}}{\rho_t} \right)^{\kappa-1} \right\} + \left| \int_{V_2} \vec{j} \times \vec{B}\, dV \right| \qquad (I.19)$$

Together with the continuity equation

$$\dot{m} = A_t \rho_t v_t = A_{ex} \rho_{ex} v_{ex}$$

and the relation eq. (I,14)

$$v_t^{\,2} = (1 + \alpha) \frac{R}{M} T_t$$

one obtains for the thrust

$$Th = \dot{m}\, v_t \left\{ \frac{v_{ex}}{v_t} + \frac{1}{1+\alpha} \frac{v_t}{v_{ex}} \left[\alpha + \left(\frac{v_t A_t}{v_{ex} A_{ex}} \right)^{\kappa-1} \right] + \left| \int_{V_2} \vec{j} \times \vec{B}\, dV \right| \right. \qquad (I.20)$$

Appendix II

Calculation of the nozzle throat condition.

According to the continuity equation

$$\dot{m} = A \rho v = \text{const.}$$

one obtains along a flow line

$$\frac{dv}{v} + \frac{d\rho}{\rho} + \frac{dA}{A} = 0 \qquad \text{(II.1)}$$

and for the equation of motion [see also (I.3)]

$$\frac{dv}{v} + \frac{dp}{\rho v^2} = \frac{[\vec{j} \times \vec{B}]_z}{\rho v^2} dz \qquad \text{(II.2)}$$

Since now within the nozzle throat

$$dA = 0 \text{ and } [\vec{j} \times \vec{B}]_z = 0$$

one obtains form eqs. (II.1) and (II.2)

$$v_t^2 = \left(\frac{dp}{d\rho}\right)_t = \text{speed of sound} \qquad \text{(II.3)}$$

and since one may assume isothermal behavior in the nozzle throat according to eq. (I.11) or (III.3), it is

$$v_t^2 = (1 + \alpha) \frac{k}{m_0} T_t = (1 + \alpha) \frac{R}{M} T_t \qquad \text{(II.4)}$$

In order to relate the average temperature across the nozzle throat $T_t = T_e$ to the arc current I, the supposition of a "fully developed arc column" within the throat will be made, i.e. all the ohmic heat input per unit arc length is dissipated away radially by heat conduction and possibly by radiation (see Fig. II.1). This assumption is quite reasonable, since the axial temperature gradient is much smaller than the radial one and since any heat input at the smallest cross sectional area cannot increase the velocity beyond the

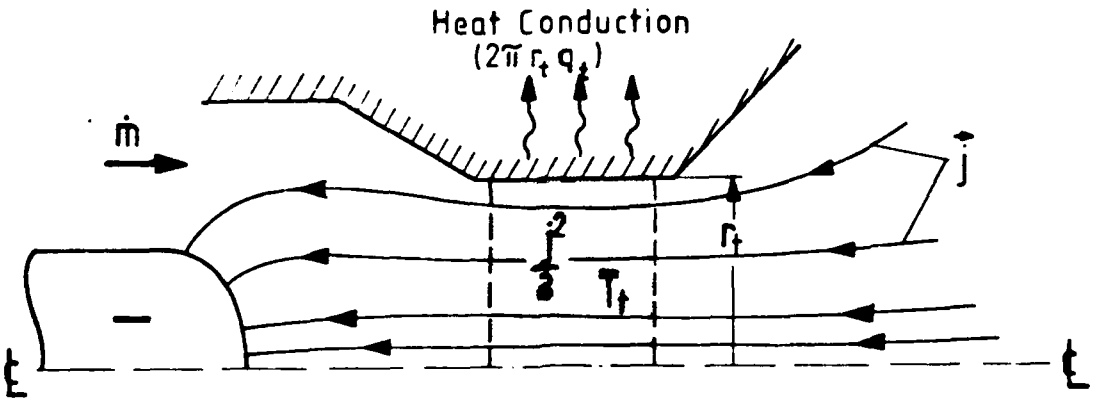

Fig. II.1 Developed flow conditions within the nozzle throat.

speed of sound. Hence the governing equation for the nozzle throat is

$$\nabla \vec{q} = \frac{j^2}{\sigma} - RL \qquad (II.5)$$

where $$\vec{q} = - \lambda \frac{d}{dr} T \vec{u}_r$$

is the heat flux vector due to conduction in the r-direction, and RL is the radiation loss.

For a nozzle-type MPD arc thruster, the chamber and throat pressure is almost an order below one bar, so that the radiation losses are negligible.

The energy balance (II.5) reduces therefore to

$$- \frac{1}{r} \frac{d}{dr} (r \lambda \frac{d}{dr} T) = \frac{j^2}{\sigma} \qquad (II.6)$$

or after integration from 0 to r

$$2\pi r \lambda \frac{d}{dr} T = - 2\pi \int_0^r \frac{j^2}{\sigma} r \, dr \qquad (II.7)$$

One now takes the current density as a paraboloid of the n'th degree

$$j = \hat{j} \left[1 - (\frac{r}{r_0})^n\right] \qquad (II.8)$$

with $$\hat{j} = \frac{n+2}{n} \frac{I}{\pi r_0^2} \qquad (II.9)$$

where $I = 2\pi \int_0^{r_0} jrdr$ is the total current,

and the radii r_0 of the conducting channel can be replaced by the throat radii r_t.

With this modeling of the current density distribution one also obtains the electric conductivity. Since within the throat

$\vec{j} = \sigma \vec{E}$, where the electric field $\vec{E}$

is constant over the cross sectional area, one obtains

$$j(r) \sim \sigma(r) = \hat{\sigma} \left[1 - \left(\frac{r}{r_0}\right)^n\right] \qquad \text{(II.10)}$$

and introduced into eq. (II.7) yields

$$2\pi r \lambda \frac{d}{dr} T = - 2\pi \frac{\hat{j}^2}{\hat{\sigma}} \int_0^r \left[1 - \left(\frac{r}{r_0}\right)^n\right] r \, dr$$

$$= - \pi r^2 \frac{\hat{j}^2}{\hat{\sigma}} \left\{1 - \frac{2}{n+2} \left(\frac{r}{r_0}\right)^n\right\} \qquad \text{(II.11)}$$

Since now within the throat the electron and heavy particle temperatures are assumed identical, and since the conduction losses of the electrons are by far dominant, one may replace the conduction coefficient λ by that of the electron gas[25]

$$\lambda_e = 2.08 \frac{k^{3/2}\sqrt{T_e}}{\sqrt{m_e}\, Q_{ee}} \frac{1}{1 + \sum_{v \neq e} \frac{n_v}{v_e} \frac{Q_{ev}}{Q_{ee}} \sqrt{2 \frac{m_e}{m_v} \frac{T_v}{T_e}}} \qquad \text{(II.12)}$$

which for a singly full-ionized plasma (also valid for not fully ionized plasmas if the degree of ionization is larger than ~ 30%) reduces to

$$\lambda_e = 2.08 \frac{k^{3/2}\sqrt{T_e}}{\sqrt{m_e}\, Q_{ee}} \qquad \text{(II.13)}$$

Herein, Q_{ee} is the collision cross section between two electrons and follows by

$$Q_{ee} = \frac{\pi}{4} \left(\frac{e^2}{4\pi\varepsilon_0 k T_e}\right)^2 \ln\left\{1 + 72 \cdot \pi^2 \varepsilon_0{}^3 \frac{k^3 T_e{}^3}{n_e e^6}\right\}$$

$$= 8.77 \cdot 10^{-10} \frac{1}{T_e{}^2} \ln\left\{5.7 \cdot 10^{-3} \frac{T_e}{p_e{}^{1/4}}\right\} \quad [m^2]$$

if T_e is in Kelvin and p_e in Pascal. Hence it is

---

[25] M. Schindler, "The Transportcoefficients of Plasmas in a Multicomponent Approach," Diplom Thesis, Institute for Plasma Physics, University of Stuttgart, 1964.

$$\lambda_e = 1.27 \cdot 10^{-10} \frac{T_e^{5/2}}{\ln\{5.7 \cdot 10^{-3} \frac{T_e}{p_e^{1/4}}\}} \quad [\frac{\text{Watt}}{\text{m}^\circ\text{K}}] \qquad \text{(II.14)}$$

Since the ln term in the denominator is only a slowly varying function and for the throat conditions is about 3, the coefficient of the electron heat flux is about proportional to the electron temperature $T_e^{5/2}$ and can be set for this problem to

$$\lambda_e = \alpha\, T_e^{5/2} = 4.23 \cdot 10^{-11}\, T_e^{5/2} \quad [\frac{\text{Watt}}{\text{m K}}] \qquad \text{(II.15)}$$

Introducing this into eq. (II.11) yields

$$2\pi r\, \alpha\, T_e^{5/2} \frac{d}{dr} T_e = -\pi r^2 \frac{\hat{j}^2}{\hat{\sigma}} \{1 - \frac{2}{n+2} (\frac{r}{r_0})^n\}$$

or

$$\int_{\hat{T}_e}^{T_e(r)} T_e^{5/2}\, d\, T_e = -\frac{1}{2} \frac{\hat{j}^2}{\alpha\hat{\sigma}} \int_{r=0}^{r} \{1 - \frac{2}{n+2} (\frac{r}{r_0})^n\}\, r\, dr$$

and after integration, one obtains

$$T_e^{7/2}(r) = \hat{T}_e^{7/2} - \frac{7}{8} \frac{\hat{j}^2}{\alpha\hat{\sigma}} r^2 [1 - (\frac{2}{n+2})^2 (\frac{r}{r_0})^n] \qquad \text{(II.16)}$$

The maximum value of the electric conductivity $\hat{\sigma}$ follows according to kinetic theory by

$$\hat{\sigma} = \frac{e^2\, n_e}{\sum_v n_v \frac{8}{3} \sqrt{\frac{2}{\pi}} \sqrt{m_e k \hat{T}_e}\, Q_{ev}} \qquad \text{(II.17)}$$

and for a singly (more than 30%) ionized plasma, one obtains

$$\hat{\sigma} = \frac{3.88 \cdot 10^{-5}}{\ln\{5.7 \cdot 10^{-3} \frac{\hat{T}_e}{p_e^{1/4}}\}} \hat{T}_e^{3/2} \equiv \gamma \hat{T}_e^{3/2} \quad [\frac{\text{A}}{\text{Vm}}] \qquad \text{(II.18)}$$

where γ is only a slowly varying function of $\hat{T}_e$ and p_e and can be set to

$$\gamma = 1.30 \cdot 10^{-5} \quad [\frac{A}{Vmk^{3/2}}] \tag{II.10}$$

Replacing in eq. (II.16) σ by eq. (II.18) and j by eq. (II.10), one obtains for $r = r_0$

$$T_e^{7/2}(r_0) = \hat{T}_e^{7/2} - \frac{7}{8\pi^2} \frac{I^2}{r_0^2} \frac{1}{\alpha\gamma\hat{T}_e^{3/2}} \{1 + \frac{4}{n}\}$$

or

$$\hat{T}_e^5 \{1 - [\frac{T_e(r_0)}{\hat{T}_e}]^{7/2}\} = \frac{7}{8\pi^2} \frac{I^2}{r_0^2} \frac{1 - \frac{4}{n}}{\alpha\gamma} \tag{II.20}$$

Since the temperature at the edge $T_e(r_0)$ can be assumed small compared to the centerline temperature T_e, it follows in good approximation

$$\hat{T}_e = [\frac{7}{8\pi^2} \frac{1 - \frac{4}{n}}{\alpha\gamma}]^{1/5} (\frac{I}{r_0})^{2/5} \tag{II.21}$$

According to eqs. (II.10) and (II.18), it is

$$T_e(r) = \hat{T}_e [1 - (\frac{r}{r_0})^n]^{2/3} \tag{II.22}$$

and therefore the average temperature $\bar{T}_e$ across the nozzle throat can be related to the maximum temperature $\hat{T}_e$ by

$$\bar{T}_e = \frac{2\pi}{\pi r_0^2} \int_0^{r_0} T_e \, r \, dr = \hat{T}_e \int_0^1 [1 - z^{n/2}]^{2/3} \, dz \tag{II.23}$$

Hence, it follows according to eq. (II.21)

$$\bar{T}_e = \bar{T}_t = [\frac{7}{8\pi} \frac{1}{\alpha\gamma}]^{1/5} \cdot \Psi(n) (\frac{I}{r_0})^{2/5} \tag{II.24}$$

with $$\Psi(n) = (1 + \frac{4}{n})^{1/5} \cdot \int_0^1 [1 - z^{n/2}]^{2/3} \, dz \tag{II.25}$$

plotted in Fig. II.2.

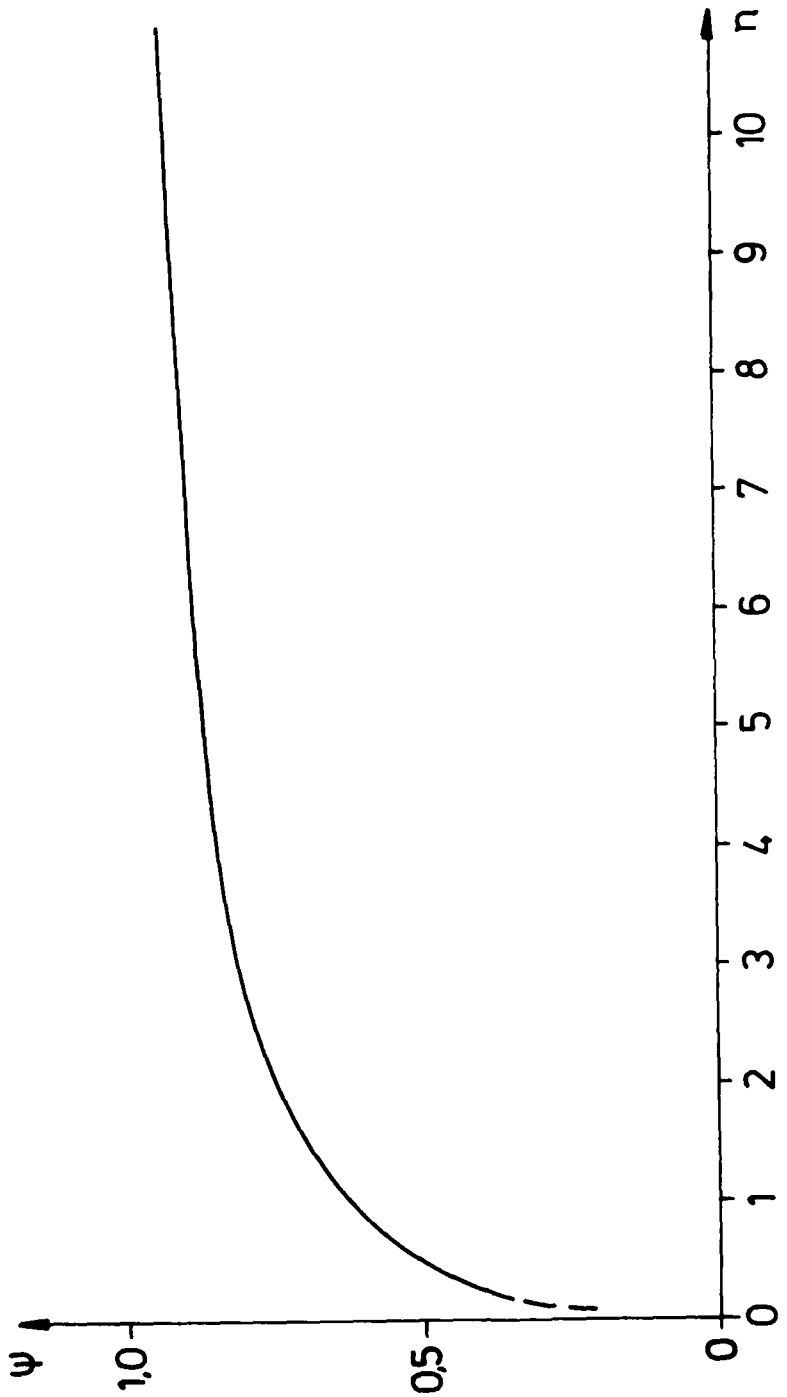

Fig. II.2 Plot of the function

$$\psi(n) = \left(1 + \frac{4}{n}\right)^{1/5} \cdot \int_0^1 \left[1 - z^{n/2}\right]^{2/3} dz$$

Appendix III

Calculation of the chamber pressure p_0 based on the nozzle throat conditions assuming an isothermal behavior for electrons and heavy particles from the cathode chamber to the nozzle throat.

Neglecting $\vec{j} \times \vec{B}$ effects, the one-dimensional equation of motion follows by

$$d\left(\frac{v^2}{2}\right) + \frac{dp}{\rho} = 0 \qquad \text{(III.1)}$$

and with

$$\begin{aligned} p &= \rho\ \alpha\ \frac{k}{m_0}\ T_e + \rho\ \frac{k}{m_0}\ T \\ &= \rho\ (1 + \alpha)\ \frac{k}{m_0}\ T_e \end{aligned} \qquad \text{(III.2)}$$

and since $T_e = T_t = \text{const}$,
one obtains

$$dp = (1 + \alpha)\ \frac{k}{m_0}\ T_t\ d\rho \qquad \text{(III.3)}$$

and the equation of motion becomes

$$\frac{v^2}{2} + (1 + \alpha)\ \frac{k}{m_0}\ T_t\ \ln\rho = \text{const} \qquad \text{(III.4)}$$

Since now the velocity $v = v_0$ in the chamber can be set equal to zero, one obtains

$$(1 + \alpha)\ \frac{k}{m_0}\ T_t\ \ln\rho_0 = (1 + \alpha)\ \frac{k}{m_0}\ T_t\ \ln\rho_t + \frac{v_t^2}{2}$$

or with $v_t^2 = (1 + \alpha) \frac{k}{m_0} T_t$ it is

$$\ln\left(\frac{\rho_0}{\rho_t}\right) = \frac{1}{2}$$

and

$$\rho_0 = \rho_t \sqrt{e}$$

or

$$\rho_0 = p_t \sqrt{e} = \rho_t (1 + \alpha) \frac{k}{m_0} T_t \sqrt{e}$$

$$= \frac{\dot{m} v_t}{A_t} \sqrt{e} = \frac{\dot{m} v_t}{A_t} \cdot 1.6487 \qquad \text{(III.5)}$$

Acknowledgements

The authors would like to thank Ms. Rhoda Stephens for typing and for her great help in interpreting and correcting the manuscript.

For the support of the Air Force Office of Scientific Research through the European Office of Aerospace Research and Development, all the participants of this research work are greatly indebted.

References

[1] P. Chr. Sleziona, "Instationary Calculation of the Electric Current Contour Lines and the Flow Field within a Cylindrical MPD Propulsion Device," Diplom Thesis, Institute for Space Systems, University of Stuttgart, April 1986.

[2] H. O. Schrade, "Magnetoplasmadynamic Effects in Electric Arcs," Interim Scientific Report, AFOSR 82-0298, Aug. 1983.

[3] J. W. Barnett and R. G. Jahn, "Operation of the MPD Thruster with Stepped Current Input," Ph.D. Dissertation, Department of Mechanical and Aerospace Engineering Faculty of Princeton University, April 1985.

[4] H. O. Schrade, M. Auweter-Kurtz, and H. L. Kurtz, "Stability Problems in Magneto Plasmadynamic Arc Thrusters," AIAA-85-1633, 18th Fluid Dynamics and Plasmadynamics and Lasers Conference, July 1985.

[5] T. Yoshikawa, Y. Kagaya, K. Kuriki, "Thrust and Efficiency of New K-III MPD Thruster," AIAA 82-1887, 16th IEPC, New Orleans, 1982.

[6] K. E. Clark and R. G. Jahn, "Magnetoplasmadynamic Thruster Erosion Studies, Phase I," Interim Report, AF Contract R 04611-79-C-0039, April 1983.

[7] K. Kuriki et al., "MPD Arc Jet System Performance Test," IAF 83-392, 34th IAF Congress, Budapest, Hungary, 1983.

[8] H. Hügel and G. Krülle, "Phänomenologie und Energiebilanz von Lichtbogenkathoden bei niedrigen Drücken und hohen Stromstärken," Beiträge Plasmaphysik, Vol. 9, p. 87, 1969.

[9] H. O. Schrade, M. Auweter-Kurtz, and H. L. Kurtz, "Plasma Thruster Development," IRA Report 85 P3, Institut für Raumfahrtantriebe, Universität Stuttgart, April 1985.

[10] A. E. Guile and B. Jüttner, "Basic Erosion Processes of Oxided and Clean Metal Cathodes of Electric Arcs," IEEE Transactions on Plasma Science, Vol. P.S.8, p. 259, 1980.

[11] L. P. Harris, "Arc Cathode Phenomena," Contr. in "Vacuum Arcs, Theory and Applications," J.M. Lafferty, ed., John Wiley & Sons, New York, 1980.

[12] A. E. Robson, "The Motion of a Low Pressure Arc in a Strong Magnetic Field," J. Physics D. Applied Physics, Vol. II, p. 1917, 1978.

[13] H. O. Schrade, M. Auweter-Kurtz, and H. L. Kurtz, "Analysis of the Cathode Spot of Metal Vapor Arcs," IEEE Transactions on Plasma Science, Vol. PS-11, No. 3, p. 103, 1983.

[14] J. P. Datlov, A. E. Guile, and B. Jüttner, "Unipolar Arc Tracks on Stainless Steel," Beiträge aus Plasmaphysik, Vol. 21, p. 135, 1980.

[15] A. E. Robson, "The Motion of an Arc in a Magnetic Field," Procedures, 4th International Conference on Phenomena in Ionized Gases IIB, 346, Aug. 1959.

[16] W. Hintze and M. Laux, "On the Motion of Unipolar Arcs in a Tokamak," Beiträge Plamaphysik, Vol. 21, p. 247, 1981.

[17] G. Ecker, "Electrode Components of the Arc Discharge," in Erg. exakt. Naturwiss., Vol. 33, p.1, 1961.

[18] G. Ecker, "Theoretical Aspects of the Vacuum Arc," in "Vacuum Arcs, Theory and Application," ed. by J.M. Lafferty, John Wiley & Sons, New York, 1980.

[19] H. O. Schrade, M. Auweter-Kurtz, and H. L. Kurtz, "Cathode Erosion Studies on MPD Thrusters," 18th International Electric Propulsion Conference, AIAA 85-2019, Alexandria, VA, 1985.

[20] H. O. Schrade, "Basic Processes of Plasma Propulsion," Interim Scientific Progress Report, Grant AFOSR 82-0298, Sept. 1985.

[21] G. N. Fursey, "Local Elementary Processes at the Formation and Operation of Vacuum Discharges," presented at the 5th Workshop on Electrode Phenomena (Berlin), May 1982.

[22] R. H. Good Jr. and E. W. Müller, "Field Emission," in Encyclopedia of Physics, "Electron Emission and Gas Discharges I," ed. by S. Flügge, Vol. XXI, Springer Verlag, Berlin, 1956.

[23] S. Anders, B. Jüttner, H. Pursch, P. Siemroth, "Investigations of the Current Density in the Cathode Spot of a Vacuum Arc," Contributed in Plasma Physics, Vol. 25, p. 467, 1985.

[24] P. Lehniger, "Designing and Building of a Test Rig in Order to Measure Cathode Erosion Caused by a Pulsed Arc," Senior Thesis, IRS, University of Stuttgart, Sept. 1986.

[25] M. Schindler, "The Transportcoefficients of Plasmas in a Multicomponent Approach," Diplom Thesis, Institute for Plasma Physics, University of Stuttgart, 1964.

END

6-87

DTIC